Measurement of the Current Profile in Fusion Tokamaks using the Motional Stark Effect Diagnostic

Sam Gibson

A thesis submitted in partial fulfilment
of the requirements for the degree of
Doctor of Philosophy

Department of Physics
Durham University

August 2021

Measurement of the Current Profile in Fusion Tokamaks using the Motional Stark Effect Diagnostic

Sam Gibson

Determining the current distribution in fusion plasmas is of paramount importance for avoiding performance limiting instabilities, and for developing plasma scenarios for future fusion power plants. Measurements of the current profile in the core plasma are obtained using the motional Stark effect (MSE) diagnostic. This diagnostic measures polarised light emission from injected fast neutrals, to obtain the pitch angle of the magnetic field. These measurements are used as a constraint in plasma equilibrium solvers, from which the toroidal current density distribution is inferred. This thesis looks to assess the capabilities of two MSE diagnostic techniques to recover the current profile of tokamak plasmas.

We first evaluate the performance of the conventional MSE diagnostic on MAST at measuring the edge current density evolution during edge localised mode cycles. Using the plasma equilibrium reconstruction code EFIT++, we infer the toroidal current density. We find that this current density depends strongly on the equilibrium settings and on the quality of the data in the pedestal region.

We describe a forward model, which considers spectral line broadening effects, to produce synthetic measurements from an imaging MSE (IMSE) diagnostic. We present in detail the design of an IMSE system for MAST Upgrade, as informed by this model. The predicted performance of the modelled diagnostic is assessed for a variety of MAST-U plasma scenarios.

We benchmark an IMSE diagnostic against a conventional MSE diagnostic on the high field side of the DIII-D tokamak. Observations in various plasma scenarios are presented, where IMSE measurements in forward field plasmas were consistent with the conventional MSE system. In reverse field plasmas, inconsistencies between the measured and EFIT predicted polarisation angles arise. This is attributed to a source of partially polarised emission at the plasma edge. We conclude by presenting potential developments of the calibration and design of future IMSE diagnostics.

Contents

List of Figures

List of Tables

Declaration

I confirm that no part of the material offered has previously been submitted by myself for a degree in this or any other University. Where material has been generated through joint work, the work of others has been indicated.

Durham, August 2021

Acknowledgements

I certainly didn't anticipate completing my PhD during a pandemic. I also didn't anticipate that during my PhD I would travel across the world to work with fusion experts, crawl inside a fusion reactor, or meet so many fascinating people along the way.

Firstly I would like to thank my supervisor Prof. Ray Sharples, for giving me this opportunity and always giving good feedback on my work (even when detective work was needed to figure out what the comments said!) A wholehearted thanks to my supervisors at CCFE: Dr Nick Hawkes for his unending patience and giving me hands on experience climbing up the side of JET for MSE calibrations just a few months into my PhD, and Dr Matt Carr, for always having an open door, sound advice and for teaching me how to code properly. A huge thanks to many others at CCFE, in particular Dr Lucy Kogan and Dr Gabor Szepesi for helping me get to grips with EFIT++, and the JET spectroscopy group for taking me in as one of their own and many interesting coffee discussions.

A huge thank you to Prof. John Howard for financial assistance which allowed me to undertake my collaboratory project at Australian National University. I will always think fondly of Canberra after being a part of such a welcoming group at PRL. I would also like to deeply thank Dr Alex Thorman, who inadvertently acquired a PhD student. It has been a pleasure to work with and learn from you. Also to Dr Clive Michael, for always having time to chat and provide useful insights, and your passion for MSE when mine had almost run out. Thanks also to Dr Joe Allcock, a true aficionado of coherence imaging, for being the only other person excited to chat about second order effects in waveplates.

I am immensely grateful to Dr Steve Allen and Dr Brian Victor for hosting me at DIII-D, and providing me with hands on IMSE experimental experience. Thank you to the wider Lawrence Livermore National Laboratory and General Atomics teams for their assistance. This work on DIII-D was performed under the auspices of the U.S. Department of Energy by Lawrence Livermore National Laboratory under Contract DE-AC52-07NA27344. This material is based upon work supported by the U.S. Department of Energy, Office of Science, Office of Fusion Energy Sciences, using the DIII-D National Fusion Facility, a DOE Office of Science user facility, under Award DE-FC02-04ER54698.

None of these opportunities would have been available to me without the Fusion CDT. A warm thank you to our lovely admin staff Kathryn and Ruth who were always so pleased to welcome us back 'home' to the YPI for fusion frontiers. My fusion family I gained along the way contains some of the most incredible people I have ever met (particular mention to the York crew, who were dearly missed when I moved to Oxford). Without you, and my wonderful housemates Charlie, Simon, and Bhavin (and Tom, Jack, Sam and Omkar since you practically lived with us anyway) this journey wouldn't have been half as fun.

To my lovely Jake; for your positivity, for always lifting me when I was struggling, for doing significantly more than your fair share housework whilst I was writing up. I don't know what I would do without you, and I'm excited to see where our scientific endeavors take us together.

Thank you to my family for always being supportive, to granddad for letting me destroy your camcorder wires as a baby, which must have lead me on the path to becoming a scientist, and my wonderful mam for always telling me 'you can only do your best'.

Chapter 1

Introduction to Fusion Energy

Demand for energy is increasing globally and is predicted to grow further this century, driven by economic growth. Energy consumption is the largest contributor to global greenhouse gas emissions[2] and so a rapid shift to low carbon energy sources is required. It is desirable for electricity to be supplied from a mixture of intermittent variable sources (such as wind, solar, hydro, biomass) as well as firm sources (nuclear fission, natural gas with carbon capture and storage (CCS)) to balance supply and demand of the electricity grid[3]. Nuclear fusion has the potential to provide a long-term source of energy, which produces low associated carbon emissions. Fusion power plants have some attractive advantages over current generation nuclear fission power plants[4], including: Nuclear proliferation risks are minimal as no fissile materials are produced in the fuel cycle[5], no long-lived high level and reduced levels of intermediate level nuclear waste[6], and no risk of a plant meltdown. With increased financing, research and development both through the public sector and private fusion companies, fusion power plants could provide electricity to the grid in the latter half of this century.

Still there remains a number of difficult engineering and plasma physics challenges to overcome to realise a fusion power plant. From a plasma physics perspective, we must fully understand what factors improve plasma confinement, how to completely mitigate plasma disruptions in tokamaks to avoid damage to the reactor and find appropriate solutions to manage the plasma

exhaust. Current experimental fusion devices are fitted with an extensive suite of plasma diagnostics to make measurements of the currents, electromagnetic fields and emission from the plasma.

1.1 Principles of Fusion Energy

Isotopes of hydrogen fuse together under high temperature and pressure conditions, forming heavier elements and in the process releases energy. Fusion is the dominant source of energy in the Sun, via proton-proton fusion. This fusion pathway has a particularly low cross section and is only achieveable due to the immense pressures and temperatures inside the Sun, long confinement times on the order of several millions of years. At more attainable pressures ($\approx$3x10^{5}N/m^2) and temperatures (<1MeV) on Earth, the largest fusion reaction cross section is between deuterium (D) and tritium (T), as shown in Fig. 1.1,

$$ {}^{2}_{1}\mathrm{D} + {}^{3}_{1}\mathrm{T} \rightarrow {}^{4}_{2}\mathrm{He} + \mathrm{n} + 17.6\mathrm{MeV} \tag{1.1} $$

For this reaction to take place, the Coulomb barrier must be overcome. There is a small but finite probability for nuclei with energies lower than the Coulomb barrier to fuse due to quantum tunneling. The reactants must be sufficiently close, with high enough temperatures, such that the short range nuclear strong force binds the nuclei together. Through this reaction process, kinetic energy is released and carried predominantly by the fast neutron, which must be captured. In fusion power plants, it is envisaged that the neutrons are trapped within breeding blankets to produce additional tritium [9] and heat a coolant to extract energy from the reactor.

For a viable fusion reactor, power losses must be smaller than the externally supplied power and the α particle power. The 'ignition' condition is met when α particle heating is significant enough to sustain the plasma temperature without the need for external heating mechanisms. This leads to the Lawson criteria, or triple product, which maximizes confinement time τ_E, the temperature of the distribution T and the particle density n,

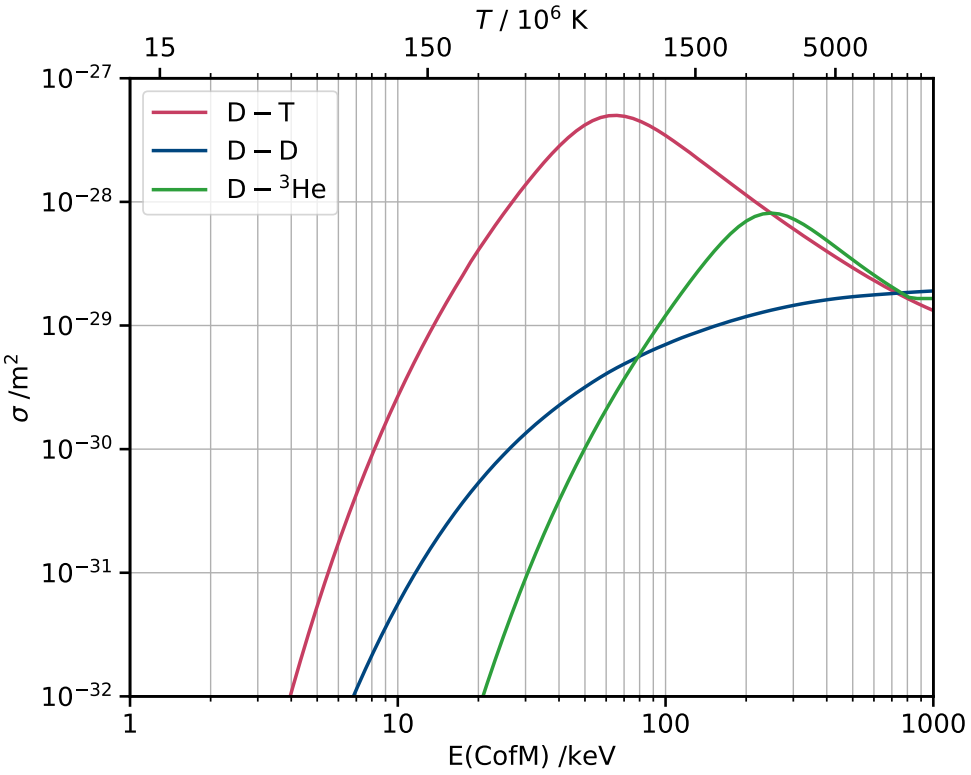

Figure 1.1: Cross sections of various fusion reactions as a function of center of mass (CoM) energy, reproduced from [7] using data from [8]. DT fusion has the highest cross section at physically feasible temperatures.

$$nT\tau_E = \frac{12}{\langle\sigma v\rangle}\frac{T^2}{E_\alpha} > 3 \times 10^{21}\mathrm{m}^{-3}\mathrm{keVs} \tag{1.2}$$

where $E_\alpha = 3.5$ MeV, $\langle\sigma v\rangle$ the reaction rate, n is the plasma density, T the plasma temperature and τ_E the confinement time.

There are two main strands of fusion research which lead to different fusion reactor designs to achieve the Lawson criteria: Inertial Confinement Fusion (ICF) where high powered lasers are fired at a frozen fuel pellet, causing ablation of the outer shell and rapid expansion of plasma which compresses inner fuel material to densities and temperatures such that fusion occurs. The alternative, and the focus of the diagnostic research in this thesis, is on Magnetic Confinement Fusion (MCF) which employs electromagnetic fields to confine the plasma. From Fig. 1.2 it is clear to see operating parameter spaces

for a tokamak reactor; temperatures of 10-20keV, densities of $\approx 10^{20}\mathrm{m}^{-3}$, and confinement times on the order of several seconds.

To be cost effective, a fusion reactor must produce more energy than is consumed to heat the plasma. We can define the efficiency of a fusion reactor, given by the ratio of fusion power produced to the externally supplied heating,

$$Q = \frac{P_{out}}{P_{ext}} \tag{1.3}$$

For a reactor to 'break even', achieving Q = 1 is required. In the case where the triple product requirement is met and fusion is sustained predominantly through the fusion reaction (ie. via alpha particle heating) then Q $\rightarrow \infty$. Currently the greatest efficiency record is held by the JET tokamak, set in 1997 [10] for Q = 0.65. The next generation of tokamaks, are aiming for Q $\geq$ 10 [11] resulting in 500MW of fusion power for 50MW injected power, and the recently designed SPARC tokamak with aims for Q > 2 with 50-100MW fusion power output [12].

1.2 Magnetic Confinement Fusion

1.2.1 Plasma Confinement

MCF uses magnetic fields to confine charged particles in the plasma. Movement of charged particles is restricted perpendicular to the magnetic field lines via the Lorentz force,

$$F = q(\boldsymbol{E} + \boldsymbol{v} \times \boldsymbol{B}) \tag{1.4}$$

where $\boldsymbol{v}$ is the particle velocity and a charge q. Particles then gyrate around magnetic field lines with frequency $\omega_c = qB/m$ at the Larmor radius $\mathrm{r}_l = \mathrm{v}_\perp/\omega_c$. In this configuration, particles are free to move parallel to field lines. To avoid particle losses, the field lines are wrapped into a toroidal geometry to form the familiar doughnut or 'torus' shape of the tokamak.

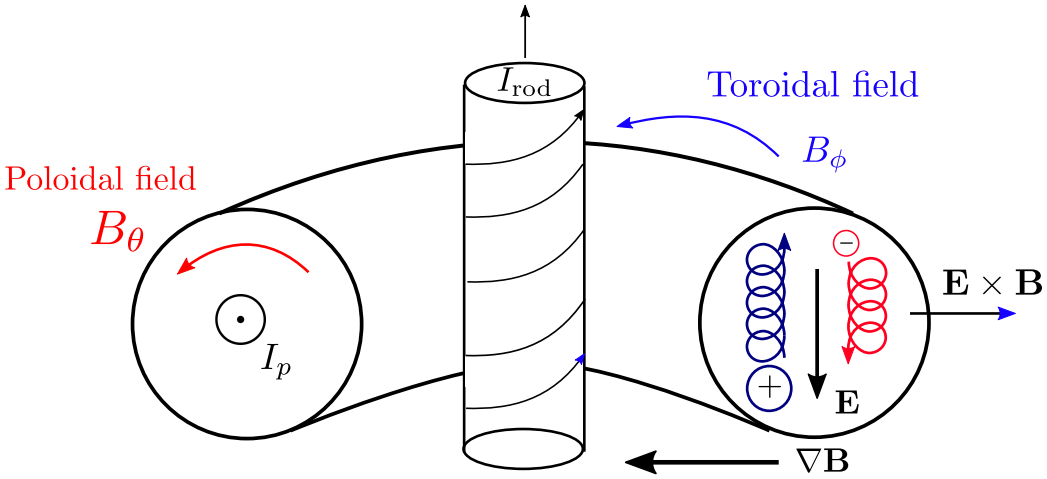

Figure 1.2: Tokamak geometry showing the poloidal and toroidal components of the magnetic field. Ramping the solenoid current generates a time varying magnetic flux, which generates a loop voltage and drives a toroidal plasma current I_p (out of the page). The motion of electrons and ions is shown, and the resulting $\mathbf{E} \times \mathbf{B}$ drift radially outwards.

A magnetic field must be generated to confine the plasma. The primary toroidal magnetic field is generated by surrounding external magnetic field coils. With only a toroidal field present, field line curvature and field gradients lead to vertical particle drifts. Naturally via the Lorentz force ions and electrons drift in opposing directions, and this charge separation generates an electric field, resulting in an E×B radial drift of particles and poor confinement. To short out this electric field, a poloidal magnetic field B_θ is required. To create the poloidal field, current is ramped through the central solenoid and, via transformer action, a current is subsequently induced in the plasma acting as the secondary circuit resulting in the poloidal magnetic field. Additional poloidal field coils contribute to B_θ and are used for plasma shaping. These two field components combined lead to helical magnetic field line structure.

To describe these helical magnetic field lines, if a single field line was traced around a number of toroidal turns n, then the field line would traverse m poloidal revolutions. This ratio of toroidal to poloidal turns is known as the safety factor q profile, a measure of how 'twisted' the magnetic field is,

$$q = \frac{1}{2\pi} \oint \frac{B_\phi}{R B_\theta} ds = \frac{m}{n}, \tag{1.5}$$

and is defined as the closed loop integral around a path length ds around

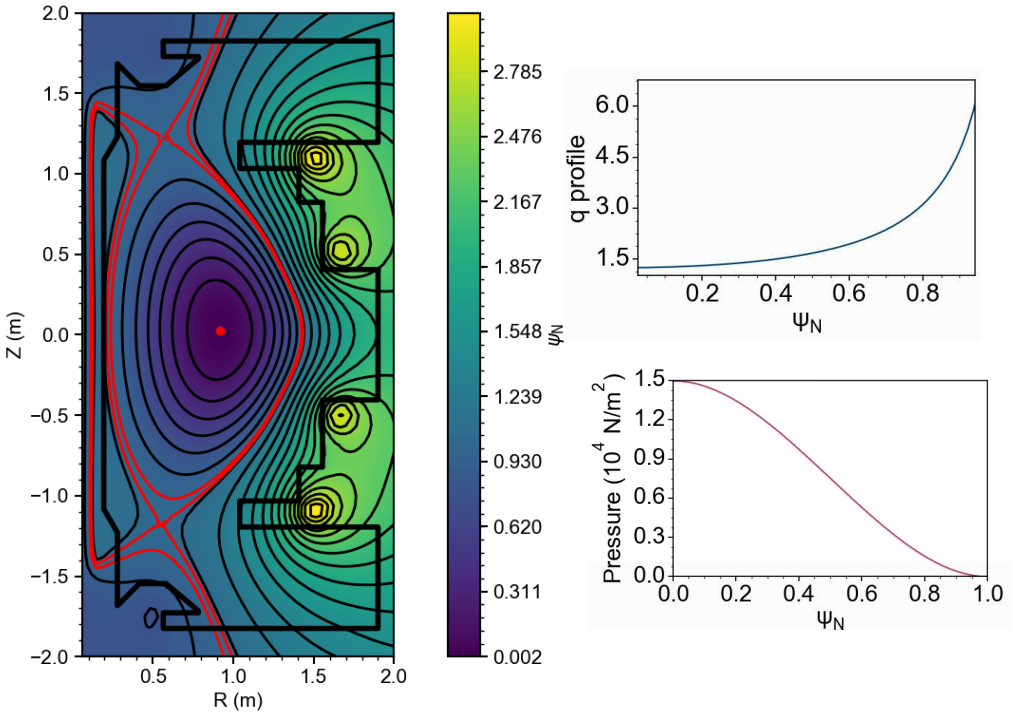

Figure 1.3: Example of a poloidal cross section of a MAST plasma. The normalised poloidal flux $\psi_N = 1$ at the plasma boundary (red outline) and $\psi_N = 0$ at the magnetic axis (red circle). The MAST vessel wall is shown in black. The q profile shown (blue) is 'monotonic' ie. the current profile peaks on axis and varies smoothly, decreasing towards the plasma edge. Data retrieved from the MAST database.

a magnetic flux surface. The 'pitch' of the helical field lines is then defined as $\tan(\alpha_{\text{pitch}}) = B_\theta/B_\phi$. The ratio of q is of critical importance for plasma stability. At all points in the plasma q > 1 must be satisfied to avoid particle losses and the sawtooth instability[13]. Upon rational q surfaces, for example at q = 3/2 or q = 1/2, MHD instabilities such as the neoclassical tearing mode (NTM) can occur [14], which are detrimental to plasma performance. Knowledge of the location of these surfaces, and the overall shape of the q profile can help to mitigate these performance limiting instabilities. Typical poloidal plasma cross section, pressure and q profiles for a MAST are shown in Fig. 1.3.

1.2.2 Plasma Heating

Additional external current drive is required to heat the plasma to fusion relevant temperatures. The plasma toroidal current provides a source of plasma heating known as ohmic heating, due to the plasma resistance η generated by collisions between ions and electrons. As the resistance of the plasma is strongly linked to the plasma temperature, $\eta \propto T^{-\frac{3}{2}}$, at very high plasma temperatures ohmic heating is not particularly effective [15]. There are a plethora of additional methods to inject heat and current into plasmas, such as: propagating radio frequency (RF) waves via Ion Cyclotron Resonance Heating (ICRH), heating electrons via ECRH, and neutral beam injection (NBI). Neutral beam injection systems fire neutral deuterium (or hydrogen or tritium) into the plasma. NBIs can inject several megawatts of power per source into the plasma, and on the MAST tokamak the two available NBIs contribute up to 3.8MW of power[16]. Ideally in a fusion reactor, external heating is applied until the plasma reaches fusion relevant conditions where α particle heating dominates and ignition is achieved.

1.2.3 Plasma Equilibrium

To produce a stable plasma, the magnetic forces and pressure gradient forces must be balanced,

$$\nabla P = \boldsymbol{J} \times \boldsymbol{B} \tag{1.6}$$

where P is the plasma pressure, $\boldsymbol{J}$ is the current density and $\boldsymbol{B}$ is the magnetic field, and the assumption is made that the plasma is stationary. Force balance in steady state implies $\boldsymbol{B} \cdot \nabla P = 0$ and $\mathbf{J} \cdot \nabla P = 0$, that the magnetic field and current density are perpendicular to the pressure gradient, and that pressure is constant along magnetic field lines. This results in a set of concentric surfaces of constant pressure with high pressure in the center of the plasma and lower pressure at the edge. It is useful to name these as flux surfaces ψ. Current flows along these flux surfaces, and using Ampere's law, $\nabla \times \boldsymbol{B} = \mu_0 \boldsymbol{J}$, where μ_0 is the vacuum permittivity. By introducing the current flux function $f(\psi)$, the toroidal component of the current density

from equation 1.6 can be described in terms of the functions $p(\psi)$ and $f(\psi)$,

$$f(\psi) = \frac{RB_\phi}{\mu_0}, \tag{1.7}$$

where μ_0 is the vacuum permeability. The toroidal current density is then,

$$j_\phi = R\frac{dp}{d\psi} + \frac{\mu_0 f}{R}\frac{df}{d\psi}. \tag{1.8}$$

Finally, by defining the magnetic field components in terms of the flux function ψ and f[17] and writing the toroidal current density in terms of the poloidal flux,

$$\Delta^*\psi = -\mu_0 R^2 p'(\psi) - \mu_0^2 f(\psi) f'(\psi) \tag{1.9}$$

where $\Delta^* = R\frac{\partial}{\partial R}\frac{1}{R}\frac{\partial}{\partial R} + \frac{\partial^2}{\partial z^2}$. This equation is known as the *Grad-Shafranov* (GS) equation and forms the basis of plasma equilibrium. The GS equation then has only three unknowns to solve for in order to determine the magnetic field components everywhere in the plasma; The poloidal flux function ψ, the plasma pressure $p(\psi)$ and the current flux function $f(\psi)$. However, the GS equation is a non-linear, second order partial differential equation, and only has analytic solutions for circular flux surface shapes. Tokamak plasmas are now highly shaped, meaning this equation must be solved numerically. Measurements from within the plasma can be used to constrain the position of the magnetic flux surfaces, for example measurements of the magnetic coil currents to estimate the plasma boundary location. These measurements are fed into equilibrium solvers which parametrize the pressure and current profiles and aim to provide a best fit to diagnostic measurements. Plasma equilibrium reconstruction forms the basis of almost all tokamak physics research, and obtaining an equilibrium representative of the plasma flux surface shapes is non-trivial. The distribution of current and magnetic field topology are crucial to the performance of the plasma, and so accurate knowledge of the internal plasma profiles is vital. To obtain accurate plasma equilibrium and to study these performance limiting instabilities, diagnostics with the ability to measure the internal current and pressure profiles are therefore essential.

1.3 Fusion Tokamak Reactors

The aspect ratio $A = R/a$, where R is the plasma major radius and a the plasma minor radius, is significantly smaller in spherical tokamaks ($A < 1$ than in conventional tokamaks. Scaling laws[1] derived from conventional tokamaks show that the global confinement time scales strongly with the plasma major radius. This then leads to the argument for 'bigger is better" when it comes to future fusion devices, reflected in the size of ITER plasmas (twice the major radius of JET and a plasma volume 8 times larger!)

Plasmas in spherical tokamaks have shown that the energy confinement dependence on the toroidal magnetic field could be higher [18]. Fusion power scales with the magnetic field strength and the plasma parameter β, which is defined as the ratio of the plasma pressure p to magnetic pressure,

$$\beta = \frac{p}{B_0^2/2\mu_0}. \tag{1.10}$$

Fusion power scaling is then $P \propto B^4\beta^2$[19]. As spherical tokamaks have a higher plasma β, we could envisage smaller spherical tokamaks as a candidate for future fusion reactor designs. Some other advantages of the spherical tokamak include the fact that ST plasmas are naturally highly elongated due to the low aspect ratio, which leads to improved vertical stability with increasing edge safety factor [20]. Additionally this means the plasma normalised β is greatly increased, meaning ST plasmas make more efficient use of the toroidal magnetic field. High β_N and strong elongation then allows for a significant contribution to the total current from the self generated plasma 'bootstrap' current arising due to the strong pressure gradients. This means less external current drive is required in order to sustain the plasma leading to increased fusion efficiency [21].

In this thesis, measurements are presented from both a conventional aspect ratio device, DIII-D, and a tight aspect ratio device, MAST.

[1]Scaling laws apply a multi-parameter fit of various engineering parameters to a measurement of the confinement time from different conventional aspect ratio tokamaks and plasma pulses to understand which parameters have the most influence on confinement time. They are favoured as an initial calculation to scope out a new tokamak's parameter space as they are computationally cheap in comparison to 2D/3D transport modelling.

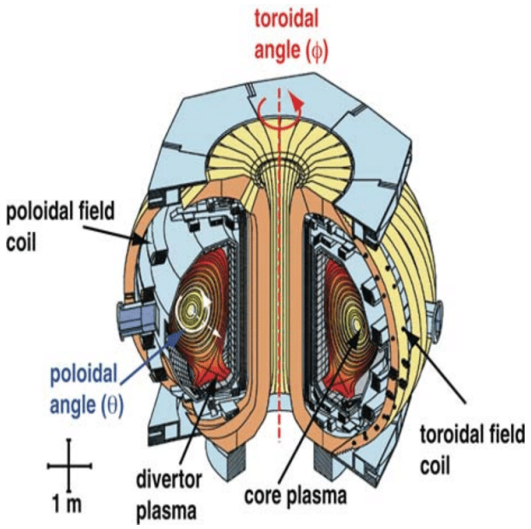

Figure 1.4: Diagram of the DIII-D tokamak[24].

1.3.1 DIII-D

The DIII-D tokamak located in San Diego, USA, is a conventional aspect ratio tokamak which has been operational since 1986. The main aims of DIII-D is to develop solutions to physics challenges necessary for the success of ITER, development towards a steady state fusion reactor through efficient external current drive methods, and to provide solutions for divertor challenges in the next generation of fusion reactors [22]. Notably DIII-D is well equipped with external heating and current drive systems, including eight neutral beam injector systems and 6 gyrotrons. Additional shaping coils allow DIII-D to explore new plasma shapes, such as negative triangularity plasmas which have high confinement characteristics without a significant pedestal structure [23]. A diagram of the DIII-D tokamak is shown in Fig. 1.4. Measurements from the imaging motional stark effect diagnostic were taken on the DIII-D tokamak during an experimental campaign in 2019 in chapter 5 of this thesis.

1.3.2 MAST and MAST Upgrade

MAST, now known as the upgraded MAST Upgrade (MAST-U) tokamak following a major upgrade, is a spherical (low aspect ratio) device. MAST-U looks to explore whether the spherical tokamak can be a strong design candidate for a future fusion power plant. Subsequent upgrades through the enhancements program [25] will look to further understanding of plasma confinement, high β scenario operation and most importantly handling of plasma exhaust through the new Super-X divertor configuration. Notably in 2019 the UK government approved £220 million of funding to produce a concept design for a next generation Spherical Tokamak for Energy Production (STEP), which aims to provide net electricity to the national grid[26]. This is a first step towards a spherical tokamak fusion plant. The results from the MAST-U campaigns will feed strongly into the design and parameter space for STEP. After an upgrade period of 6 years, MAST-U entered commissioning and its first physics campaign in late 2020.

The most notable upgrade for MAST-U is the ability to produce novel divertor configurations, such as the 'Super-X' divertor[27], shown in Fig. 1.5. By increasing the connection length of the magnetic field lines within the divertor, and varying the strike point position, these advanced divertor configurations are predicted to reduce the peak heat flux to the divertor tiles[28]. Other purposes of the divertor include impurity control through transport in the scrape off layer (SOL) to be neutralised in the divertor. One of the main aims then for MAST-U is to test these advanced exhaust solutions and their suitability for future fusion devices.

Other main aims of MAST-U include an understanding of performance limiting magneto-hydrodynamic (MHD) instabilities, including developing scenarios with the Edge Localised Mode (ELM) instabilities completely suppressed using Resonant Magnetic Perturbation (RMP) coils. This is a key area of research for large fusion devices such as ITER, where energy fluence of around 20MJ could be lost per ELM. Maximum tolerable ELM energy fluxes are predicted to be 0.5MJm^{-2} at Q=10 operation without significant

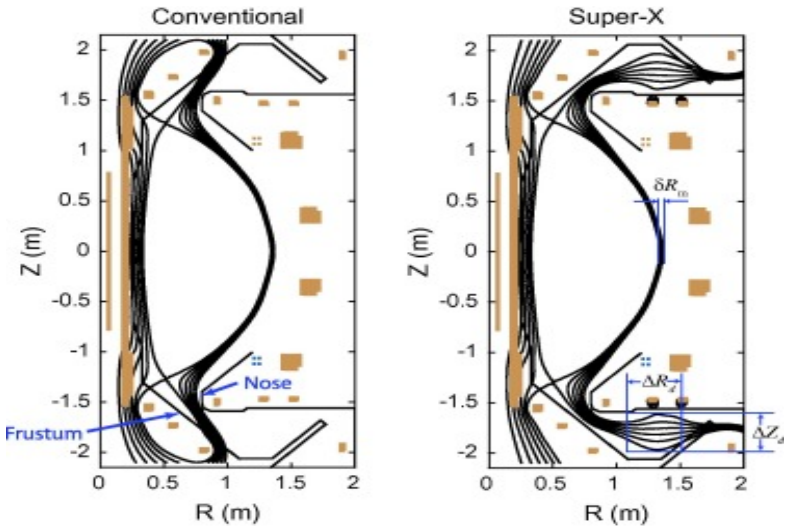

Figure 1.5: Conventional and 'Super-X' divertor configurations for MAST-U, from [29].

damage to the ITER divertor [30, 31]. [2] Therefore, ELM control via RMPs is of crucial importance to ITER.

Core plasma parameters for MAST and MAST-U are outlined in Table. 1.1. The aim is to increase the plasma pulse length from 0.5s to 6s. Further neutral beam heating systems will be installed as part of the enhancements program, including an off-axis neutral beam to study current drive efficiency. A microwave heating system known as Electron Cyclotron Resonance Heating (ECRH) is also to be included as an enhancement, allowing opportunity to investigate a predominantly electron heated parameter space for spherical tokamaks, which has not previously been explored [25].

1.4 Plasma Diagnostics

Diagnostic measurement of plasma parameters is vital for understanding the internal state of the plasma, plasma conditions, and plasma interactions with both electromagnetic fields and the tokamak vessel. The high temperatures

[2] To put this into context, the major radius of ITER is R≈6.2cm. With a predicted strike width of 1-3cm, then the energy flux in the divertor could range from 17-51MJm^{-2}, at least an order of magnitude larger than the tolerable limit.

Parameters	**MAST**	**MAST-U**
Major radius (m)	0.85	0.85
Minor radius (m)	0.65	0.65
Plasma current (MA)	1.3	2.0
Magnetic field at R=0.85m (T)	0.52	0.75
Total NBI power (MW)	3.8	5.0
On-axis NBI power (MW)	3.8	2.5
Off-axis NBI power (MW)	0.0	2.5
Pulse length (s)	0.6	5

Table 1.1: Comparison of the operational parameters for MAST and MAST-U. The MAST-U plasma parameters are given as the intended full capabilities after further enhancements. Table generated from the MAST-U research plan 2019[25].

of the core plasma region mean it is infeasible to use probes or other invasive methods frequently used in the cooler edge region to measure the current profile. Favorably, tokamak plasmas emit radiation across the whole electromagnetic spectrum. This can be exploited as a passive plasma diagnostic. Passive diagnostics use non-invasive methods of quantifying plasma quantities of interest, by measuring spectral line emission from the plasma. One of the brightest emission lines within the visible wavelength region is the Balmer-α line. This common emission line measured in fusion plasmas is due to transitions from the n=3 to n=2 states in hydrogenic atoms at λ=651nm and so can be measured easily using conventional optics and spectrometers. This is the emission line of interest for the beam spectroscopy techniques mentioned in this thesis.

1.4.1 Active Beam Spectroscopy

As mentioned previously in section 1.2.2, neutral atoms (typically Hydrogen or Deuterium) are often injected into fusion plasmas as a source of external heating. These fast neutrals interact with thermal ions or impurity ions within the plasma, become excited and emit radiation. Measuring emission from these excited states is known as *active beam spectroscopy*. "Active" spectroscopy is named from the active nature of perturbing the plasma in

order to make a measurement. For some diagnostics this could be inserting probes into the plasma to measure current, lasers, microwaves, or in the case of active beam spectroscopy the neutral beam injection (NBI) system.

Beam spectroscopy diagnostic techniques are well established and provide key information on the plasma profiles. Beam spectroscopy diagnostics examples include: Charge eXchange Recombination Spectroscopy (CXRS), measuring emission from impurity ions exchanging electrons with fast neutrals. The measured impurity line width provides information on the ion temperature, and can be used to derive the plasma toroidal rotation [32]. The Fast Ion D-Alpha (FIDA) diagnostic[33] measures emission through charge exchange between fast plasma ions and the neutral beam atoms, and can be used to derive the fast ion distribution function. Finally, we come to the Motional Stark Effect (MSE) diagnostic[34], which is the technique focussed on in this thesis.

1.4.2 The Motional Stark Effect Diagnostic

The MSE diagnostic measures polarised line emission from neutral beam atoms. As these fast neutrals move across the magnetic field, they experience a Lorentz electric field $\mathbf{E} = \mathbf{v} \times \mathbf{B}$ in their rest frame. The Stark effect causes wavelength splitting of the Balmer line and the emission is polarized with respect to the Lorentz electric field. Transitions where $\Delta m = 0$, also known as π emission lines, are linearly polarized parallel to the electric field. Transitions to states with Δm=$\pm$1, known as σ emission lines, produce linearly polarised emission perpendicular to the $\mathbf{E}$ field. Then, the measured polarisation angle with respect to the Lorentz $\mathbf{E}$ field can be used to infer the magnetic field line pitch angle. In Chapter 2 the physics of the Motional Stark Effect and the diagnostic technique will be expanded upon in further detail.

The MSE spectrum features were first observed on the JET tokamak[35] and by fitting to a spectral model, the Stark shift separation between the π and σ lines was used to calculate the strength of the local poloidal magnetic field at different radial locations in the plasma, as well as the safety factor on axis. This opened the avenue for local measurement of the poloidal field

since the emission was measurable at visible wavelengths within a part of the wavelength spectrum already well calibrated (using plasma emission D_α line at λ=656.1nm). Almost simultaneously the design of a polarimetry system and measurements from the PBX-M tokamak were presented[34], which we will refer to as the 'conventional' MSE system. This measurement technique uses photoelastic modulators (PEMs), large aperture crystals driven at a specific frequency to encode polarisation information as an amplitude modulation. This system used a single fiber sight line, which was moved to view different radial locations within the plasma over identical plasma pulses to build up a radial profile of the polarisation angle. This system led to measurements of the value of q at the magnetic axis and provided evidence to validate models of the sawtooth instability[36].

Almost all major tokamaks now include an MSE diagnostic, and they are an integral part of the suite of plasma diagnostics necessary for physics analysis. On low magnetic field devices, spectral discrimination of a single component within the MSE multiplet is difficult due to small Stark shifts within the MSE multiplet and significant spectral broadening, as is the case on MAST and NSTX[37, 38]. Conventional MSE systems require extremely narrow bandpass filters (FWHM = 0.12nm) to select a σ or π component for measurement of the polarisation angle. Alternatives to the conventional polarimetry method were considered at NSTX-U. The MSE Laser Induced Fluorescence (MSE-LIF) technique [39] uses a tunable laser, fired into a highly collimated dedicated neutral beam to stimulate emission from the Doppler shifted D_α line. This diagnostic measures the Stark shift to determine the magnitude of the magnetic field, with predicted resolution of down to 10^{-4}T [40].

A comprehensive overview of MSE systems on several tokamaks and notable measurements can be found in[41]. However there have been some advances since this paper, particularly in the new imaging Motional Stark Effect (IMSE) technique. The IMSE technique was developed at Australian National University (ANU) in the early 2000s, where a variety of polarisation encoding methods have been implemented[42–44]. The system is based on a 2D polarisation interferometer, using birefringent crystals to produce a phase shift between ordinary and extraordinary components of incident

polarised light, which when recombined with a polariser, encodes the polarisation information spatially within the phase of the resulting interferogram. The brightness or 'fringe contrast' then contains information on the spectral intensity, the fringe phase retrieves information on the Doppler shift of the emission and the polarisation angle. To discriminate between contributions to the fringe phase due to the Doppler shift and the polarisation angle, a switching halfwave plate is used such that the difference in the interferogram phase between two successive images retrieves only the polarisation angle. This technique, known as the Temporally Switched Single Spatial Heterodyne (TSSSH) approach was employed on the KSTAR tokamak[45], and the DIII-D tokamak[46], where the system was bench marked against other MSE diagnostics. An IMSE system was also developed for the ASDEX-U tokamak[47], using an alternative amplitude double spatial heterodyne (ADSH) encoding technique, where measurements have been used to corroborate neoclassical current diffusion models during sawtooth events [48]. The IMSE system benefits from increased number of measurements over a traditional fiber based MSE system, providing additional 2D information which cannot be recovered using the conventional MSE system. It has not yet been investigated in depth whether IMSE measurements can improve the quality of the pressure and current profiles resulting from equilibrium reconstruction codes. Additionally significant improvements in the switching waveplate uniformity is required for IMSE systems using the TSSSH technique, in order to ensure a bench calibration of the diagnostic is an accurate representation of the ray paths through the polarimeter when viewing neutral beam emission [49].

1.5 Motivation

In the previous section we have shown that there are several diagnostic techniques which have been used to measure MSE emission in tokamak plasmas. This thesis will concentrate on two techniques; The conventional MSE diagnostic and the Imaging MSE (IMSE) technique for measuring the current profile in fusion devices. These MSE diagnostics provide a local measure of

the magnetic field line pitch across the plasma, and so these measurements are critical to constrain equilibrium reconstruction codes. The resulting pressure and current profiles from these equilibrium facilitate stability analysis of the plasma, and develop our understanding of performance limiting MHD modes and ELMs, which degrade plasma confinement.

There are very few examples of local measurements of the edge current density in tokamaks, and so typically this is calculated using theoretical models of the current distribution[50, 51]. During a previous campaign on the MAST tokamak, attempts to measure the edge current density using the conventional MSE diagnostic were made and used to inform stability analysis. This analysis was achieved for a limited number of times in single plasma discharge. This thesis first looks to extend this analysis and answer two questions:

- Is it possible to resolve the edge current density directly using the conventional MSE diagnostic?
- To what extent does the diagnostic constraints and uncertainties influence the edge current density inferred using equilibrium reconstruction codes?

Due to delays in the MAST-U timeline, alternative MSE measurement techniques were explored as an additional candidate MSE diagnostic for MAST-U. Subsequent to the development of the IMSE technique outlined in section 1.4.2, this thesis then looked to develop a forward model to predict the performance of an IMSE diagnostic on MAST-U. Due to the low magnetic field on MAST-U, it was important to use a spectral model which included significant sources of spectral broadening. The MSESIM[52] modelling code was used to generate synthetic MAST Upgrade spectra, and to develop a forward model of the IMSE diagnostic. With this forward model, this thesis looks to:

- Propose a candidate IMSE system design optimised for MAST-U.
- Indicate the modelled performance of the system in MAST-U plasmas.

Finally, the IMSE modelling work led to a short secondment to the DIII-D tokamak at General Atomics (GA) with Lawrence Livermore National

Laboratory (LLNL), working under Dr Brian Victor and Dr Steve Allen. Parasitic measurements were made with the IMSE diagnostic at DIII-D with a unique view towards the high field side (inboard) of the machine, which is poorly diagnosed by plasma diagnostics. In this section of the thesis, we look to:

- Assess the IMSE diagnostic consistency with other well established conventional MSE systems.
- Understand the impact of including IMSE high field side measurements within equilibrium reconstruction codes.

1.6 Thesis Overview

This thesis is laid out as follows. Chapter 2 gives an overview of the atomic theory necessary to understand the origins of the motional Stark effect and introduces the mathematical formalisms of the Stokes vector and Mueller matrices to describe the evolution of the polarisation state of light. This mathematical formalism is then used to describe the two measurement techniques focussed on in this thesis, the conventional MSE dual photoelastic modulator polarimetry technique, and the interferometry based imaging motional Stark effect technique. Chapter 3 looks to understand the relationship between conventional MSE diagnostic measurements and their role in the constraint of equilibrium reconstruction in MAST plasmas with a focus on resolving the edge current density evolution. Chapter 4 describes the spectral modelling code MSESIM and how spectral broadening effects such as the beam divergence, collection volume and finite collection optics effect the modelled MSE spectrum. This is coupled to a forward model developed for the IMSE diagnostic, and the design of an IMSE system on MAST is outlined. The performance of the modelled diagnostic is then assessed for some predicted MAST-U scenarios. Future development work required to implement the diagnostic is suggested. Chapter 5 presents results from an experimental campaign on the DIII-D tokamak, using an IMSE diagnostic with a unique view to the high field side of the tokamak. Measurements of the system were compared to those from additional conventional MSE systems,

and the IMSE measurements integrated into the equilibrium reconstruction EFIT[53]. Finally, Chapter 6 provides a summary of the thesis work, together with developments and extensions to the work presented.

Chapter 2

Polarimetry as a Diagnostic for Fusion Devices

Polarimetry is the measurement of polarised light. Measuring the polarisation state of light gives information on the medium through which the electromagnetic radiation propagates, and also upon the electric and magnetic fields which influence the polarisation state of an atom. Polarimetry has a long history within astronomy and solar spectroscopy[54]. Analogous polarimetry diagnostics on fusion tokamaks have lead to the measurement of the line integrated electron density[55], the magnetic pitch angle[34] and even localisation of synchotron radiation due to runaway electrons[56].

The focus of this thesis is on the Motional Stark Effect (MSE) diagnostic, a polarimetry based technique which provides a measurement of the local poloidal magnetic field within a plasma. As briefly outlined in section 1.4.2, the MSE principle relies on the generation of a strong Lorentz electric field due to the movement of fast neutral deuterium (or hydrogen) across a magnetic field. This in turn gives rise to Stark split line emission which is polarised with respect to the Lorentz **E** field, and a spectrum consisting of 9 (out of 15) bright transition lines is produced. The emission from these Stark split states is polarised with respect to the E field. As such, by measuring the polarisation angle γ one can determine the orientation of the **B** field component perpendicular to **E**, and subsequently the magnetic pitch angle $\gamma_{\text{pitch}}=$

$\arctan(B_\theta/B_\phi)$. These measurements are coupled with plasma equilibrium solvers to inform upon the current distribution and q profiles in tokamaks. Accurate knowledge of these profiles is critical to avoid performance limiting instabilities.

In this chapter we will introduce the concept of energy level perturbation due to external electric and magnetic fields, building to the motional Stark effect principle. Then, we will lay the mathematical framework required to describe the different polarimetry techniques, conventional dual photo-elastic modulator (PEM) polarimetery and coherence imaging based polarimetry, used within this thesis.

2.1 The Hydrogen Atom

Before tackling atoms within external electric and magnetic fields, we first look at the unperturbed energy levels in Hydrogen and introduce some relevant quantum numbers. The total energy E_n of a bound electron in each stationary state is quantised and given by,

$$E_n = -\frac{R_y Z^2}{n^2}, \tag{2.1}$$

where R_y is the Rydberg energy (13.6 eV), Z is the proton number, and the principal quantum number n. Angular momentum is also quantised, which can be shown by solving the Schrodinger equation in spherical coordinates[57]. This leads to the angular momentum operators $\mathbf{L}$ and $\mathbf{L}_z$,

$$\begin{aligned} \boldsymbol{L}^2 \left|n, \ell, m_\ell\right\rangle &= \ell(\ell+1)\hbar^2 \left|n, \ell, m_\ell\right\rangle, \\ \boldsymbol{L}_z \left|n, \ell, m_\ell\right\rangle &= m_\ell \hbar \left|n, \ell, m_\ell\right\rangle, \end{aligned} \tag{2.2}$$

where the orbital angular momentum quantum number ℓ can take integer values from ℓ=0 to $(n-1)$, m_ℓ is the magnetic quantum number, spanning the range m_ℓ = -ℓ to ℓ. $\mathbf{L}$ and $\mathbf{L}_z$ act upon the state $|n, \ell, m_\ell\rangle$ [58]. Additional splitting of the energy levels caused by coupling of the electron spin and orbital angular momentum is known as fine structure. There is a further correction to the energy levels arising from the interaction between the

magnetic moments of the nucleus and electron spin. Since we only consider atoms within strong external electric fields, where the energy shift due to the Stark effect ΔE_{Stark} is much greater than the shift due to fine and hyperfine structure, we will neglect to consider these effects when discussing the linear Stark effect in the next section.

A transition between two energy levels, from an initial state $|n, \ell, m\rangle$ to a final state $|n', \ell', m'\rangle$, occurs after excitation, and subsequently radiative decay from this excited state is observed. The probability of a transition between two states is given by $|\mu_{i\to f}|^2$, where $\mu_{i\to f}$ is the matrix element of the electric dipole moment. The intensity of transitions between the initial state ψ_i and final state ψ_f,

$$\mu_{i\to f} = \langle n', \ell', m' | \, \mathbf{D} \, | n, \ell, m \rangle \,, \tag{2.3}$$

where $\mathbf{D}$ is the electric dipole operator, $\mathbf{D}$ = -e$\mathbf{r}$. Whether this matrix element is non-zero depends on the particular values of (ℓ,m) and (ℓ',m') and is governed by selection rules which conserve angular momentum [59]. The selection rules for allowed electric dipole transitions,

$$\begin{aligned} \Delta\ell &= \pm 1, \\ \Delta m = 0 \quad \text{or} \quad \Delta m &= \pm 1. \end{aligned} \tag{2.4}$$

Transitions with $\Delta m = 0$, with a component of the electric field of incident radiation along the z-axis (linear polarisation) are labelled as π transitions, and transitions with $\Delta m = \pm 1$, with the electric field within the xy plane (circular polarisation) are labelled as σ transitions [60]. This nomenclature will be used later when labelling transitions within the Stark multiplet.

Although there are a wealth of spectral lines to observe within fusion plasmas, we will focus on the n=3 $\to$ n=2 atomic transition, which is the α component of the Balmer line series. In Hydrogen, H_α transitions occur at λ=656.3nm, and in Deuterium (D_α) at λ = 656.1nm, which are within the red visible part of the electromagnetic spectrum. Now we will consider shifts to atomic energy levels in the presence of external magnetic and electric fields.

2.1.1 The Zeeman Effect

Atoms within an external magnetic field exhibit splitting of the atomic energy levels. The strength of the perturbation due to the external magnetic field is,

$$H_{\text{Zeeman}} = -\boldsymbol{\mu} \cdot \mathbf{B}, \tag{2.5}$$

where $\mathbf{B}$ is the magnetic field, and μ is the magnetic moment of the atom. External magnetic fields induce splitting of the Balmer-α line, with the polarisation state depending on the orientation of the magnetic field. Other impurity species, particularly those with transition lines close to H_α, for example the CII doublet lines at $\lambda = 657.8$nm and $\lambda = 658.3$nm [61], within the plasma also produce Zeeman split polarised line emission [62]. In tokamaks, the magnetic field strength is large enough to be considered within the Paschen-Back regime where spin and orbital angular momentum are decoupled [63], and again we neglect fine (and hyperfine) splitting. The energy separation between Zeeman (Paschen-back) split states is given by,

$$\Delta E_{\text{Zeeman}} = \mu_{\text{B}} \boldsymbol{B} \left(m_\ell + 2m_s\right), \tag{2.6}$$

where μ_{B} is the Bohr magneton and m_s is the magnetic spin quantum number.

2.1.2 The Stark Effect

The motional electric field, generated by high velocity beam atoms moving across the magnetic field, is significantly larger than the magnetic field in the plasma. In this case the Stark effect dominates over the Zeeman effect for D_α emission lines from excited neutral beam atoms. For treatment of the Stark effect in atoms, it is useful to use a parabolic co-ordinate system (ξ, ζ, ϕ) as Schrodinger's equation is separable and the energy shift due to the Stark effect can be retrieved to first order[64]. This leads to the introduction of electric quantum numbers n_1 and n_2 which relate to n via

$$\begin{aligned} n &= n_1 + n_2 + |m_\ell| + 1, \\ k &= n_1 - n_2. \end{aligned} \tag{2.7}$$

These electric quantum numbers are introduced at the expense of the quantum number l, which is no longer a good quantum number. The energy separation due to Stark splitting is given by,

$$\Delta E_{\text{Stark}} = -\frac{3}{2} nkea_0 \boldsymbol{E} \tag{2.8}$$

where $\boldsymbol{E}$ is the electric field strength, a_0 is the Bohr radius, e is the elementary charge and n and k are as defined in equation 2.7. Transitions and spectral lines for the pure Stark effect (a single electric field, with a preferred axis along **E**) are shown in Fig. 2.1. These 9 bright transition lines combine to form the well known Stark split multiplet. The separation of the π wings and central σ line depends on the strength of the electric field.

The Lorentz electric field strengths in question for MAST and other small tokamaks is around $\mathrm{E_L} = 10^6 \mathrm{V/m}$, and so only the linear Stark effect is considered for the devices. However, on ITER where neutral beam energies are on the order of 1MeV and upwards, a Lorentz field strength of $\mathrm{E_L} \approx 10^8 \mathrm{V/m}$ can be anticipated. The quadratic Stark effect becomes more significant with increasing field strength, and must be included to calculate the correct line intensity ratios [65].

2.1.3 Motional Stark Effect

High energy neutral atoms are injected into the plasma and their movement through the magnetic field induces a strong Lorentz electric field $\mathbf{E}_L$ in the rest frame of the neutral beam atoms. The total electric field **E** in this rest frame is then,

$$\begin{aligned} \mathbf{E} &= \mathbf{E}_L + \mathbf{E}_R \\ \mathbf{E} &= \boldsymbol{v_b} \times \mathbf{B} + \mathbf{E_R} \\ \mathbf{E} &= v_b \hat{e}_v \times (B_{\mathrm{R}} \hat{e}_{\mathrm{R}} + B_\phi \hat{e}_\phi + B_z \hat{e}_z) + E_R \hat{e}_R \end{aligned} \tag{2.9}$$

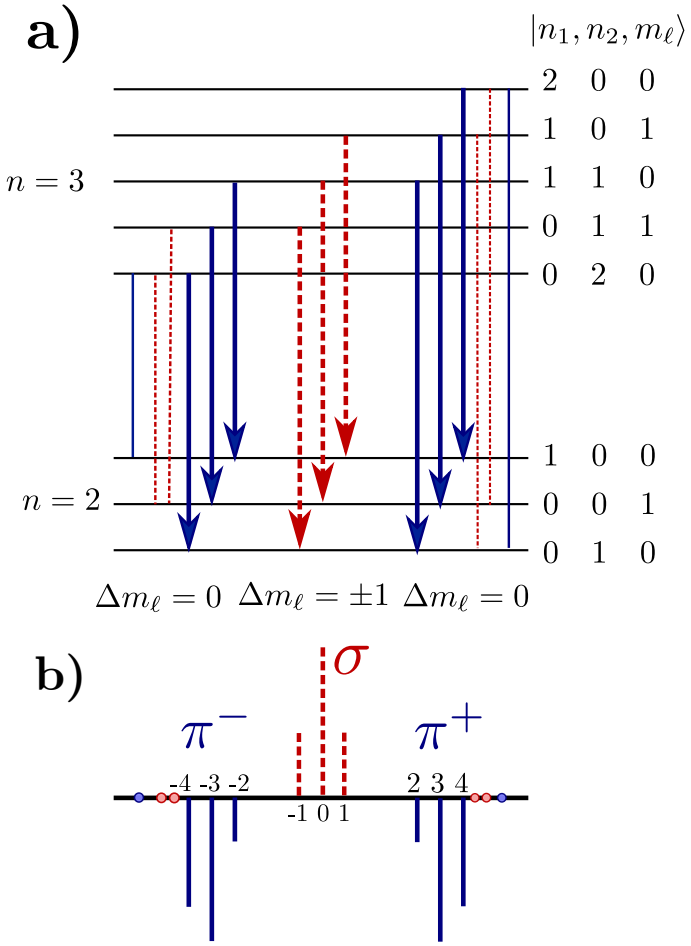

Figure 2.1: **a)** Transitions between the Balmer-α Stark split n_1,n_2,m_ℓ states. **b** Sigma σ transitions (red dashed) are the central component of the multiplet, with two pi π wings (blue solid) and emission from these Stark split states is orthogonally polarised. Considering the pure linear Stark effect, there are a total of 15 possible transition lines, with 9 bright lines which produce a multiplet. Additional lines which cannot be resolved are shown as small circles. Figures re-produced from [64].

where v_b is the neutral beam velocity and $\mathbf{E_R}$ is known as the radial electric field. This E_R component arises due to force balance and depends on plasma poloidal and toroidal rotation and diamagnetic effects (pressure gradient). Details on the radial electric field component, and the impact on MSE measurements, can be found in section 3.2.3.

In the simple Stark effect described in section 2.1.2, emission from π and σ lines is orthogonally polarised. The presence of both **E** and **B** fields, as is

the case for the Motional Stark effect in fusion plasmas, there is no longer a preferred axis of symmetry along the electric field as is the case in the pure Stark effect. With the loss of symmetry the polarisation of σ transitions may change, most noticeably in low density plasmas. There has been some effort to describe the polarisation state in simultaneous electric and magnetic fields more accurately[49], as the Stark-Zeeman lines may have different polarisation properties which could change the measured polarisation angle in some particular conditions, such as beam-into-gas discharges[1] (BIG). Discrepancies in the measured π/σ line intensity ratios during BIG calibrations were observed [66], where the neutral beam is injected into low density gas with a known magnetic field. This is due to non-equal population of the upper n=3 states at low plasma densities which cannot be described using Boltzmann statistics. On MAST it was observed that the π/σ ratio was significantly enhanced in both BIG and some low density plasma pulses[37], favourably leading to an improved signal to noise ratio if polarisation angle measurements are made using the π component of the multiplet. This variation in the linear polarisation in plasma discharges can be minimised with careful choice of diagnostic geometry (ie. using a view tangential to magnetic flux surfaces) and neutral beam injection angle close to 45° with respect to the magnetic field. Naturally if using BIG discharges as a calibration method, then this effect should be considered. But, as this optimal configuration was implemented for the MSE system on MAST and continued for MAST-U, we anticipate this effect to be negligible in plasma discharges and does not impact the design of the imaging MSE system for MAST-U presented later in chapter 4.

Neutral beam injection systems operate at high energies and inject fast neutrals into the plasma which are generated through acceleration of an ion source through a large potential difference. Subsequently they are re-neutralised

[1]The vessel is filled with a low density neutral gas ($n \approx 10^{16}$-$10^{18}\mathrm{m}^{-3}$ compared to densities of $\approx 10^{20}\mathrm{m}^3$ for typical MAST-U plasma discharges) and the magnetic field is produced only by external coil currents. BIG shots can be used for an absolute calibration of the polarisation angle including any in-vessel systematic uncertainties due to finite collection volume effects, Faraday effect induced by toroidal field coils close to the collection optics and the 3D viewing geometry.

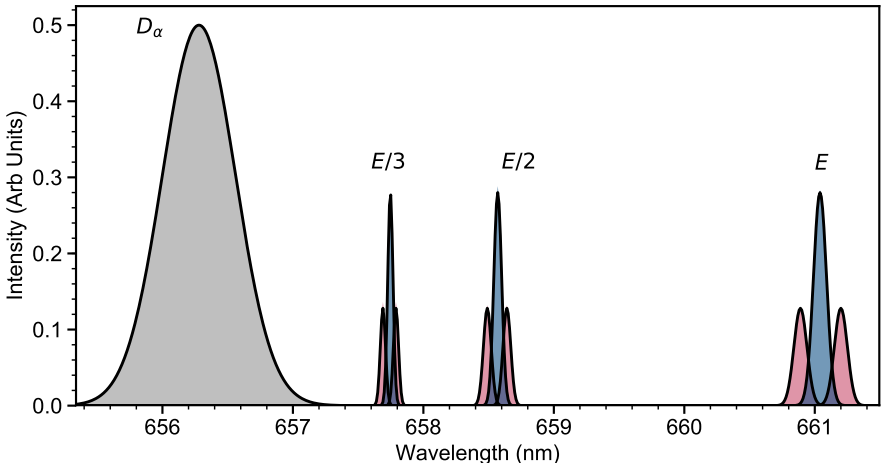

Figure 2.2: Example MSE spectrum, for a magnetic field strength $|B| \approx 0.5$T and a 75keV neutral beam. The spectrum includes the full, half and third energy components. The MSE multiplet is Doppler red shifted away from the D_α peak due to the fast movement of neutral atoms away from the line of sight. σ (blue) and π (red) lines include some artificial broadening for visualisation. Due to the low magnetic field the π and σ components overlap, resulting in a reduced linear polarisation fraction.

resulting in a source of fast neutrals deposited into the plasma. Additional molecular ions D_2^+ and D_3^+ are generated in the ion source. When neutralised and dissociated, the constituent atoms have fractional half and third energies E_2 and E_3 depending on their original ion mass, and produce similar multiplet structures at different wavelengths as shown in Fig. 2.2. These full, half and third energy multiplets are Doppler shifted away from the main passive D_α peak, with the wavelength shift $\Delta\lambda_\mathrm{D}$ dependent on both the beam velocity and the viewing angle to the neutral beam,

$$\Delta\lambda_D = -\frac{v_\mathrm{b}}{c}\lambda_{D_\alpha}\hat{e}_v \cdot \hat{e}_k, \tag{2.10}$$

where v_b is the velocity of neutral beam atoms, $\hat{e}_v$ is the beam unit vector and $\hat{e}_k$ is the emission unit vector. A typical spectrum is shown in Fig. 2.2 including all energy components and plasma D_α emission. The diagnostic lines of sight are chosen for good spatial resolution by maximising tangency to flux surface, and such that the Doppler shift provides significant separation between the energy components, and any nearby impurity lines.

The polarisation orientation of emission from σ transitions with respect to the

electric field is related to the local magnetic pitch angle $\gamma_{\mathrm{p}} = \arctan(B_\theta/B_\phi)$, assuming that $\mathbf{E}\perp\mathbf{B}$. The polarisation angle γ measured is then,

$$\tan(\gamma+\pi) = \frac{\hat{E}\cdot\hat{e}_{\mathrm{Z}}}{\hat{E}\cdot\hat{e}_{\mathrm{H}}} \tag{2.11}$$

where $\hat{e}_{\mathrm{z}}$ is the vertical unit vector, and $\hat{e}_{\mathrm{H}}$ is the horizontal unit vector. The general equation for out of the mid-plane light of sight and neutral beam,

$$\tan\gamma = \frac{A_0 B_z + A_1 B_R + A_2 B_\phi}{A_3 B_z + A_4 B_R + A_5 B_\phi}. \tag{2.12}$$

The A coefficients derived from the geometry are given as,

$$\begin{aligned}
A_0 &= -\cos\beta\cos\nu + \frac{E_{\mathrm{R}}}{v_{\mathrm{b}}\sqrt{B_R^2+B_z^2}}\cos(\alpha+\beta),\\
A_1 &= -\sin(\alpha+\beta)\sin\nu,\\
A_2 &= \cos(\alpha+\beta)\sin\nu,\\
A_3 &= -\sin\beta\cos\nu\sin\mu + \frac{E_{\mathrm{R}}}{v_{\mathrm{b}}\sqrt{B_R^2+B_z^2}}\sin\mu\sin(\alpha+\beta),\\
A_4 &= \cos(\alpha+\beta)\sin\nu\sin\mu + \cos\alpha\cos\nu\cos\mu - \frac{E_{\mathrm{R}}}{v_{\mathrm{b}}\sqrt{B_R^2+B_z^2}}\cos\mu,\\
A_5 &= \sin\alpha\cos\nu\cos\mu + \sin(\alpha+\beta)\sin\nu\sin\mu,
\end{aligned} \tag{2.13}$$

where α is the angle between the toroidal direction and the neutral beam vector, β is the angle between the neutral beam vector and the line of sight vector, μ and ν are the out of mid-plane angles for the line of sight and neutral beam vectors respectively. Further details of the derivation have been described elsewhere [30, 41, 67]. The neutral beam and diagnostic lines of sight for the MSE system on MAST are situated effectively at the mid-plane and ν, μ and $B_R \approx 0$. Coefficients A_1, A_2, A_3 become negligible, with equation 2.12 reducing to,

$$\tan(\gamma) = \frac{B_z\left[\cos\beta + (E_{\mathrm{R}}/v_b)\cos(\alpha+\beta)\right]}{-B_\phi\sin\alpha} \tag{2.14}$$

A simple relation using the geometric A coefficients to the magnetic pitch angle $\tan\gamma_p \approx -\frac{A_0}{A_5}\tan\gamma$.

Finally the polarisation angle is used in combination with other diagnostic measurements in equilibrium reconstruction codes, such as EFIT++[68], to derive quantities of interest (*e.g.* q and current profiles, the poloidal flux function.) We will discuss the relationship between equilibrium reconstruction and MSE measurements across the chapters in this thesis.

2.2 Stokes-Mueller Formalism

To describe the polarised line emission from the MSE multiplet, we must introduce an appropriate mathematical description of polarised light. The polarisation state of electromagnetic radiation is given by the electric field vectors E_x and E_y oscillating along a plane transverse to the direction of wave propagation. Fully polarised light is described using these vectors combined to form a Jones vector. However, Jones vectors only describe *coherent* fully polarised light in terms of the complex amplitudes of the electric field, averaging over phase information. Light emission from atomic processes with fusion plasmas is not always fully polarised. Convenient notation for partially polarised and incoherent light sources is the Stokes vector S[69],

$$S = \begin{pmatrix} S_0 \\ S_1 \\ S_2 \\ S_3 \end{pmatrix} \begin{pmatrix} \langle E_x^* E_x + E_y^* E_y \rangle \\ \langle E_x^* E_x - E_y^* E_y \rangle \\ \langle E_x^* E_y + E_y^* E_x \rangle \\ \langle i(E_y^* E_x - E_x^* E_y \rangle \end{pmatrix} = I_0 \begin{pmatrix} 1 \\ P\cos(2\gamma)\cos 2\chi \\ P\sin(2\gamma)\cos 2\chi \\ P\sin 2\chi \end{pmatrix} \tag{2.15}$$

where I_0 is the total light intensity, P is the polarised fraction, γ is the polarisation angle and ellipticity angle χ. The degree of polarisation (DOP) is then calculated as,

$$DOP = \frac{\sqrt{S_1^2 + S_2^2 + S_3^2}}{S_0} \tag{2.16}$$

The evolution of the electric field vector is shown on the polarisation ellipse in Fig. 2.3. Evolution between polarisation states are shown on the Poincaré sphere. Linear polarisation states are described around the equator within

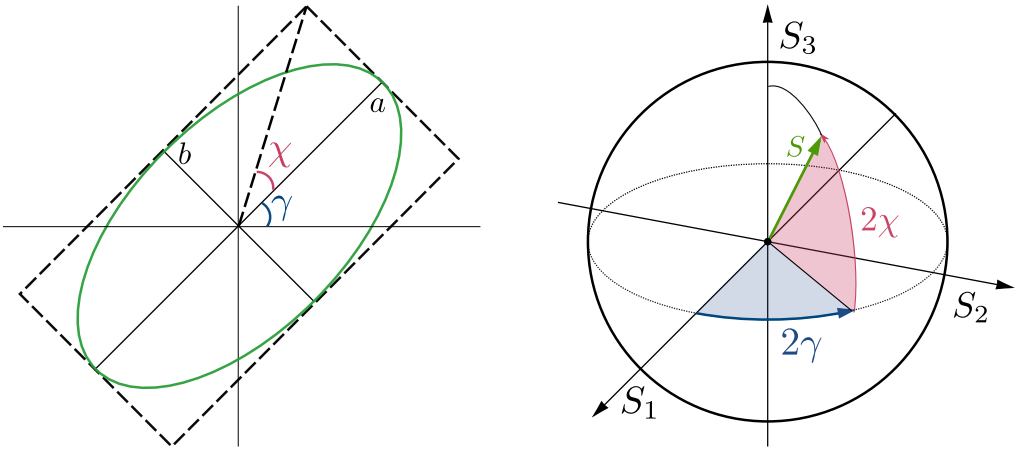

Figure 2.3: **Left:** The polarisation ellipse which defines the ellipicity angle χ and the orientation angle γ which describe the polarisation state of the electric field vector and a and b are the major and minor semi-axes of the ellipse.
Right: Depiction of the polarisation state of a Stokes vector S on the Poincaré sphere. Evolution around the equator represents variation in linear polarisation. Rotations toward the poles describes circular polarisation. The Poincaré sphere is useful for visualisation of the Stokes vector evolution through optical components.

the xy plane and circular polarisation states are represented by a rotation towards the poles, with the right and left handedness given along the ±z axis. The Poincaré sphere is a useful tool for visualising the effect on the polarisation state of light through optical components. A full overview of Stokes-Mueller analysis can be found in many textbooks [69][70].

2.3 Mueller Matrix Formalism

The interaction of polarised light given by a Stokes vector **S** with an optical component, such as an optical retarder or polariser, is described using Mueller matrix formalism. The output Stokes vector $\mathbf{S}_{out}$,

$$\mathbf{S}_{\text{out}} = \mathbf{M} \cdot \mathbf{S}_{\text{in}} \tag{2.17}$$

This formalism will be used throughout this thesis, where **M** is the Mueller matrix for a given optical component. Finally, Mueller matrices can describe

optical components at any arbitrary orientation angle using the notation $\mathbf{R}(\text{-}\theta)\cdot\mathbf{M}\cdot\mathbf{R}(\theta)$ where $\mathbf{R}(\theta)$ is the rotation matrix,

$$\mathbf{R}(\theta) = \begin{pmatrix} 1 & 0 & 0 & 0 \\ 0 & \cos 2\theta & \sin 2\theta & 0 \\ 0 & -\sin 2\theta & \cos 2\theta & 0 \\ 0 & 0 & 0 & 1 \end{pmatrix}. \tag{2.18}$$

Mueller matrices for many optical components can be multiplied to construct a full Mueller matrix describing the diagnostic techniques presented in this thesis. A few Mueller matrices common to both polarimetry techniques are shown here. A Mueller matrix for a general waveplate $\mathbf{W}(\phi)$ applying an arbitrary delay ϕ and a horizontal fast axis (θ=0),

$$\mathbf{W}(\phi) = \begin{pmatrix} 1 & 0 & 0 & 0 \\ 0 & 1 & 0 & 0 \\ 0 & 0 & \cos\phi & \sin\phi \\ 0 & 0 & -\sin\phi & \cos\phi \end{pmatrix}. \tag{2.19}$$

A pure polariser $\mathbf{P}$ with polarisation axis along the horizontal,

$$\mathbf{P} = \frac{1}{2}\begin{pmatrix} 1 & 1 & 0 & 0 \\ 1 & 1 & 0 & 0 \\ 0 & 0 & 0 & 0 \\ 0 & 0 & 0 & 0 \end{pmatrix}. \tag{2.20}$$

2.4 Polarisation Measurement Techniques

Initially a spectrometer was used to measure MSE emission on the JET tokamak[35]. However, the photo-elastic modulator (PEM) polarimetry technique became the standard method relatively quickly, after boasting improved spatial and temporal resolution, where measurements were used to infer the q profile and the value of q on axis during sawtooth oscillations [34].

Achieving measurements with the MSE diagnostic at the accuracy required, both spatially and temporally, for physics studies can be challenging on fusion

devices. Long optical trains require multiple mirrors, which change the polarisation state of incident light depending on the mirror surface reflectivity[71]. Degradation in the optical properties of mirrors due to plasma deposition, which can lead to drifts in the measured polarisation[72]. Polarimetry diagnostics are also sensitive to *any* polarised light within the wavelength region of interest, and so background polarised light can contribute to the measured emission. In this section we outline the two MSE diagnostic techniques focussed on in this thesis.

2.4.1 Dual Photo-elastic Modulator (PEM) Polarimetry

The conventional MSE diagnostic uses photo-elastic modulators and an analysing polariser to convert polarisation information into an intensity modulation in the time domain. The PEM fused silica glass plate is driven at its resonant frequency with a piezoelectric transducer and exhibits stress induced uni-axial birefringence. Details of PEM technology can be found in [73]. Two PEMs, as shown in Fig.2.4, are required to measure the full 4 Stokes vector components, as linearly polarised light parallel to the fast axis of a single PEM would be insensitive to the modulation frequency[72, 74]. Conventional MSE polarimeters use two PEMs with their orientation axes 45° apart, with an analysing polariser oriented at 22.5°. The effect of the two PEMs is given by,

$$\boldsymbol{S_{\text{out}}} = \mathbf{R}(\pi/8)\cdot\mathbf{P}\cdot\mathbf{R}(-\pi/8)\cdot\mathbf{R}(\pi/4)\cdot\mathbf{W}(A_2\cos(\lambda_2 t))\cdot\mathbf{R}(-\pi/4)\cdot\mathbf{W}(A_1\cos(\lambda_1 t))\cdot\boldsymbol{S_{\text{in}}} \tag{2.21}$$

where the output intensity on the detector is,

$$\begin{aligned} I_{\text{out}} = \frac{1}{2}\big(S_0 + \frac{S_1\cos\left[A_2\cos\left(\lambda_2 t\right)\right]}{\sqrt{2}} + \\ \frac{S_2}{\sqrt{2}}[\cos\left[A_1\cos\left(\lambda_1 t\right)\right] + \sin\left[A_1\cos\left(A_1 t\right)\right]\sin\left[A_2\cos\left(\lambda_2 t\right)\right]] + \\ \frac{S_3}{\sqrt{2}}[\sin\left[\left(A_1\cos\left(\lambda_1 t\right)\right] - \cos\left[A_1\cos\left(\lambda_1 t\right)\right]\sin\left[A_2\cos\left(\lambda_2 t\right)\right]]\big) \end{aligned} \tag{2.22}$$

where the retardance of each PEM is $A_1 \cos(\omega_1 t)$ and $A_2 \cos(\omega_2 t)$, ω_1 and ω_2 are the transducer driving frequencies and the Stokes components are given in equation 2.15. Equation 2.22 can then be decomposed into the amplitudes of the PEM harmonics, decomposing the trigonometric terms into Bessel functions of the first kind [2][75],

$$\cos[z\cos(\omega t)] = J_0(z) + 2\sum_{n=1}^{\infty}(-1)^n J_{2n}(z)\cos(2n\omega t), \tag{2.23}$$

$$\sin[z\cos(\omega t)] = 2\sum_{n=1}^{\infty}(-1)^n J_{2n-1}(z)\cos((2n-1)\omega t). \tag{2.24}$$

The intensity of the harmonics of interest are,

$$\begin{aligned} I_{2\omega_1} &= \frac{-I_0 P\cos(2\gamma)J_2(A_1)}{\sqrt{2}}, \\ I_{2\omega_2} &= \frac{-I_0 P\sin(2\gamma)J_2(A_2)}{\sqrt{2}}, \\ I_{4\omega_1} &= \frac{I_0 P\sin(2\gamma)J_4(A_1)}{\sqrt{2}}, \\ I_{4\omega_2} &= \frac{I_0 P\cos(2\gamma)J_4(A_2)}{\sqrt{2}}. \end{aligned} \tag{2.25}$$

The polarisation angle is retrieved using the intensity of the second (or fourth) harmonics,

$$\gamma = \frac{1}{2}\arctan\left(\frac{S_2}{S_1}\right) = \frac{1}{2}\arctan\left(\frac{J_2(A_2)I_{2\omega_1}}{J_2(A_1)I_{2\omega_2}}\right). \tag{2.26}$$

In most fusion applications the large aperture PEMs are driven at 20kHz and 23kHz respectively in a dual PEM configuration. The retardances for both PEMs are usually set to maximise the amplitude of J_2, at a retardance of 175°, but for the MAST system the retardances are set slightly higher at 220° to entirely suppress the amplitude of the first Bessel function J_1. This is due to frequencies which appear in addition to the harmonic frequencies at 3kHz and 43kHz leading to,

[2]These identities are derived by decomposing the Jacobi–Anger expansion $e^{iz\cos\omega t} = \sum_{n=-\infty}^{\infty} i^n J_n(z)e^{in\omega t}$ into real-valued expressions.

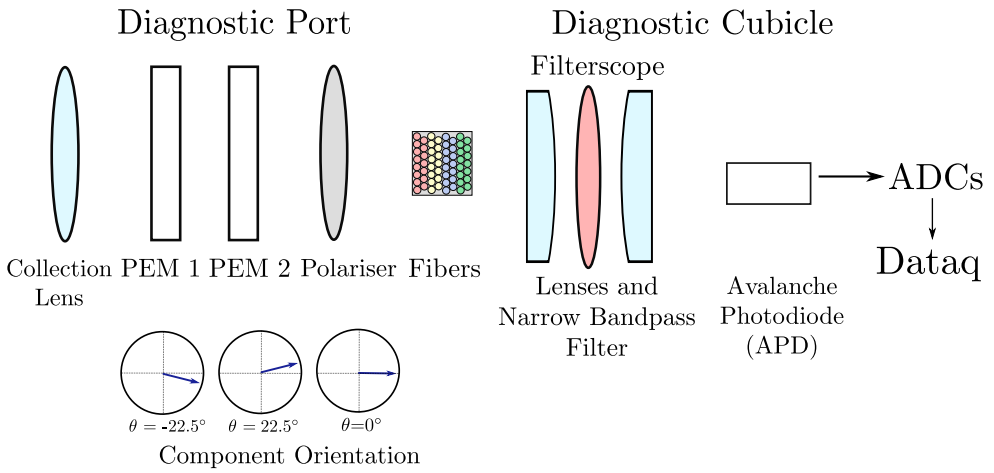

Figure 2.4: Layout of the conventional MSE system from the viewing port to the diagnostic cubicle. Polarised neutral beam emission is modulated by the PEMs and is then transmitted to the diagnostic cubicle via optical fibres. Narrow-band filters (FWHM = 0.12 nm on the MAST MSE system) select either a π or σ line within the MSE multiplet.

$$I_{\omega_1+\omega_2} = I_{\omega_1-\omega_2} = \frac{I_0 P \sin 2\gamma J_1(A_1) J_1(A_2)}{\sqrt{2}} \tag{2.27}$$

Suppressing $I_{\omega_1-\omega_2}$ by running at a higher retardance, effectively minimising J_1, then doubles the available frequency bandwidth to 3kHz [37].

The full optical arrangement for a dual PEM polarimeter is shown in Fig. 2.4 starting with the collection optics located at the tokamak to the filterscopes and components in the diagnostic cubicle. After amplitude modulation with the polariser, light is transmitted through optical fibres to individual filterscopes. The filterscope consists of a collection of lenses and a narrowband interference filter used to select either π or σ component of the Stark multiplet, which is then collected by avalanche photodiodes (APDs). To resolve up to the fourth harmonic of the PEM frequencies, digitization of the APD signal is required up to at least 92kHz, and so the bandwidth of the amplifiers for the APDs is set to 250kHz [37]. The polarisation information can then be retrieved in software rather than using analogue lock-in amplifiers, allowing for the data to be synthesised using different time windows. Additionally, the PEM reference wave-forms are digitized for use as the reference signal

within the lock-in amplifier routine. This then recovers the PEM retardances to check these are set correctly by the PEM controllers. Further details on the PEM retardance settings on MAST can be found in section 3.2.2.

Conventional MSE systems are installed and operating on the majority of fusion devices. They are currently the only diagnostic which provides spatially resolved both real time[76] and high temporal resolution measurements of the magnetic pitch angle across the radial extent of the plasma. In Chapter 4 we will discuss how both the conventional MSE system and relatively recent coherence imaging interferometry technique is adapted for low field spherical tokamaks.

2.4.2 Imaging MSE

An imaging based polarization interferometry technique has been developed within the last decade for fusion applications[47, 49]. Obvious advantages of an imaging system over a fibre based conventional MSE system include:

- Obtaining 2D spatially resolved measurements and a significant boost in the overall number of measurements. Although fibre based systems measure across the vertical extent of the beam, these measurements are averaged to a single 1D measurement and the vertical spatial information is lost. Many pixels in an imaging based system can be binned to improve the shot noise uncertainty and provide a 2D grid of measurements.

- All available signal is used, as a wider bandpass filter is used to encompass the whole MSE multiplet. An added bonus of the wide filter is the imaging MSE system can adequately handle large changes in the neutral beam voltage without the requirement of tracking wavelength shifts using tilted or temperature controlled filters.

- Additional plasma parameters can be inferred from polarisation angle measurements in the vertical extent, such as the poloidal flux surface shape, the shafranov shift δ of the flux surfaces [77] and tracking of the magnetic axis position in the RZ plane. The addition of this 2D

resolved data into equilibrium reconstruction codes should improve the inferred q and current profiles necessary for MHD stability analysis.

Uni-axial Birefringent Crystals

Key components in the IMSE polarimeter are birefringent crystal waveplates, made from materials such as Alpha-Barium Borate (α-BBO) and Lithium Niobate ($LiNbO_3$). These crystals are uni-axial, exhibiting different refractive indices along the ordinary n_e and extraordinary n_o axes. The refractive indices are wavelength dependent, and are calculated using the Sellmeier equations for α-BBO[78],

$$\begin{aligned} n_o(\lambda)^2 &= 2.7359 + \frac{0.01878}{\lambda^2 - 0.01822} - 0.01354\lambda^2 \\ n_e(\lambda)^2 &= 2.3753 + \frac{0.01224}{\lambda^2 - 0.01667} - 0.01516\lambda^2 \end{aligned} \tag{2.28}$$

where λ is the incident wavelength measured in microns. From Eq. 2.28, the birefringence B_0 and dispersion parameter κ_0 can be calculated for the center of mass wavelength of the emission λ_0.

As linearly polarised light passes through the waveplate, a phase shift is introduced between the incident ordinary and extraordinary rays,

$$\phi(\lambda) = \frac{2\pi L B(\lambda)}{\lambda} \tag{2.29}$$

where $B(\lambda) = n_e(\lambda) - n_0(\lambda)$ is the birefringence, L is the thickness of the crystal, λ is the wavelength of the incident light. Equation 2.29 holds for waveplates where the optic axis is within the plane of incidence known as *delay* plates, imposing a uniform delay across the crystal aperture. In *displacer* waveplates, the optic axis makes an angle to the crystal aperture, Θ, as shown in Fig. 2.5. The full general equation for the phase shift between the ordinary and extraordinary rays through a waveplate with arbitrary optical axis orientation is[79],

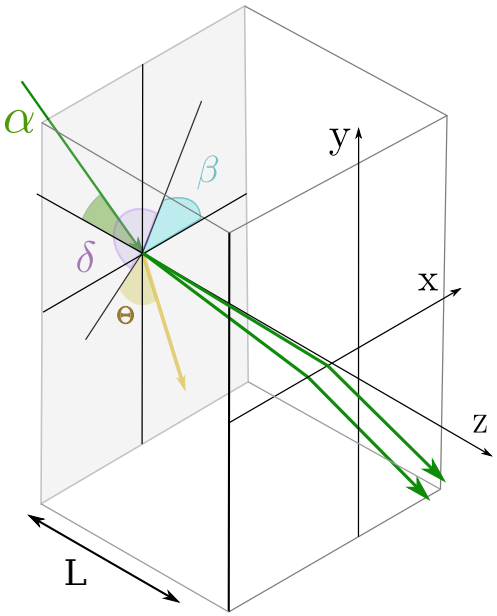

Figure 2.5: Ray propagating incidence angle α to the normal and the ordinary and extraordinary ray transmission through a uni-axial birefringent crystal with arbitrary optical axis orientation Θ. The angle β is the projection angle of the incidence ray into the face of the crystal and δ is the angle between the optic axis and the incidence plane. Adapted from [79].

$$\Delta\phi = \frac{2\pi L}{\lambda_0}\left(\left(n_0^2 - n^2\sin^2\alpha\right)^{\frac{1}{2}} + \frac{n(n_0^2 - n_e^2)\sin\Theta\cos\Theta\cos\delta\sin\alpha}{n_e^2\sin^2\Theta + n_0^2\cos^2\Theta}\right.$$
$$\left. + \frac{-n_0\{n_e^2(n_e^2\sin^2\Theta + n_0^2\cos^2\Theta - \left[n_e^2 - (n_e^2 - n_0^2)\cos^2\Theta\sin^2\delta\right]n^2\sin^2\alpha\}^{\frac{1}{2}}}{n_e^2\sin^2\Theta + n_0^2\cos^2\Theta}\right) \tag{2.30}$$

where Θ is the angle between the crystal surface and the optic axis, n_e and n_0 are the extraordinary and ordinary refractive indices, n is the refractive index of the medium, α and β are the spherical polar angles of incidence of the incoming ray, δ is the angle between the incidence plane and the plane of the optic axis. We also define that $\delta = \beta$ - ρ, where ρ is the orientation of the crystal. From this point we assume that $\rho = 90°$ such that the optic axis is aligned with the y axis. These angles are depicted in Fig. 2.5, which shows how the incident ray is projected onto the optic axis of the crystal, such that the applied phase shift is dependent on the incidence angles α and β. If the light is collimated through the crystal and focussed onto a sensor

at positions (x,y) in the focal plane depending on the focal length f of the focussing lens,

$$\begin{aligned} \tan\alpha &= \frac{\sqrt{x^2+y^2}}{f} \\ \tan\beta &= \frac{y}{x} \end{aligned} \tag{2.31}$$

then the phase shift is spatially dependent.

An approximation of Eq. 2.30 is derived through Taylor expansion in the incidence angle α to second order[49],

$$\begin{aligned} &\Delta\phi = \phi_{\text{offset}} + \phi_{\text{shear}} + \phi_{\text{hyperbolic}} \\ &\Delta\phi = -\frac{2\pi L\Delta n(\lambda)}{\lambda}\left(\cos^2\Theta + \frac{\sin(2\Theta)\sin\beta}{\bar{n}}\alpha + \frac{\sin^2\Theta + \frac{1}{2}\cos 2\beta\cos^2\Theta}{\bar{n}^2}\alpha^2 + \mathcal{O}(\alpha^3)\right) \end{aligned} \tag{2.32}$$

This leads to three distinct phase terms; A phase 'offset' ϕ_{offset} independent of incidence angle, a linear phase shear ϕ_{shear} and quadratic term $\phi_{\text{hyperbolic}}$. Rewriting in terms of positions (x, y) on the sensor in the focal plane,

$$\begin{aligned} \phi_{\text{offset}}(\lambda) &= -\frac{2\pi L\Delta n(\lambda)}{\lambda}\cos^2\Theta \\ \phi_{\text{shear}}(\lambda, y) &= -\frac{2\pi L\Delta n(\lambda)\sin 2\Theta}{\lambda\bar{n}f}y = k_y y \\ \phi_{\text{hyperbolic}}(\lambda, x, y) &= \frac{2\pi L\Delta n(\lambda)}{\lambda 4\bar{n}^2 f^2}(3-\cos 2\Theta)x^2 - ((3\cos 2\Theta)-1)y^2) \end{aligned} \tag{2.33}$$

The spatial frequency k_y sets the frequency of the interference fringes. This first order term provides a linear variation in the phase delay along one axis of the crystal. Finally, the second order term $\phi_{\text{hyperbolic}}$ introduces a hyperbolic pattern in the phase delay across the crystal.

These total phase calculated with equation 2.30 is shown in Fig. 2.6, alongside the linear delay and hyperbolic terms (Eq. 2.32) for an α-BBO crystal of thickness L=5.8mm with an optical axis at an angle Θ=30°. This second order effect is small for small values of α and thin displacer plates. However for thick displacer places this term leads to curvature of the interference fringes, which can be detrimental to the Fourier demodulation. In Chapter

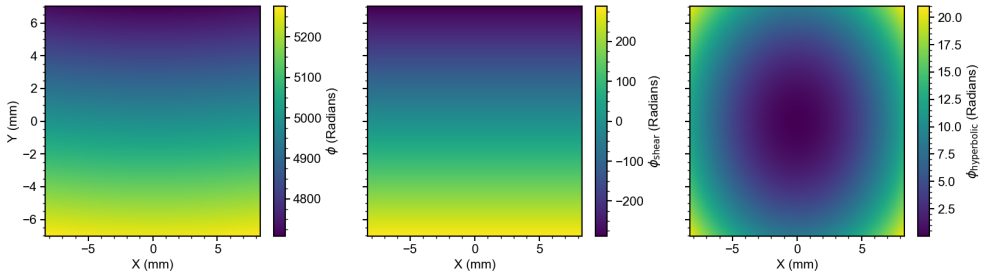

Figure 2.6: Left: Total phase delay imposed for incident light λ=660nm by an α-BBO crystal with properties: L=5.8mm, Θ=30°, ρ=90°, focussed onto the sensor of a PCO.edge camera using an f = 85mm focal length lens. Middle: Phase shear term calculated using Eq. 2.32. Right: Hyperbolic phase term which arises due to the second order dependence of the delay on the incidence angle α.

4 we will explore the significance of these second order effects for the forward modelled MAST-U IMSE system and how to reduce severity of the fringe curvature through careful choice of the crystal materials and the 'field widening' technique.

IMSE Principle

A basic imaging polarimeter setup to measure linearly polarised light is shown in Fig. 2.7. The system consists of a quarter waveplate, polariser orientated 45° from the axis of a displacer waveplate and a focussing lens.[3]

The displacer imposes a phase delay $\phi(y)$ dependent on the incidence angles α and β. This produces an interferogram in the focal plane, where the fringe contrast depends on the angle between the measuring polarised and the input polarisation. With this simple setup and incident light described by equation 2.15, assuming zero ellipticity, the interferometer output is,

[3]It might be illuminating to think of the imaging MSE system as a Michelson interferometer; The displacer plate introduces a lateral shift between the two polarised ray components, analogous to the polarising beam splitter, and the delay plate provides the optical path difference. The ray components are then recombined to form an interference pattern in the image plane. The interference fringe pattern orientation depends on whether the lateral shift is applied in the horizontal or vertical direction.

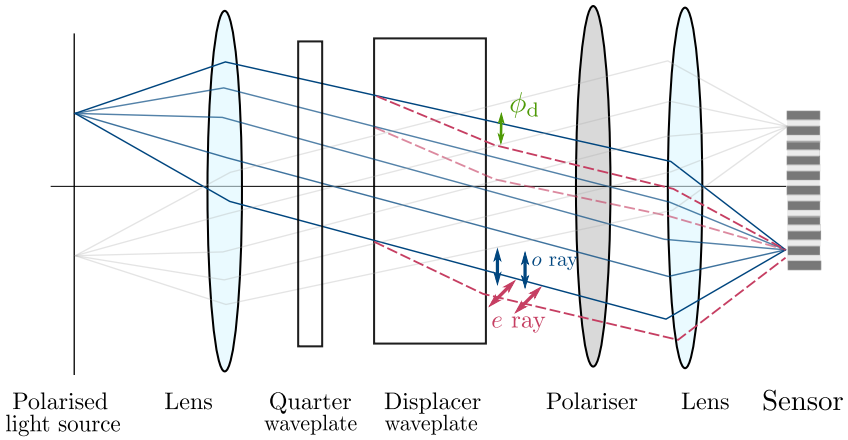

Figure 2.7: A polarimeter sensitive to linearly polarised light, using a two lens system with focal lengths f_1 and f_2 respectively. A quarter waveplate (QWP) orientated at 45° leaves the polarimeter sensitive only to linearly polarised light. The displacer plate orientated at 90° introduces a phase shift ϕ_D between the ordinary and extra ordinary rays, which are recombined by a measuring polariser at 45°. This produces an interferogram on the camera sensor.

$$\begin{aligned} \boldsymbol{S}_{\mathbf{IMSE}} &= \mathbf{P} \cdot \mathbf{R}\left(-\frac{\pi}{4}\right) \cdot \mathbf{W}\left(\phi(y)\right) \mathbf{R} \cdot \left(\frac{\pi}{4}\right) \cdot \mathbf{W}\left(\frac{\pi}{2}\right) \cdot \mathbf{R}\left(\frac{\pi}{4}\right) \cdot \mathbf{S}, \\ \boldsymbol{S}_{\mathbf{IMSE}}(\lambda) &= \frac{1}{2}\left(S_0 - S_1 \sin\phi(\lambda, y) + S_2 \cos\phi(\lambda, y)\right), \end{aligned} \tag{2.34}$$

where $\phi(y)$ is the delay applied by the displacer, which varies linearly in the vertical direction and only very weakly in the horizontal direction across the crystal. From equation 2.34 the delay acts as a sinusoidal filter over the polarised Stokes components, Integrating the interferometer output over the MSE spectrum, *i.e.* $\int_0^\infty S(\lambda) f(\lambda) d\lambda$, where $f(\lambda)$ is the bandpass filter transmission function,

$$\boldsymbol{S}_{\mathbf{IMSE}} = \frac{I_0}{2}\left(1 + \zeta_l \sin(2\gamma - \phi(y))\right) \tag{2.35}$$

where ζ_l is the *fringe contrast*. The fringe contrast is a measure of the brightness of the fringes, and has a complex relationship with respect to the inherent coherence of the emission lines as well as the fringe contrast set by the interferometer components. The fringe contrast is given by,

$$\zeta_l(\lambda) = \frac{1}{I_0}\left|\int_0^\infty I(\lambda)p(\lambda)\exp\left(i\phi(\lambda)\right)d(\lambda)\right| \tag{2.36}$$

where $I(\lambda)$ is the total emission intensity, $p(\lambda)$ is the linearly polarised fraction, $\phi(\lambda)$ is the delay imposed by the interferometer components. Equation 2.36, and therefore the fringe contrast, is the amplitude of the Fourier transform of the individual emission lines in the MSE multiplet and the imposed sinusoidal filter.

The contrast becomes an important parameter when considering that the MSE multiplet consists of orthogonally polarised σ and π emission, which when summed is net unpolarised and results in zero net spectral contrast, and therefore zero fringe contrast. Therefore we choose to maximise the difference in the spectral contrast $\zeta_\pi - \zeta_\sigma$ to produce a net polarised signal. Introducing a sinusoidal filter to maximise the coherence of the multiplet is achieved through careful consideration of the displacer plate properties. The maximum achievable contrast (assuming the waveplate properties target the net spectral contrast) is limited by the available signal level and spectral line broadening.

Without amplitude or phase modulation it is not possible to distinguish between the unknown spectral properties of the MSE multiplet (such as the Doppler shift) and the contribution to the interferogram phase from the birefringent waveplates in equation 2.34. Additional modulating optical components need to be included to the simple polarimeter setup in order to retrieve only the polarisation information. The most common modulation methods is the 'Temporally Switched Single Spatial Heterodyne'(TSSSH) which is the focus in this thesis. There are additional modulation techniques which have been explored [42, 47, 80] but will not be addressed in detail here.

Temporally Switched Single Spatial Heterodyne

This technique uses an additional switching half waveplate for phase modulation in order to measure weightings of the Stokes vector within successive interferograms. The setup for a TSSSH imaging polarimeter is shown in

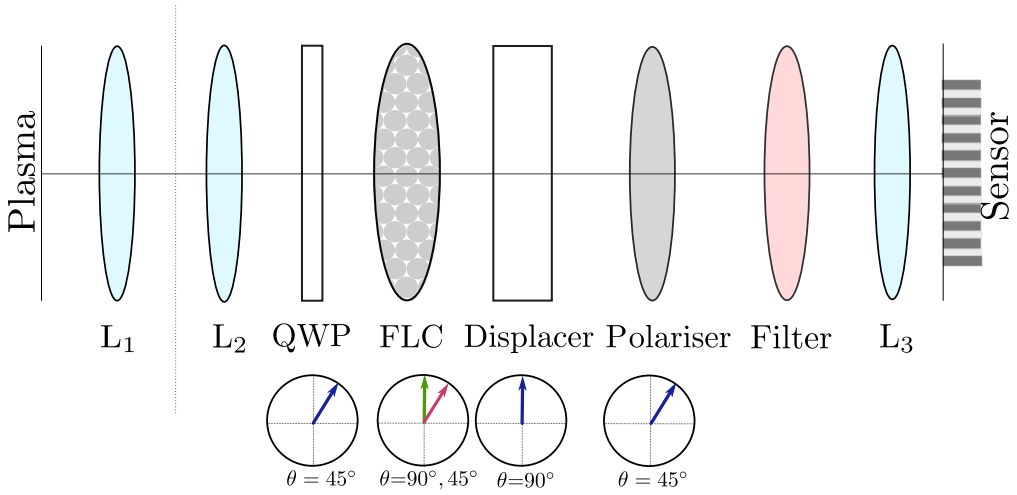

Figure 2.8: IMSE system using the temporally switched single spatial heterodyne encoding technique. The orientation of each component is shown in the arrow direction, where 0° is along the horizontal. The ferro-electric crystal switching half waveplate consisting of liquid crystal molecules switches its optical axis orientation by 45° when voltage is applied (green and red orientation arrows is ON and OFF state respectively.) Two successive weightings of the input Stokes vector is measured in two images. The phase difference between successive images retrieves the polarisation angle.

Fig. 2.8. The resulting phase difference between the two interferograms, assuming that the background plasma remains the same in the two images, retrieves the polarisation angle. The switching waveplate most commonly used is a ferro-electric crystal (FLC) device, which switches its fast axis orientation when voltage is applied by 45° on short timescales (≈100μs). The interferometer output in both states is then,

$$\begin{aligned} \boldsymbol{S}_+(\lambda) &= S_0 + S_1 \cos\left(\phi(\lambda, y)\right) + S_2 \sin\left(\phi(\lambda, y)\right) \\ \boldsymbol{S}_+ &= I_0 \left(1 - \zeta_l \cos\left(\phi(y) - 2\gamma\right)\right) \\ \boldsymbol{S}_-(\lambda) &= S_0 + S_1 \cos\left(\phi(\lambda, y)\right) - S_2 \sin\left(\phi(\lambda, y)\right) \\ \boldsymbol{S}_- &= I_0 \left(1 + \zeta_l \cos\left(\phi(y) + 2\gamma\right)\right) \end{aligned} \tag{2.37}$$

and a 2D spatially resolved image of the polarisation angle can be retrieved via phase demodulation.

The primary advantage to using the TSSSH system is that the system calibration is relatively straightforward, and simple phase encoding of the polarisation angle. Only a single displacer waveplate in addition to the switching waveplate is required, which improves the intrinsic contrast of the system. Using only a single spatial carrier the radial resolution can be maximised through orientation of the interference fringes. However, it has been shown that the reliability of measurements from the system depend on the uniformity of the FLC retardance[46]. FLC switching must be synchronized with both neutral beam modulation and camera exposure time, which can limit the maximum duty cycle. The measurement is also sensitive to any strong fluctuations between the two successive images, such as beam voltage fluctuations introducing a phase shift from variation in the Doppler shift of the MSE emission.

2.5 Summary

In this chapter we reviewed the effect of external electric and magnetic fields on hydrogenic atoms. For fast injected neutrals in tokamaks, movement across the magnetic field generates a Lorentz electric field in the rest frame of the neutrals, leading to polarised line emission from these Stark split states. We reviewed the relationship between the emission polarisation orientation and the magnetic field components and how this information can be used to infer the magnetic pitch angle in a plasma.

Using the Stokes-Mueller formalism we introduced two polarimetry techniques to measure polarised beam emission. The conventional MSE system encodes polarisation information into the harmonic amplitudes of two photoelastic modulators driven at a specific frequencies. Finally we introduced the polarisation interferometry based imaging MSE diagnostic. The IMSE technique imposes a spatially carrier upon the MSE multiplet to bring the orthogonal π and σ components in phase, producing a net polarised signal. Using a displacer waveplate with an arbitrary optical axis, a phase shift dependent on the incidence angle is applied such that the phase depends on spatial location, which is also mapped to a position on the sensor. Finally

we discussed the temporally switched single spatial heterodyne modulation techniques, using a single spatial carrier to encode polarisation information within the resulting interferogram.

Chapter 3

The Edge Current Density on MAST

In this chapter, analysis of motional Stark effect data from two plasma pulses from a previous experimental campaign on the MAST tokamak is presented. We describe the method used to analyse the diagnostic data, for which a demodulation routine was written by the author of this thesis, and was used by the author to analyse and interpret the results. The measurements are then compared to the plasma equilibrium reconstruction code EFIT++[68]. All plasma equilibrium reconstructions presented in this thesis chapter, and interpretation of, were performed by the author.

3.1 Edge Pedestal Stability

In the high confinement mode (H mode), a transport barrier forms[81] at the plasma edge, leading to enhanced plasma confinement and increased pressure and temperature. Within this edge "pedestal" region, with a width on the order of ≈2-3cm, the pressure gradient and current density increases until the onset of edge instabilities known as Edge Localised Modes (ELMs). ELMs cause the collapse of pedestal density and pressure gradients in a periodic manner, leading to spikes in D_α radiation leading to significant divertor heat fluxes. ELM suppression is of critical concern for next generation

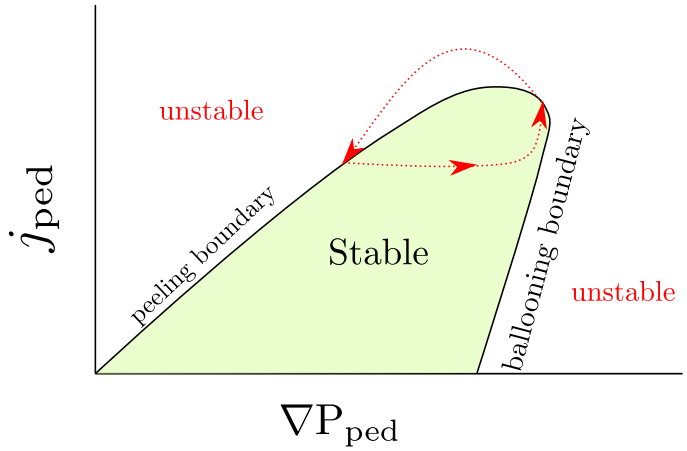

Figure 3.1: Diagram of the ELM stability as described by the peeling-ballooning model, reproduced from [82]. Pressure gradient increases in the pedestal drive local bootstrap current, until the peeling boundary is reached, until the mode becomes unstable and an ELM occurs. This then collapses the pressure and current profiles to within the stable (green) region.

tokamaks such as ITER, where the peak ELM energy fluence is predicted to reach between 10-30MJ/m^2 in Q = 10 operation[30]. Therefore, direct measurements of the current density from the MSE diagnostic could inform inter-ELM evolution dynamics, which are of paramount importance.

The leading candidate theory of ELM dynamics is the "peeling-ballooning" model[83]. A simplified diagram of the ELM crash cycle is shown in Fig. 3.1. Strong pedestal pressure gradients ∇p increase up to the ballooning limit. ∇p drives the local bootstrap current, increasing the local current density. This reduces the edge magnetic shear and improves stability to ballooning modes, moving towards the peeling limit, where a coupled peeling-ballooning mode is triggered and an ELM crash occurs.

In pedestal stability calculations analytical formula are used to calculate the current density[50, 51]. It was thought that the edge current density, being governed by resistivity and current diffusion, may evolve on a longer time scale than the edge pressure gradient, leading to a delay in the expected ELM crash. However recent modelling of the edge current in [84, 85] indicated that current diffusion does not fully explain why some pedestals are

found to be stable to peeling-ballooning modes for longer than is expected. Evidently for more informed stability analysis, direct measurements of both the pressure gradient and the edge current density could improve the confidence as to where the pedestal conditions are relative to the peeling-ballooning limits, and answer whether they evolve on on the same timescale.

This thesis chapter looks to analyse two plasma pulses from an experimental campaign on MAST, where the edge current was measured by the MSE diagnostic and results were previously presented for one discharge in[82]. Two methods can be used to determine the edge current density; either directly using the raw MSE data, or inferred using a plasma equilibrium solver. First we look to measure the current density directly using the MSE measurements, determining changes to the polarisation angle profile which indicate an increase in the local current density. Then we try to infer the current profile profile using the plasma equilibrium reconstruction code EFIT++[68]. EFIT++ represents the pressure and current profiles as a set of basis functions and attempts to iteratively solve the Grad-Shafranov equation whilst performing χ^2 minimisation of the fit to experimental data. We establish the routine code settings used to generate consistent equilibria with good convergence rates across the entire pulse, and also converges for other plasma pulses. Then we compare the current density evolution predicted by EFIT++ to the directly measured current density using the MSE data.

3.2 Local Measurement of the Edge Current Density

3.2.1 Overview of the plasma pulses

Whilst this chapter is mainly focussed on the measurement of the current density and whether this is achievable using the MSE diagnostic, rather than pedestal stability analysis, it is useful give some context to the plasma discharges analysed in this chapter. Plasma discharges 24408 and 24409 are double null divertor plasmas, with a plasma current of I_p=900kA. Fig. 3.2

shows the D_α emission throughout the two discharges, where frequent type-III ELMs occur between 0.24-0.33s, followed by a type-I ELM and then an ELM-free period. Using the peeling-ballooning cycle described in section 3.1, we can expect that the edge current density should increase before the type-I ELM, and then subsequently reduce after the ELM. The temporal resolution of the MSE system can be decreased to 0.5ms, but with a subsequent increase in the measurement uncertainty. For these discharges the data was averaged with 2ms time resolution. With at least 10ms before and after the ELM in both discharges, this should provide a good opportunity to analyse whether it is possible to measure changes in the current density and to what accuracy.

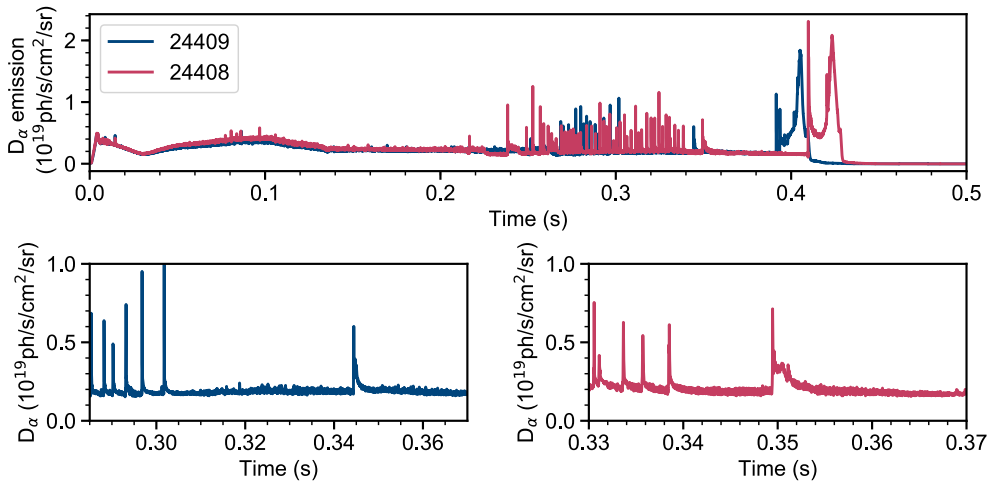

Figure 3.2: Top: D_α emission traces for MAST discharges 24408 (red) and 24409 (blue) Bottom: Zoom in at the end of the type-III ELM period, where a long ELM-free period before and after a type-I ELM is observed in both discharges, allowing for comparison of the current density measured by MSE in these discharges. Data retrieved from MAST database.

3.2.2 Demodulation of the MSE data

As described in section 2.4.1, the PEMs are driven at 20kHz and 23kHz to modulate the intensity of incoming polarised light at the driving and harmonic frequencies. The polarisation information is recovered using on the ratio of the second harmonic amplitudes of the two PEM frequencies, or using the ratio of the fourth harmonic amplitudes,

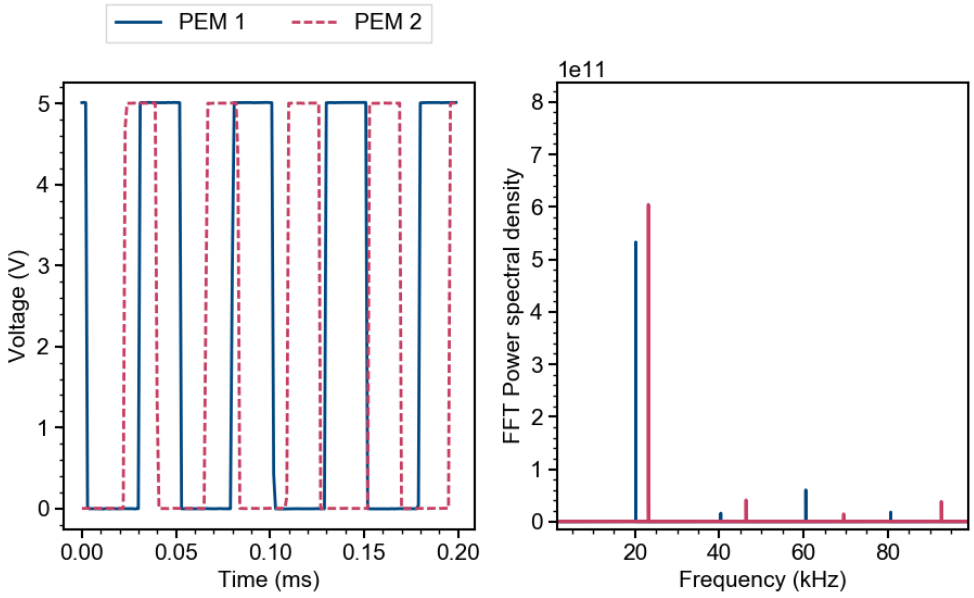

Figure 3.3: Left: 20kHz and 23kHz wave forms supplied to the PEMs. Right: Power spectral density of the PEM reference signals showing the 20kHz and 23kHz driving frequencies of PEM1 and PEM2 respectively, up to the fourth harmonic frequencies.

$$\gamma = \frac{1}{2}\arctan\left(\frac{J_2(A_2)I_{2\omega 1}}{J_2(A_1)I_{2\omega 2}}\right) = \frac{1}{2}\arctan\left(\frac{J_4(A_2)I_{4\omega 1}}{J_4(A_1)I_{4\omega 2}}\right) \tag{3.1}$$

The detected signal by the APDs is digitized by the ADCs producing a voltage signal. The polarisation angle is then retrieved using digital lock-in methods, briefly described in this section.

A phase difference arises due to a time lag between the MSE signal and the PEM reference signal. The optical head in the electronics of the PEMs is driven by an LC circuit within the transducer, and so the reference PEM waveform may not be precisely in phase with the measured MSE signal. This time lag can be up to one full wave period and so can lead to the reference waveform signal becoming out of phase by up to $\pm n\pi$ for the n^{th} harmonic MSE signal. Fig. 3.4 shows the correction of the phase for the harmonics of both PEMs, taking care to project the complex amplitudes into the correct quadrant to preserve the sign of the harmonic amplitudes. The root mean square (RMS) error in the harmonic amplitudes is then calculated from the standard deviation in the imaginary component of the complex amplitudes, and propagated through to the uncertainty in the Stokes vectors components.

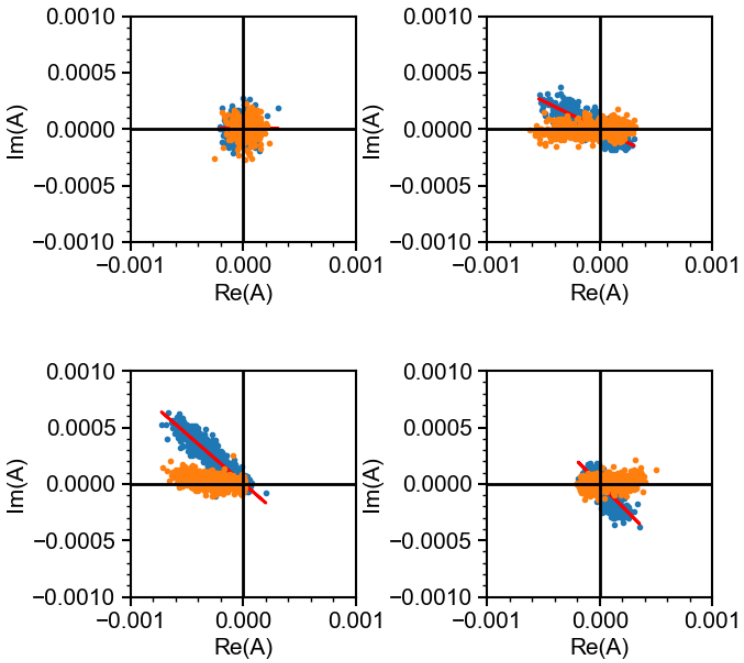

Figure 3.4: Correcting for the nuisance phase in the MSE signal due to a phase shift between the MSE signal and reference signal. Shown are the measured complex amplitudes on the argand diagram (blue). The first (top left) second (top right), third (bottom left) and fourth (bottom right) harmonics for the 20kHz PEM. Linear regression best fit is used to find to the phase and quadrature, then is removed from the complex amplitude (orange).

Once the harmonic amplitude intensities are recovered, these can be used to calculate the PEM retardances and the value of the Bessel functions at this retardance. Fig. 3.6 shows the Bessel amplitudes as a function of PEM retardance. The PEM retardances are set by the PEM controllers, usually at half wave retardance, where it is clear the second order Bessel function is maximised, which therefore maximises the second harmonic amplitude of the PEMs. To remove the inter-modulation frequency at 43kHz, shifting to higher retardances of 220° reduces the first harmonic amplitude, and maximises the bandwidth between the second harmonic amplitudes of the PEMs to 3kHz.

Using equations 2.25 the initial Stokes vector is finally reconstructed, used to calculate the linearly polarised fraction (LPF) and circularly polarised fraction (CPF). Whilst we are primarily interested in retrieving the polarisation

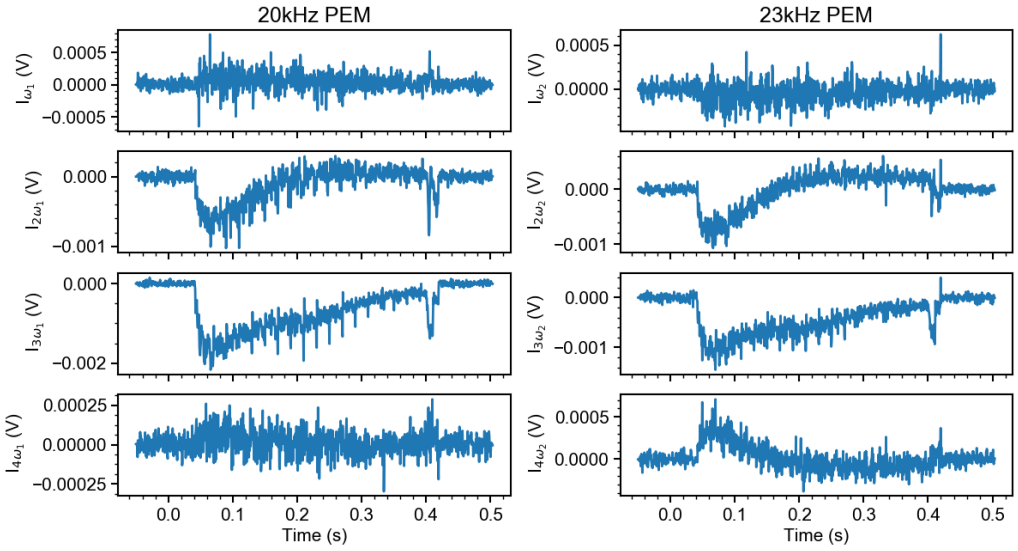

Figure 3.5: Recovered intensities of the harmonics for the 20kHz and 23kHz PEM. Note that in this case the intensity of the fourth harmonic is particularly noisy, and so it is unlikely the polarisation angle could be recovered using the ratio of $I_{4\omega_1}/I_{4\omega_2}$.

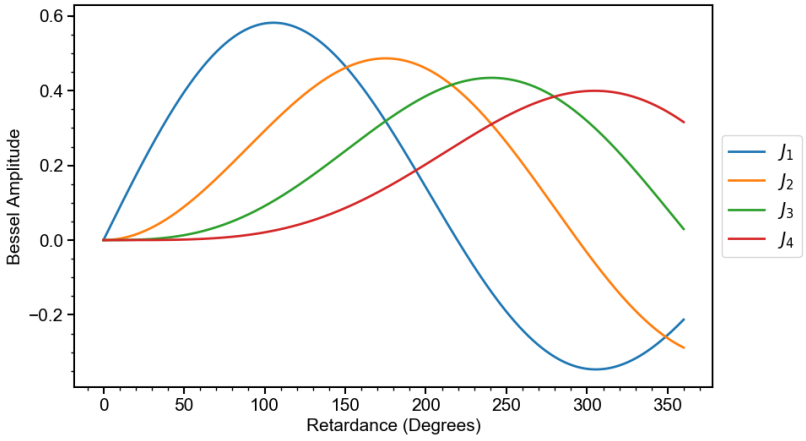

Figure 3.6: Amplitude of the Bessel functions with varying PEM retardance. A crossing point occurs where J_2 is maximised at 180°, however the PEMs are run at a higher retardance of 220° on MAST to suppress the J_1 amplitude and increase the inter-modulation bandwidth of the second harmonic, at a minor cost to the J_2 amplitude.

angle, monitoring the circularly polarised fraction measured by each channel could identify whether contaminating impurity line emission is present within the bandpass of the filter. Circularly polarised light could also alter the linear polarisation angle if mirrors are present in the optical system (not of concern to the MAST system as the PEMs are mounted directly to

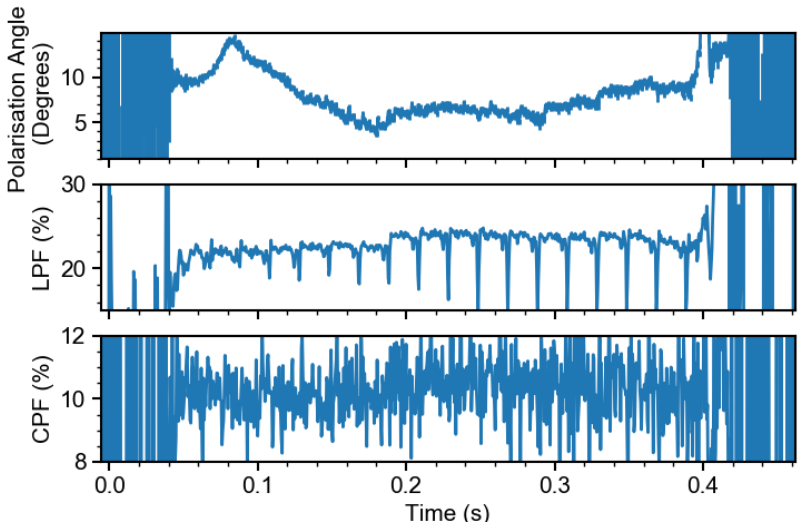

Figure 3.7: Measured polarisation angle for MSE channel 16 at R = 1.0m

the port window), or if stress induced birefringence is significant within the diagnostic port window.

Finally, this demodulation process is completed for each radial channel. Fig. 3.7 shows the temporal evolution of the polarisation angle, linearly polarised fraction and circularly polarised fraction for channel 16 at R = 1.0m. The CPF remains constant at $\approx 10\%$ throughout the discharge, but periodic decreases in the LPF is observed. This can be attributed to an event which causes a significant increase in the D_α emission, such as ELMs, from the plasma which can temporarily swamp the polarised beam emission.

3.2.3 Influence of the radial electric field

It has been well documented that the radial electric field E_r influences the polarisation angle measured by MSE diagnostics[36, 86]. E_r arises as a consequence of the force balance, balancing the pressure gradient and $v \times B$ where v is the plasma velocity and B the magnetic field within the plasma. The influence of the radial electric field is significant in regions of the plasma where there are large pressure gradients, which occur in the pedestal, and for highly rotational plasmas [87, 88]. From Eq. 2.9, we see that the radial electric field shifts the Lorentz electric field vector depending on the angle between the line of sight and the toroidal direction. The influence of E_r can

be minimised by choosing the MSE geometry such that the sightlines are radial to the toroidal field, however this would limit radial resolution of the system due to the finite width of the neutral beam. Generally E_r is corrected for through the addition of terms in the A coefficients from Eq. 2.13, if a measurement of E_r is routinely available. Direct measurement of E_r is challenging, but in fact sensitivity of the polarisation angle to the radial electric field has led to some direct measurements of E_r through using multiple MSE systems[86]. The radial electric field is given by,

$$E_r = \frac{\nabla P_i}{Z_i n_i e} - v_\phi \times B_z + v_z \times B_\phi \tag{3.2}$$

where v_ϕ and v_z are the toroidal and vertical plasma velocity, B_ϕ and B_z the toroidal and vertical magnetic field components, ∇P_e the pressure gradient, Z_i the ion charge number, n_i the density of the ion species, and e the elementary charge.

Measurements of the poloidal ion velocity using the poloidal CXRS views was not always available on MAST, and unfortunately were not available for these two discharges. Other work [89] noted that the toroidal plasma velocity contributing from the momentum transfer from the neutral beams, was significantly larger ($v_\phi \approx$ 200km/s) than the poloidal velocity, mostly due to the pressure gradient ($v_\theta \approx$5km/s towards the core plasma, but towards the plasma edge $v_\phi/v_\theta \approx 2$.) When measurements are available, analysis should look to include this term in the E_r correction process. The toroidal velocity v_ϕ is measured by the charge exchange (CXRS) diagnostic [90], using the velocity of the main ion impurity species C^{6+}. Fig. 3.8 shows the toroidal velocity profile measured by CXRS for the discharge 24408 at t=0.33s in the time leading up to an ELM. The data at the edge of the profile is noisy, particularly for the channels located just beyond the plasma boundary. To ensure that the resulting E_r profile is smooth, a rolling average was performed on the data, with a spatial window of 2.5cm, which is around the spatial resolution of the MSE diagnostic.

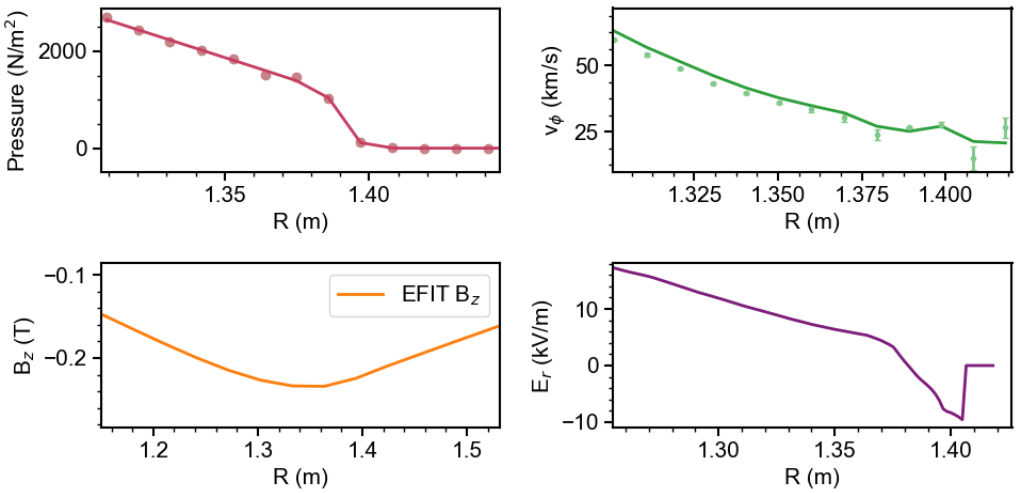

Figure 3.8: Top left: Fit of the modified tanh function to the pedestal region of the pressure profile. The pressure profile is derived from the TS electron temperature and density measurements. The mtanh fitting function was provided by James Clark (TS responsible officer). Top right: Smoothing of the toroidal ion velocity profile measured by CXRS. Outside the separatrix E_r has been fixed to zero.

The assumption $T_i \approx T_e$ was made[1], such that measurements of the electron density and temperature from the high resolution Thomson scattering (TS) system could be used to derive the pressure gradient [1]. The electron density and temperature edge profiles were fitted using a modified tanh function, which is a common approach to fitting the strong gradients in the measured TS data on many tokamaks[91, 92]. These profile fits are not necessarily the most optimised for this application, but are sufficient to provide a reasonable estimate of the magnitude of Er within the pedestal region. Other work is ongoing to produce routine fitting algorithms for the TS data for MAST-U.

The final E_r profile is shown in Fig. 3.9. The evolution of E_r throughout the ELM period shows that E_r of order 10kV/m can be anticipated in these H mode discharges during the ELM-free period. Comparing to the strength of the Lorentz field which, depending on the beam voltage is around $E_L \approx 10^6$V/m, then $E_L/E_r \approx 100$. Therefore we can expect that the contribution to the polarisation angle due to E_r is small, but not negligible as E_r is

[1]We also assume that Z_{eff}=1 such that n_i=n_e, strictly we should consider the density contribution from impurities however this is a small correction to n_i.

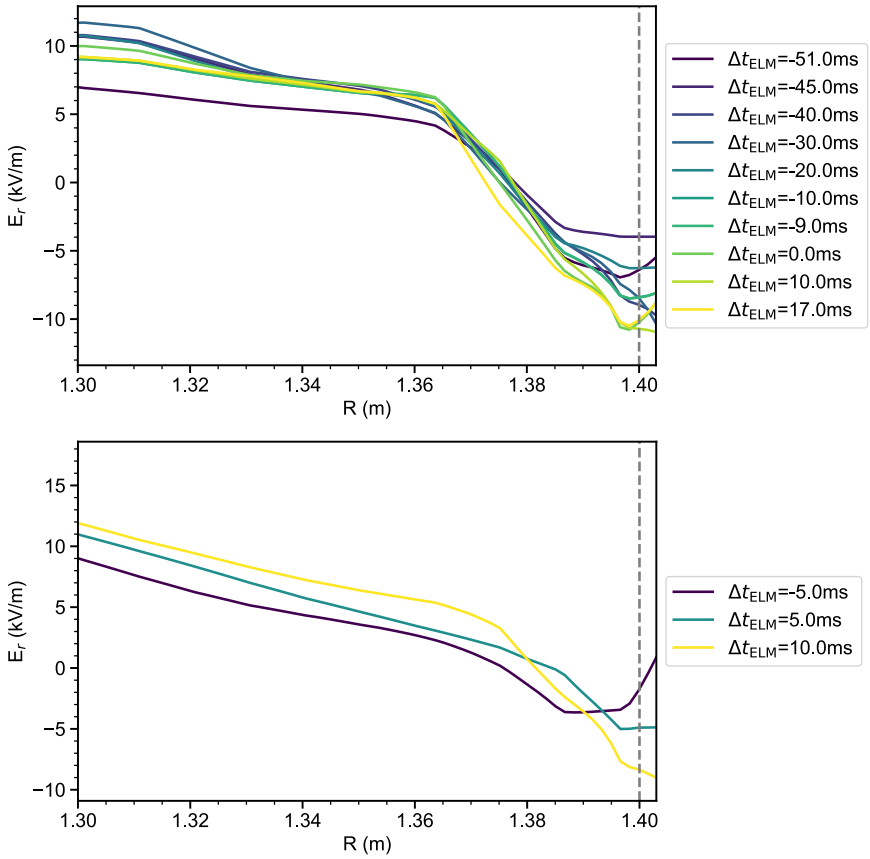

Figure 3.9: Evolution of the derived radial electric field for discharges 24408 (left) and 24409 (right). The E_r 'well' increases to a maximum of -10kV/m just before the ELM and therefore it is important to correct for E_r for the edge MSE channels.

orthogonal to the Lorentz field. Using Eq. 2.12 and knowledge of the view geometry via the A coefficients in Eq. 2.13, the sensitivity of the polarisation angle $\mathrm{d}\gamma/\mathrm{dE}_r$ can be derived as[41],

$$\frac{d\gamma}{dE_r} = -\frac{\cos\gamma^2}{vB_\phi}\frac{\cos\left(\alpha+\beta\right)}{\sin\alpha}, \tag{3.3}$$

where γ is the measured polarisation angle, α the angle between the toroidal direction and beam axis, β the angle between the MSE view and beam axis, v is the velocity of the neutral beam and B_ϕ the toroidal magnetic field. Fig. 3.10 shows the sensitivity of the MSE channels to E_r. On MAST, due to the low magnetic field and favourable tangential viewing geometry, the polarisation angle correction is small ($\mathrm{d}\gamma < 0.2°$) at a peak $\mathrm{E}_r \approx -10\mathrm{kV/m}$ in the pedestal region. Any shift in the polarisation angle over the pedestal region larger than this correction can be attributed to actual changes in B_z, rather than a contribution from E_r effects. Although here we focus on sensitivity of the MSE channels to E_r in the pedestal region, it should be noted that E_r vanishes at the magnetic axis location, despite significant toroidal rotation, as the poloidal field B_θ goes to zero. This is shown in Fig. 3.10 where the sensitivity to $E_r \approx 0$ for channels at the magnetic axis location ($\mathrm{R} \approx 1.0\mathrm{m}$).

3.2.4 Calculation of the local toroidal current density

The MSE diagnostic is sensitive to changes in the poloidal magnetic field and hence the field line pitch. From Eq. 2.14 the poloidal magnetic field component can be derived from the measured polarisation angle,

$$\tan(\gamma) = \frac{-\cos(\beta)B_z - \frac{Er}{v}\cos(\alpha+\beta)}{\sin(\alpha)B_\phi} \tag{3.4}$$

where α is the angle between the toroidal direction and the neutral beam direction, β is the angle between the line of sight and the neutral beam. These geometric angles are described by the A coefficients in Eq. 2.13, which are determined by the diagnostic geometry. E_r is the radial electric field, v is the beam velocity, and B_z and B_ϕ are the vertical and toroidal components of the magnetic field respectively. An approximate value of the toroidal field

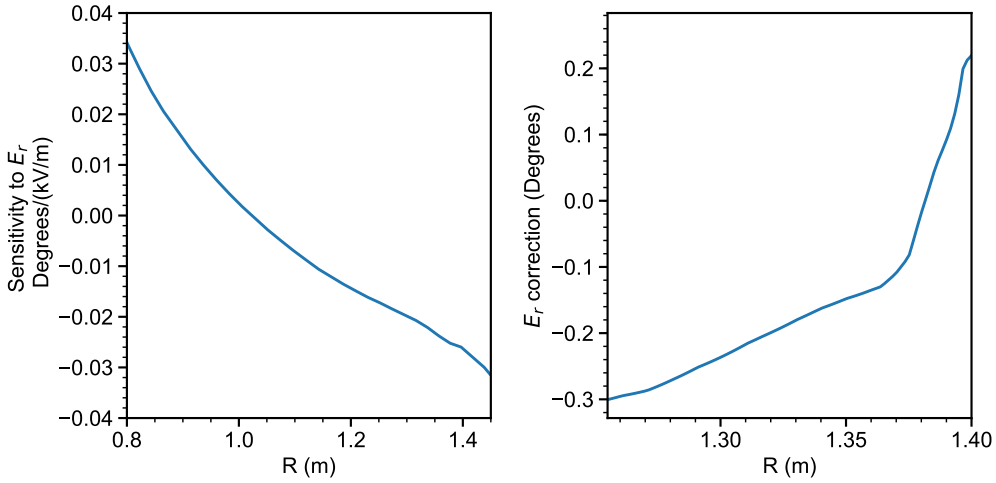

Figure 3.10: Left: $d\gamma/dE_r$ for the MAST MSE view geometry, a toroidal field $B_\phi \approx -0.22$T, and a beam voltage of 66.7kV. Right: Polarisation angle offset required to account for the E_r profile in Fig. 3.9 at t=0.355s, with a maximum value of E_r in the pedestal of -10kV/m.

at the plasma edge is retrieved from a magnetics only equilibrium, as at the plasma boundary $B_\phi \approx B_{\text{vac}}$ the vacuum toroidal field generated only by the currents in the field coils around the vessel. Using Ampere's law the toroidal current density is,

$$\mu_0 j_\phi = \frac{\partial B_z}{\partial R} - \frac{\partial B_R}{\partial Z} \tag{3.5}$$

where B_R is the radial magnetic field, μ_0 is the vacuum permittivity and B_z is the poloidal field at the midplane (z=0). From Eq. 3.5 the toroidal current density is then proportional to the spatial gradient of the measured polarisation angle profile. The final unknown is the term $\frac{\partial B_R}{\partial Z}$, however the B_R component is small at the midplane (Z=0), which is the location of the MSE fiber sightlines. This term can also be approximated from a basic equilibrium reconstruction constrained only with magnetic measurements.

3.2.5 Evolution of the edge current density

Using the methods outlined in the previous section, we can analyse the evolution of the polarisation angle and current density profiles during the ELM

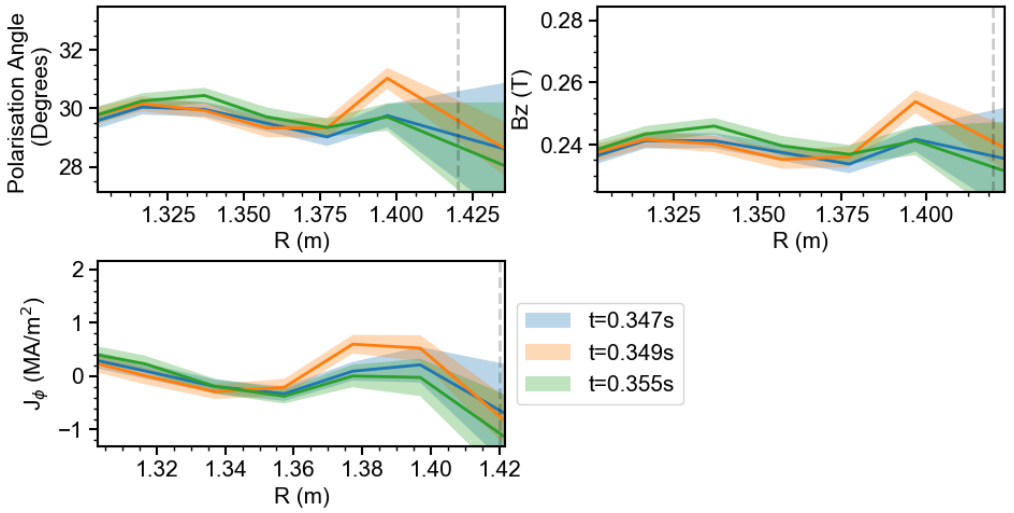

Figure 3.11: Evolution of the polarisation angle profile (top left), inferred B_z (top right) and current density profiles (bottom left), 3ms before (blue), 1ms before (orange) and 2ms after (green) the type-I ELM.

cycle. We choose three time intervals: before the ELM (t=0.347s), immediately after (t=0.349s), and ≈5ms after the ELM (t=0.355s) during the ELM-free period. In Fig. 3.11 the polarisation angle measured at these time intervals is shown, as well as a 2σ confidence interval. The profile clearly indicates an increase in the polarisation angle localised within the pedestal region just before the ELM, and relaxes 5 ms after the ELM. Propagating to the toroidal current density using the method outlined in section 3.2.4, this peak across a single channel in the polarisation angle profile is smeared out across the ≈3cm pedestal region, which can be seen in the steep pressure gradient at the plasma edge in Fig. 3.8, leading to a broad current peak in the pedestal. These local current density profiles can now be compared to the inferred current density profile using the equilibrium reconstruction code EFIT++.

3.3 Equilibrium Reconstruction

Plasma equilibrium reconstruction codes solve the Grad-Shafranov equation (Eq.1.9) to determine the poloidal flux function ψ and toroidal current distribution, whilst also fitting to a set of diagnostic measurements. Using an

initial value for $\psi = \psi_0$, $p'(\psi)$ and $ff'(\psi)$ functions are calculated. A fit to the set of diagnostic measurements is performed, minimising χ^2 by adjusting $ff'(\psi)$ and $p'(\psi)$,

$$\chi^2 = \sum_i \left(\frac{D_i - Ci}{\sigma_i} \right)^2 \tag{3.6}$$

where D_i is the measured data and C_i is the computed (or expected) value and σ_i is the uncertainty in the measured data, summed over i data points. Then, using the updated functions $p'(\psi)$, $ff'(\psi)$, a new poloidal flux function is found by solving the GS equation. This is an iterative process, using the Picard iteration scheme[53], until the difference in ψ between iterations reaches a prescribed tolerance (generally between $\delta\psi \approx 10^{-8} - 10^{-4}$) and the code has converged. After convergence is achieved, equilibrium parameters such as the poloidal flux function, current flux function $f(\psi)$, pressure $p(\psi)$ are obtained, as well as the plasma boundary and parameters such as the normalised plasma β, inductance ℓ_i and the total stored energy W. The main benefit of this type of equilibrium reconstruction is it is extremely computationally cheap to run and can be performed intershot.

However, providing a good fit to the diagnostic measurements and retrieving accurate current and pressure profiles can be challenging. There are many regions across the poloidal cross section where virtually no measurements of either the pressure or current are made, either directly or indirectly, using plasma diagnostics. This leads to a wide distribution of possible ψ, p' and ff' configurations which would equally satisfy the GS equation and minimise χ^2 for the available measurements. Whether the resulting equilibrium is a good representation of the internal plasma profiles, magnetic field, flux surface geometry then depends strongly on the quality (and quantity) of the measurements and the basis functions used to represent p' and ff'.

The equilibrium code EFIT++[68] is used for MAST[2], which is derived from the original EFIT code written for the DIII-D tokamak[53]. As equilibrium reconstruction codes require input data from a variety of diagnostics, data structure handling was improved, the code became fully machine independent. Development is continuing on EFIT++ to; Redevelop data handling

[2]and for future MAST-U plasmas.

codes using python, include EFIT++ as a module in integrating modelling suites such as OMFIT[93] and finally generate robust kinetic equilibrium reconstructions to inform disruption prediction on MAST-U[94].

3.3.1 Constraints

A variety of diagnostic measurements are used as inputs to EFIT++ to produce varying levels of constrained equilibrium. Ideally one would develop an equilibrium reconstruction routine with measurements from all available diagnostics, but not all diagnostic measurements are available for every plasma discharge. For example, if NBI heating is unavailable, so too are measurements from the MSE diagnostic. Other complications can arise, such as inconsistencies between different diagnostics measuring the same parameter[95], which can lead to the equilibrium not converging or fitting poorly to the diagnostic data. Developing routine numerical settings and constraints that produce equilibria with plausible internal plasma profiles with acceptable fits to the data for all plasma scenarios is non-trivial. The process to develop equilibrium settings, such as the basis function representation or the weighting for each diagnostic measurement, requires additional bespoke analysis for each diagnostic, particularly for more elaborate plasma configurations such as double null divertor (DND) plasmas with significant beam heating. Finally this variety of constrained equilibria have different purposes. The "magnetics only" equilibrium, with constraints explained in detail below, means intershot analysis is available within the control room and is used to inform basic flux surface geometry and as a flux map for diagnostics [96].

Each of the diagnostics used to constrain MAST equilibria is shown on a poloidal cross section of the MAST vessel in Fig. 3.12. The most basic constraint level at MAST includes only magnetic measurements (magnetics only EFIT). These include: 16 flux loops for loop voltage measurements, 40 magnetic pick up coils, along the center column for measurements of B_z, 38 outboard magnetic pickup coils, measuring both B_r and B_z, and Rogowski coils to measure the plasma current and currents in passive structures around the vessels[97]. Over the course of the MAST campaigns, the num-

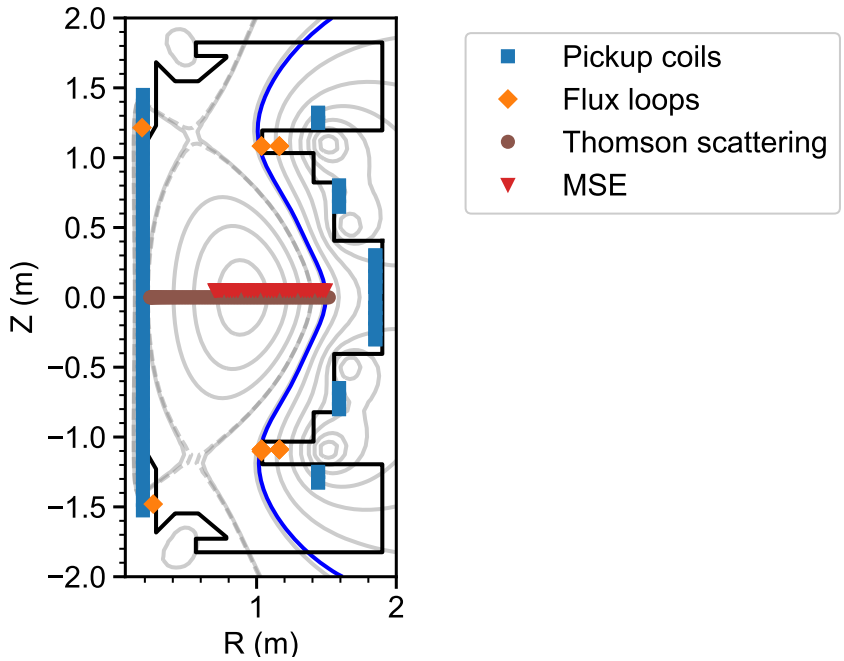

Figure 3.12: Poloidal cross section of the MAST vessel, including the vessel walls (black) and the poloidal flux of MAST plasma 24409, t=0.267s (gray). The magnetic pick up coils (blue squares) and flux loops (orange diamonds) are placed on both the center column and outboard side of the machine. The Thomson scattering (brown) diagnostic measures the electron density and temperature across the entire poloidal cross section and constrains p'. The MSE diagnostic measures across from the core to the plasma edge (red). Both TS and MSE measure at the midplane (Z=0), but in the diagram the MSE channel vertical locations have been shifted to Z=0.05m for clarity.

ber of available pickup coils on the outboard mid plane reduced due to coils breaking. To further constrain the plasma boundary, the linear D_α camera is included as a constraint. The diagnostic consists of an array of photodiodes which capture image of D_α emission across the plasma at high time resolution (1ms). The D_α emissivity peaks within 1-2cm of the plasma boundary location and therefore constrains the radial location of the last closed flux surface (LCFS)[98, 99].

A further level of constraint includes measurements from the Thomson scattering (TS) system [92]. The electron density n_e and temperature T_e is measured by the TS system at high resolution with 120 spatial locations with 10mm radial resolution and the electron pressure derived from fits to n_e

and T_e. In the simplified approach, it is assumed the $T_i = T_e$ and the total plasma pressure becomes $P = 2P_e$. In high performance discharges, particularly towards the core (or central region) of the plasma, the fast ion pressure may need to be included. However, there is no direct measurement available. To compensate for this lack of information on the fast ion pressure, measurements at the edge of the pressure profile are used for constraint ($\psi_n > 0.7$) and the core plasma is left unconstrained. Equilibrium using magnetics and the pressure constraint will be known as "kinetic" equilibrium.

The final constraints to include are measurements from the MSE diagnostic, which is sensitive to the orientation of the poloidal magnetic field. A 1D radial profile of local polarisation angle measurements are provided to inform B_z. MSE measurements are the only available internal constraint for ff' on MAST. Other tokamaks, such as on JET, additionally use the far-infrared interferometer-polarimetry diagnostic for line integrated plasma density, poloidal magnetic field and magnetic axis location [100]. Including the MSE constraint is important to accurately reconstruct structure in the current profile (and subsequent q profile), particularly in strongly heated plasmas and early ramp phase of a plasma discharge where the q profile can exhibit reverse shear[3].

3.3.2 Spline and polynomial representation of the basis functions

It is useful to understand how the basis functions can be represented in equilibrium reconstruction, and the impact this choice has on the resulting pressure and current profiles. The functions ff' and p' can be represented by a polynomial expansion,

[3]q profiles are said to be reverse sheared when $q_0 > q_{\min}$ and $q_{\min}$ is located off-axis. Reverse shear q profiles have been shown to improve plasma stability against various MHD modes[101, 102] and has been developed into the "advanced tokamak" steady state scenario[103] used on many tokamaks today.

$$\begin{aligned} p'(\psi) &= \sum_{k=0}^{n} a_k x^k \\ ff'(\psi) &= \sum_{k=0}^{n} b_k x^k \end{aligned} \tag{3.7}$$

where n is the polynomial order, and a_k, b_k the polynomial coefficients. The basis functions are defined over the normalised poloidal flux, ($\psi_n = 0$ at the boundary and $\psi_n = 1$ at the LCFS). Additionally a tension spline representation is available[104], defined by a set of k knot points. Constraint can be imposed on the gradient of the fitted splines through the knot points, set through the relational weights of the splines. Spline tension can also be used as a constraint, which defines the way the interpolating function behaves between the knot points. If the tension is too high, one can expect straight line interpolation style fits between adjacent knots, and zero tension would provide a more 'polynomial' like fit. Further details of the mathematical description of these basis functions can be found in [105] but will not be further addressed here. Polynomials allow for smooth fitting to profiles, but do not allow as much freedom to the fit to sharp gradients in the pressure and current profiles.

3.3.3 Choice of basis function

The most appropriate choice of basis function representation depends on the structure within the underlying pressure and current profiles. Since magnetics only equilibrium provides no internal constraint on p' or ff', low order polynomials are chosen to give reliable convergence across all types of plasma discharge and smooth internal profiles, in which the details are likely incorrect (eg. elevated $q_0 > 1$ during sawtoothing) but sufficient for intershot analysis and diagnostic mapping to flux co-ordinates. For plasmas during H mode, with steep pedestal pressures, or strongly heated plasmas, features in the TS data or MSE measurements can be more difficult to represent with a basic polynomial. The basis functions must be chosen to accurately fit the TS data, which constrains p', and MSE data, constraining the plasma current, to retrieve the most accurate pressure and current profiles that describe

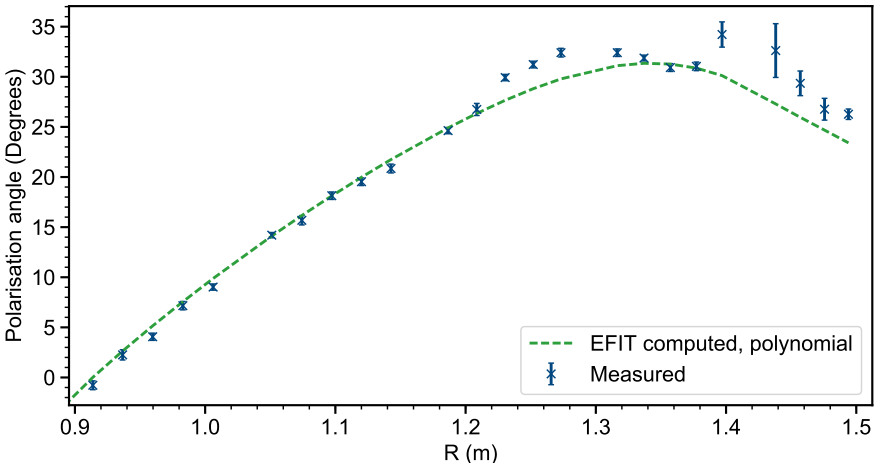

Figure 3.13: The polarisation angle profile at the plasma edge measured by the MSE diagnostic for pulse 24409, t=0.367s. Fits to the data computed by EFIT are shown, using the 3rd and 4th order polynomial basis representation for ff' and p' (green dashed). The polynomial basis functions provide a poor fit to MSE channels towards the outboard edge.

the plasma.

The method for developing the equilibrium settings used for the rest of the equilibrium analysis in this chapter is now presented. Firstly EFIT++ was ran for discharge 24409, for a single timeslice t=0.367s, using low order polynomial basis functions, 3^{rd} order for p' and 4^{th} order for ff' respectively. This is the standard approach on other tokamaks[53], as the reconstructions tend to be more numerically stable and provide reasonable fits to the diagnostic data. Fig. 3.13 shows the measured and computed profiles for the pressure and polarisation angle profiles. In this case polynomials provide a reasonable fit to the core MSE channels where there is little structure, but fails to fit the edge channels. Similarly for the steep pressure gradient developed in H mode, the polynomial basis function does not provide enough degrees of freedom in the fit in order to represent the pressure gradient in the pedestal. The fit to the data was not improved (ie. χ^2_{min} was not reduced) by increasing the polynomial order, and beyond 6^{th} order polynomials the code did not converge.

Fig. 3.14 shows the computed polarisation angle profile using tension splines.

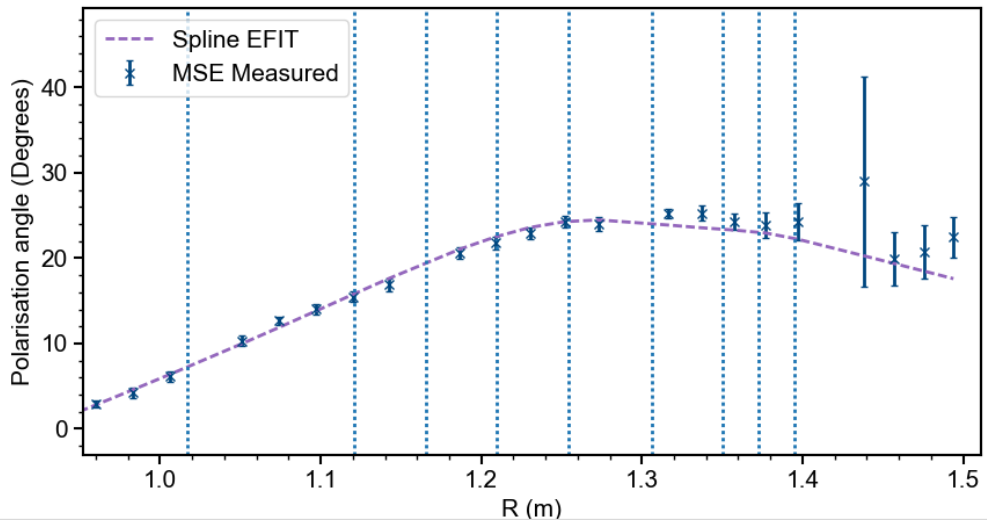

Figure 3.14: Fit to the MSE profile (purple, dashed) using spline knot representation for both the ff' and p' basis functions. The knot point locations (dotted, light blue) are spaced closely towards the boundary location

Initially 10 knots for ff' and 5 knots for p' were chosen, equally spaced from $\psi_n = 0$ to $\psi_n = 0.7$ in the core reason, and 2-3 knots close together between $\psi_n = 0.9$ and $\psi_n = 1$. Any further increases in the number of knot points meant that the equilibrium did not converge. The spline fit allows for more flexibility in achieving an improved fit to the pedestal gradient.

The level of flexibility (or curvature of the fitted profile through the knot points) is determined by the relational weight of the splines. Without enough regularisation, the fitted profiles can exhibit oscillations, but too high a tension can lead to stiff computed profiles with large χ^2 values. A scan of the relational weights was performed and the χ^2 value calculated for the fit to the MSE data, and a regularisation weight for both ff' and p' of 0.001 was found to produce more acceptable χ^2 values. An example of this is shown in Fig. 3.15 and Fig. 3.16, where the tension of ff' and p' was varied and compared with the best fits to the MSE and pressure data. We see that lower tension provides better χ^2_{min} values for both sets of data, as the loose tension provides more freedom to fit structure at the edge of the polarisation angle profile, and in the edge of the pressure profile.

Finally, the knot point locations for p' are chosen at the steep gradient regions of the pressure profile, with an additional knot point around the plasma axis

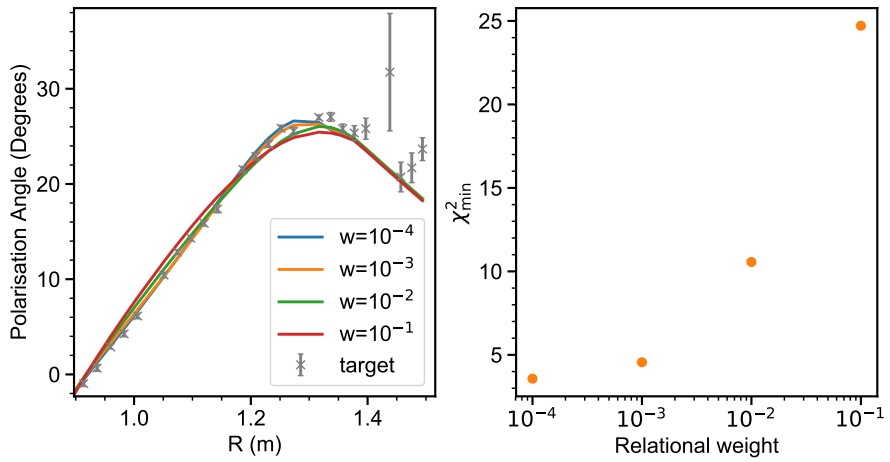

Figure 3.15: Scan of the relational ff' and p' weight. The outer 4 channels were not included in the fit as these channels resided outside the plasma.

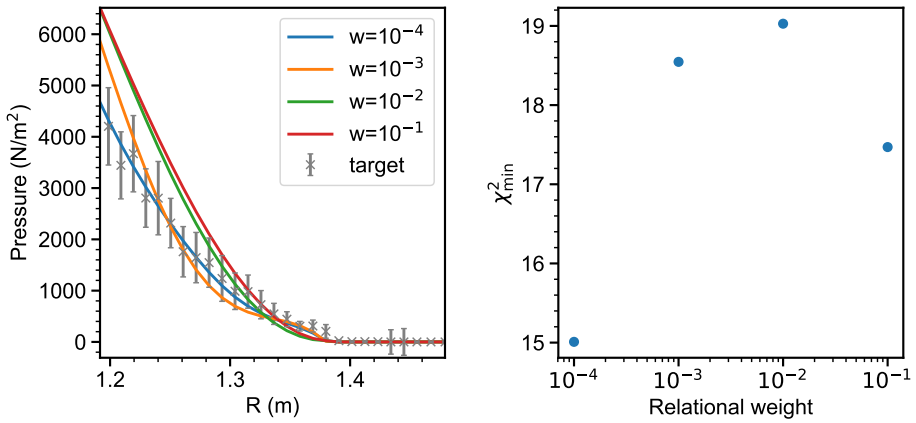

Figure 3.16: Scan of the relational ff' and p' weight. Higher relational weight produces a 'stiff' fit to the edge channels.

to avoid the possibility of a collapsed hollow pressure profile. This provides an improved fit to the pedestal gradients, important for accurately reconstructing the edge current density and leads to an over estimate of the computed core pressure to crudely "include" the fast ion pressure contribution. An extension of this equilibrium analysis would be to run a beam model to estimate the fast ion distribution function, to then calculate the fast ion pressure and include this into the pressure profile. Then the equilibrium can be re-run to test for changes in the current profile due to fast ion pressure.

3.3.4 Fit to the diagnostic profiles

Using equilibrium settings developed in section 3.3.3, EFIT++ was run for the discharge 24409 for many timeslices throughout the discharge. The equilibrium timeslices showed good convergence rates across the entire discharge.

Fig. 3.17 shows the EFIT predicted polarisation angle compared to the measured polarisation angle, for discharge 24409, t=0.367s. The overall fit to the profile across the core is good, however EFIT under predicts the measured polarisation in the plasma edge. This is likely because of an inconsistency between the MSE, TS and D_α boundary measurements in the pedestal region. The number of outer magnetic probes were limited in the later MAST campaigns due to breakages, and so the D_α emission peak was used instead to locate the boundary position. There was difficulty in fitting both the pressure profile near the separatrix and the boundary location as measured by the D_α camera. This could be resolved by shifting the D_α boundary offset by R≈0.5cm. The inconsistency was later found to be due to a shift in the radial location of the TS system measurements of ≈0.5cm. When rerunning the equilibrium with the new calibration the equilibrium computed boundary location was now within the uncertainty on the boundary location measured by the D_α camera. This shows that the uncertainty in the spatial locations of the diagnostic data should also be considered when constraining the equilibrium reconstruction.

3.3.5 Resulting current density profile

The resulting current profiles with new calibration of the TS radial locations, offset to the D_α boundary location and equilibrium settings are shown in Fig. 3.19. The consequence of these changes was that the edge current peak which was previously $j_\phi = 1.2\text{MA/m}^2$ was reduced to $j_\phi = 0.8\text{MA/m}^2$. Between these two equilibria the computed fit to the MSE data by EFIT remained virtually identical, showing that either are potentially valid solutions and provide good fits in the pedestal. This indicates that the equilibrium requires further constraint in order to narrow down the solution space being searched by the equilibrium solver. Additionally, including improved estim-

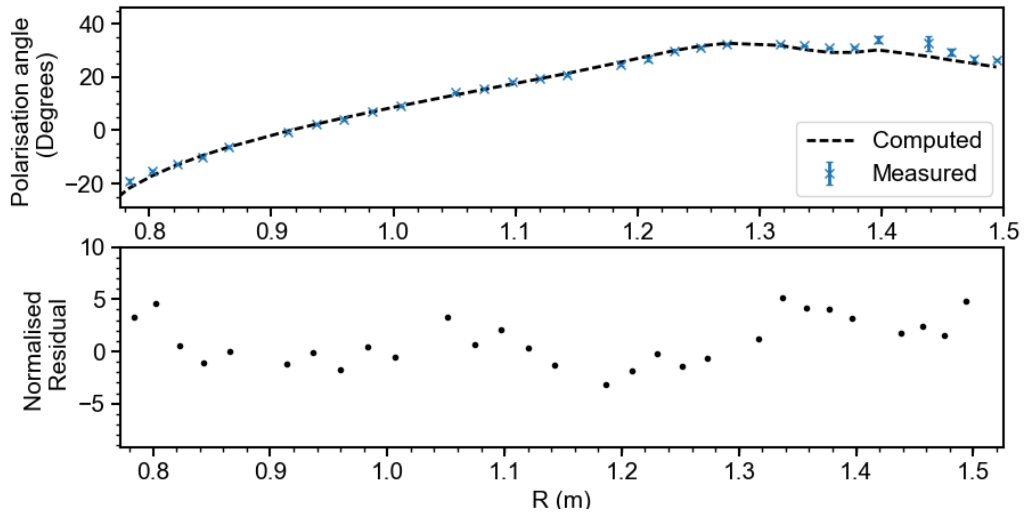

Figure 3.17: Fit (black, dashed) to the polarisation angle (blue) measured by the MSE diagnostic.

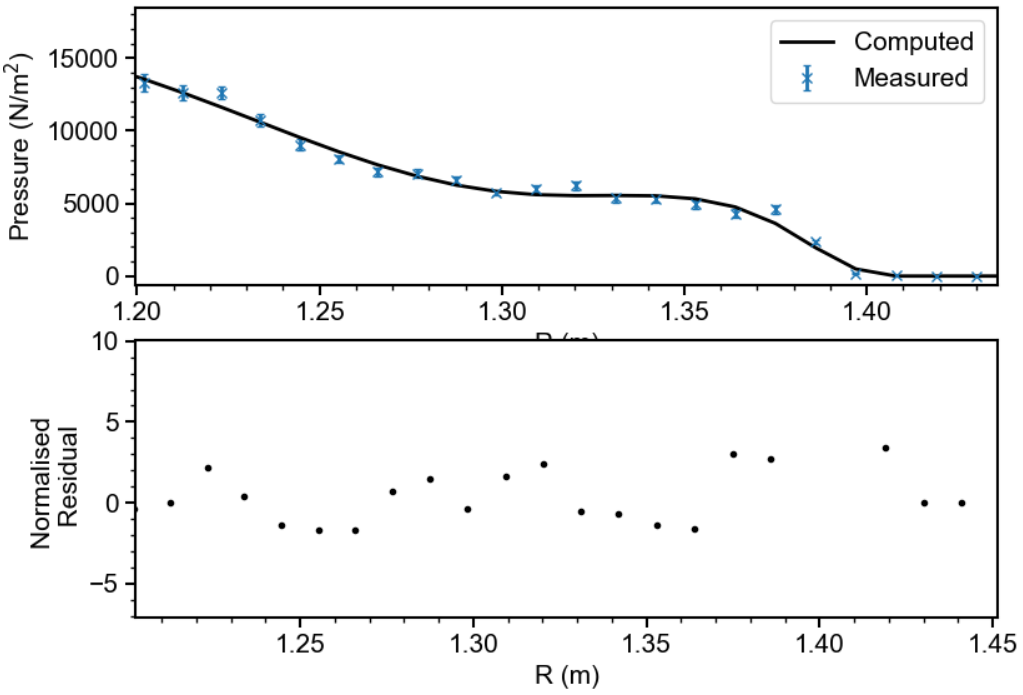

Figure 3.18: Fit (black) to the pressure profile (blue) in the edge pedestal region.

ates of the uncertainty in the spatial locations of the diagnostic data could improve the quality of the equilibrium profiles.

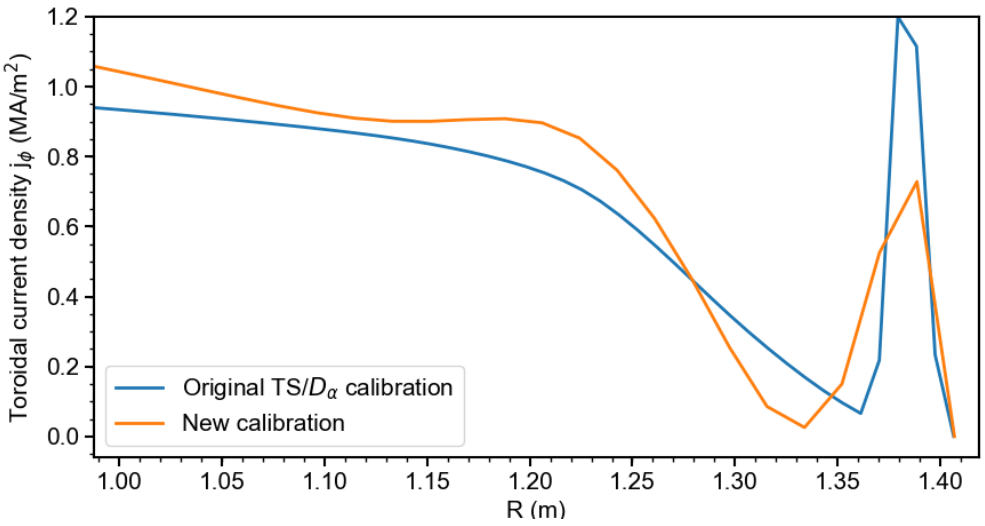

Figure 3.19: Change in the resulting current density profile using the new calibrated data and equilibrium run settings outlined in 3.3.3.

3.3.6 Comparison to local current density measurements

In section 3.2.5 the evolution of the local current density profile was calculated from the MSE data in discharge 24408. Using the equilibrium setup from section 3.3.3 the equilibrium was run for the timeslices stated during the ELM cycle. Fig. 3.20 shows the MSE derived current density measurements compared to the EFIT++ inferred current profile. There is good agreement in the location of the current density peak. However the MSE measurements indicate a large current density peak just prior to the ELM, which is not replicated by the equilibrium current profile. Due to the addition of other diagnostic data in the pedestal region, this predicted current profile likely provides the best χ^2 minimisation to all diagnostic data. It is also clear that the spatial resolution of the MSE system is too coarse to directly derive the edge current density, without a large uncertainty in the current density peak in the pedestal. However, we have also shown that the current density peak inferred from the equilibrium can be influenced greatly depending on the quality of the input data and equilibrium settings. If equilibrium current profiles are to be used to inform stability analysis, this uncertainty must be considered.

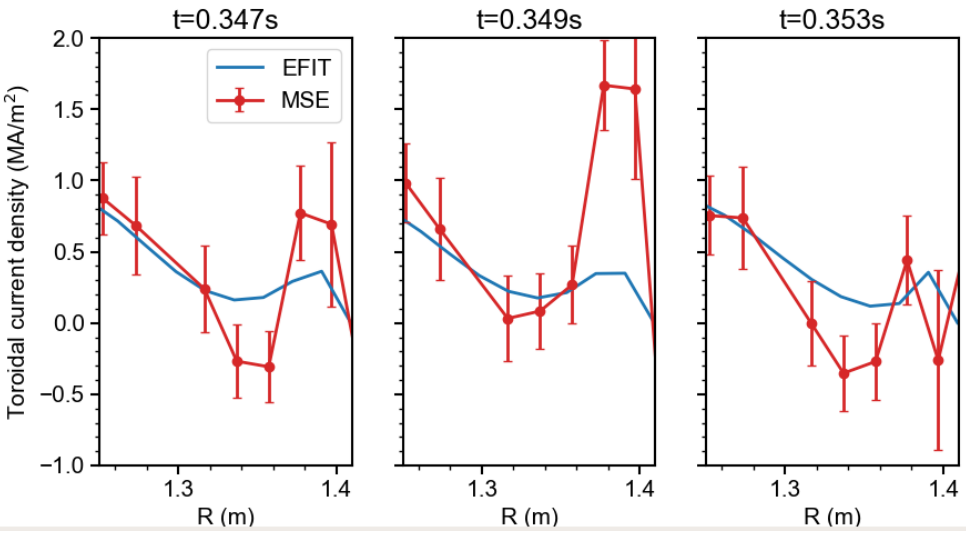

Figure 3.20: Comparison of the EFIT++ predicted (blue) and MSE measured (red) current density profiles in the pedestal region.

3.4 Outlook

3.4.1 Equilibrium development

The development of the equilibrium settings in this chapter show that the current density profile inferred using equilibrium reconstruction can be particularly sensitive to both the uncertainties in the diagnostic data and the basis function representation. To improve the equilibrium reconstruction output current profiles the accuracy in the separatrix location must increase. There will always be inherent uncertainties in the spatial calibration of the measurements, but improvements in the density and temperature profile fitting would be useful to derive a consistent boundary location between the TS diagnostic and D_α camera. If this is not the case then we can expect a large range of uncertainty in the peak current density over the pedestal region.

Other ways to improve the boundary location estimation is to increase the number of outer magnetic probes within the equilibrium, which would vastly improve the separatrix estimation. Unfortunately at this time in the campaign, many of the outer magnetics probes exhibited spurious noise or had died completely. For MAST Upgrade the array of outer magnetic probes will be greatly increased, and so this should improve the accuracy of the boundary

location without relying greatly on the D_α camera data or TS measurements.

Including an estimate of the fast ion pressure would allow improved core constraint. This could be modelled using a transport code such as TRANSP[106], and included in addition to the electron pressure measured by the HRTS system. MAST Upgrade will also benefit from increased resolution in the CXRS diagnostic for high resolution measurements of the ion temperature, and therefore the assumption $T_i \approx T_e$ could be removed and lead to a more accurate representation of the kinetic pressure profile.

To maintain consistency of the equilibrium basis functions and settings across different discharges, there will inevitably be some unconverged timeslices, for example very early in the discharge when the current profile evolves quickly, or if the current profile is particularly structured due to significant NBI heating. One way to counteract this would be to increase the number of iterations, which is useful for timeslices which almost hit the convergence criteria. On JET[107] the 'relax' factor is used to mix a proportion of the computed poloidal flux within the previous iteration step to the computed flux function for the following step. This is a common tool used in non-linear PDE solvers, particularly in computational fluid dynamics which does not have any smoothing effect on the flux functions but rather assists in the numerical stability of solving non-linear PDEs with many free parameters [108]. The algorithm is forced to search the possible solution space more slowly to find an appropriate minimum where the convergence criteria is met. This means that convergence is achieved in a much larger number of iterations but at an increased computational cost. This additionally reduces the possibility of converged timeslices which become 'stuck' in a local minima where the convergence criteria is not met.

3.4.2 Diagnostic development

Additional MSE channels within the edge region would be beneficial, as there currently only exist three fibers over the entire pedestal region, meaning the spatial gradients are coarse. At this diagnostic port it would not be possible to improve the spatial resolution of the individual measurements, due to the

inherent finite width of the neutral beam. Alternative ports were considered in the MSE design previously[52], but this port was the best compromise for tangency over the full field of view and the degree of tangency between each line of sight and the flux surfaces. For MAST Upgrade, with highly elongated plasmas, is is likely the plasma boundary location will be shifted inwards towards $R \approx 1.35$m, where the spatial resolution of the channels is marginally improved (δR$\approx$2cm).

Additional corrections could be made to the MSE data, for example correcting for the Faraday rotation due to the variation in the magnetic field over the viewing optics. The port window is made from low Verdet constant glass, and so this contribution is expected to be small. Currently there are no previous measurements available of the Faraday rotation contribution to the polarisation angle. To correct for this effect, if the current in the poloidal field coils is slowly increased in turn during a beam into gas shot, the polarisation angle offset could be measured to provide a correction look up table of the number of degrees correction per Tesla for each line of sight. This has been achieved at other tokamaks with reasonable success[47].

3.5 Summary

Details in the toroidal current profile in tokamak plasmas, such as the edge current density, is important for pedestal stability analysis. In this chapter, we looked to measure the toroidal current density profile using two approaches. As the conventional MSE polarisation angle is related to the poloidal magnetic field, we showed that the toroidal current density is derived through the spatial gradients of the MSE measurements. The demodulation technique to retrieve the polarisation angle profile is outlined. The local current density profiles derived from the data had reasonable agreement with equilibrium reconstruction, however there were discrepancies in the peak of the current density. Since the conventional MSE systems are fiber based, the distance between the fiber image projected onto the neutral beam is around R=2-3cm, which is on the order of the pedestal width, meaning resolving peaks in the profile on a length scale smaller than this is challenging.

Routine equilibrium settings to include the MSE data as a constraint on MAST were re-developed. This was achieved with a consistent set of diagnostic weights and numerical settings, across the discharges analysed in this thesis. Prior to this work the settings and weights were varied depending on the type of physics analysis (eg. focussing on core or edge physics) which meant comparing equilibrium from shot to shot was difficult. This work also helped to inform the equilibrium analysis presented using another implementation of EFIT in [94]. Improved fitting routines is critical for estimating the peak edge current density from an equilibrium reconstruction.

Chapter 4

Modelling an Imaging MSE Diagnostic for MAST Upgrade

This chapter outlines the development of a forward model and design of an imaging MSE polarimeter for the MAST Upgrade (MAST-U) tokamak. First the challenges of measuring MSE emission on MAST Upgrade is discussed and their implications for the IMSE system design. The modelling code MSESIM[52], previously used to model the conventional MSE system on MAST and K-STAR [30], was adapted by the author to model imaging based MSE systems. An additional forward model was developed to model the optical components within an imaging MSE system, and to generate the synthetic measurements presented in this chapter. This was written by the author of this thesis. The design of the system for MAST-U, analysis and interpretation of the proposed diagnostics' performance is entirely the work of the author of this thesis. Plasma equilibrium reconstructions presented in section 4.6.2 were kindly provided by Dr Andrew Thornton (CCFE).

4.1 Motivation for an edge IMSE system on MAST-U

There has been some improvement in diagnostics with routine edge current measurement capability in the last decade. Candidate diagnostics, such as

the Synthetic Aperture Microwave Imaging (SAMI) technique[1][109], measured the magnetic pitch angle in the edge pedestal on NSTX, with good agreement with even the reduced spatial resolution pedestal measurements from the conventional MSE system[110]. Combination of high spatial resolution diagnostic measurements from the SAMI diagnostic and the proposed imaging MSE system with vertical resolution improves the ability for routine local edge current measurements.

Pedestal structures were previously investigated using an IMSE system on the K-STAR tokamak, where the polarisation angle contours showed good agreement with equilibrium poloidal flux contours. Structure in the poloidal field around the separatrix was also visible during an ELM [45]. However this analysis was not extended to determine whether this structure was directly attributable to edge current, or other factors such as the radial electric field effects in the plasma edge. Therefore it would be useful to design an imaging MSE system for MAST-U, which has some strong advantages over conventional diagnostics specifically for edge current studies. Some obvious advantages of the imaging based MSE system over the conventional fibre based system include:

- 2D measurements: 2D imaging allows for measurements of any vertical variation in the polariastion angle, which can be used to infer the toroidal current density in the vertical direction ie. $\mathrm{d}B_Z/\mathrm{d}R$ across the poloidal cross section.
- Potential for improved resolution: Around 10^6 local measurements can be made using a megapixel detector. This allows a degree of flexibility over having sub mm spatial resolution per pixel, or averaging over 100s of pixels to create an n×m array of pixels with improved signal to noise by a factor $\sqrt{n_{\mathrm{pixels}}}$.
- Insensitivity to broadband polarised light: The large offset delay required to constructively interfere the π and σ MSE emission ensures that the contribution to the fringe contrast from broadband polarised light sources remains small.

[1]This technique is based upon Doppler backscattering of microwaves into the plasma to measure the magnetic pitch angle.

- Simple method to decouple polarisation information from waveplate delay: An IMSE system based on the switching FLC design subtracts any background contributions to the interferogram phase, assuming that this background does not significantly vary on a timescale equivalent to the image exposure time.

- Improved equilibrium reconstruction: Fundamental to almost all avenues of fusion plasma research requires a strong understanding of the poloidal flux function, pressure and current profiles. Increasing the level of constraint, particularly on the internal current profile, reduces the amount of potential profiles which could fit the internal measurements given their uncertainty, leading to more informed MHD analysis. Many diagnostics require channel locations to be mapped from radial positions onto a poloidal flux function which requires an accurate poloidal flux map. This process can lead to further inconsistencies between diagnostic measurements if a poorly constrained equilibrium is used.

Local current density measurements inferred from the conventional MSE system, as seen in Chapter 3, can suffer due to the finite spatial resolution of each MSE channel, causing a radial spatial smearing of the current density and greater uncertainty in the value of the current peak in the pedestal. The maximum current peak inferred from constrained equilibrium reconstruction is strongly dependent on the quality of the fits to the electron temperature and density from HRTS, positioning of the boundary/separatrix position and the basis functions used to represent p' and ff'. Local measurements using the few spatial channels in the pedestal leads to coarse point-wise measurements of the current with a high degree of uncertainty. Naturally however, any beam spectroscopy based system will be limited by the neutral beam width and divergence, but with significant improvement in the number of measurements made in the pedestal region, averaging to a smooth local measurement, a more accurate depiction of the current at the plasma edge could be achieved.

In the low aspect ratio limit $\epsilon = 1$ the bootstrap current is dominated by the poloidal field and pressure gradient,

$$j_{bs} = \frac{-1}{B_\theta}\frac{dp}{dr} \tag{4.1}$$

where p is the pressure and B_θ the poloidal magnetic field[111]. In low aspect ratio devices, where the pedestal gradient can be significantly steeper than in conventional machines, the bootstrap contribution to the edge current density is significant. Combining high resolution Thompson scattering (HRTS) measurements of the pressure profile with local measurements of j_ϕ inferred from IMSE would lead to complete ELM stability analysis using local measurements, rather than using neoclassical models to describe the current evolution[50, 51].

4.2 MSE challenges on MAST-U

Here we outline some of the challenges which must be considered when designing the imaging system for MAST-U:

As outlined in section 2.4.2, the delay applied by the birefringent crystals creates a periodic sinusoidal filter, where the period of this filter is optimised match the wavelength separation of the MSE multiplet to produce a net polarised signal. Thick (>10mm) birefringent crystals are required to produce many waves of delay needed on low field (and hence small Stark splitting) devices, producing interferogram fringes with significant curvature due to the second order dependent of delay on incident angle. These variations in the phase across the crystal can lead to distortions in the interferogram fringes, and limits the spatial resolution along the axis of interest [112].

Strong magnetic field curvature in low aspect ratio devices can lead to a significant variation in the magnetic pitch angle across the collection volume. The effect of this is a reduction in spatial resolution, but this can be minimised through careful choice of diagnostic geometry, ensuring sight lines are tangential to flux surfaces. Additional modelling of the Stark spectrum, including 3D broadening effects, means the expected spatial resolution is assessed to whether this meets the accuracy requirements for physics analysis.

The Doppler shift of the beam emission varies with beam voltage, as well as with the viewing angle between the line of sight and neutral beam. To compensate in the conventional system fiber bundles are 're-patched' to al-

ternative filterscopes to provide optimal wavelength matching with the narrowband filters. The change in Doppler shift is also more prevalent on the inboard side where the angle between the line of sight and beam axis is small. The IMSE system is tolerant to a range of beam voltages without changes to the system setup, as a wider bandpass filter is used to select the entire MSE multiplet. Considering an IMSE system using the TSSSH technique, shown in section 2.4.2, the Doppler contribution to the inteferogram phase is assumed to remain constant between two successive frames. Severe beam voltage instability between successive frames corrupts the phase encoding of the polarisation angle. This could in theory be corrected for, but only if the beam velocity distribution and variation in the velocity over time is known or accurately modelled.

4.2.1 IMSE system requirements

Measurement Uncertainty

Here we consider the diagnostic requirements in order to achieve the physics goal of measuring the evolution of the current density profile during a type-I ELM cycle. The toroidal current density is derived from the magnetic pitch angle, which as an integrated quantity means there is little variation in the pitch angle profile at the plasma edge. However spherical tokamaks by design have strong field line pitch, as the poloidal and toroidal magnetic field components are approximately on the same order. These small changes in the current distribution produce a larger change in the pitch angle and MSE measured polarisation angle than in a conventional aspect ratio device. To accurately measure the spatial distribution of the toroidal current, the uncertainty in the *spatial gradient* of the polarisation angle $\mathrm{d}\gamma/\mathrm{dR}$ is of most importance. Considering the measured current density and corresponding polarisation angle profiles from Section 3.2.5, we can reasonably estimate the change in the edge current density during the ELM cycle to be Δj_ϕ=0.6MA/m^2 with a corresponding increase in the polarisation angle of $\mathrm{d}\gamma/\mathrm{dR} = 1^\circ$ over R $\approx$ 2cm. Therefore we can set maximum limits on the uncertainty in the spatial gradient of the polarisation angle to be $\mathrm{d}\gamma/\mathrm{dR}<1^\circ$/m and $\mathrm{d}\gamma < 0.02^\circ$ at a spatial resolution of R=2cm. To achieve this level of

uncertainty in the absolute value of the polarisation angle is challenging, but some systematic effects can be accounted for through calibration and forward modelling of the optical system to include effects such as: Optical misalignment and non-uniformities, non-ideal waveplates effects, neutral beam geometry and voltage ripple effects, Faraday rotation in the port window and Stark-Zeeman ellipticity effects.

Spatial resolution requirements

The edge pedestal width on MAST-U is around 3cm[113], and so to resolve current profile over that region we require at least a spatial resolution of dR $<$ 3cm. Fiber based conventional MSE systems are limited in the minimum achievable spatial resolution due to the total diameter of the fibres ($\approx$400μm) and their spacing within the fibre bundle head, which corresponds to around 3cm spacing between the fiber footprints at the location of the neutral beam. Achieving dR $<$ 3cm spatial resolution is feasible with an imaging based system, where thousands of individual pixel measurements with millimeter resolution can be made and averaged within the pedestal region.

Temporal resolution

The temporal resolution of the system depends on the timescales relevant for physics studies. It would be feasible to measure, and be limited to the regime before and after a type-I ELM followed by a long ELM-free period, as was conducted previously on MAST[82]. The slowest ELM frequencies observed on MAST range from 250-500Hz[113], which sets an upper limit on the temporal resolution at τ=4ms in order to measure the current density evolution between multiple ELM crashes.

4.3 Modelling the MSE Spectrum

To address some of the challenges presented in section 4.2, a full spectral model is required to determine the capabilities of an IMSE system on MAST-U. When the conventional MSE system on MAST was developed, a full

spectral modelling code was written, MSESIM[52]. The goal of the MSESIM code is to simulate the MSE spectrum including 3D geometry effects, which contribute to spectral broadening. MSESIM performs Monte-Carlo sampling of the beam emission, sampling the neutral beam velocity distribution across the beam axis, the finite 3D collection volume and the 2D viewing solid angle. In essence, the overall polarisation state (and therefore total Stokes vector S_{tot} as measured at a particular line of sight is described by the sum of the Stokes vectors from each emission source within the sampled region,

$$S_{tot}(\lambda) = \int_{x,y,z} \int_{\Omega} \int_{\hat{v}} \sum_{m=-4}^{4} f(\lambda - \lambda_{\text{cwl}}) g(x, y, z, \hat{v}) S_{\text{local}}(\lambda) \mathrm{d}x \mathrm{d}y \mathrm{d}z \mathrm{d}\hat{v} \mathrm{d}\Omega \mathrm{d}\lambda, \tag{4.2}$$

where $f(\lambda - \lambda_{\text{cwl}})$ is the bandpass filter transmission function specified over wavelength λ and a peak transmission at the central wavelength λ_{cwl}, $g(x, y, z, \hat{v})$ is the 3D beam velocity distribution, $S_{\text{local}}(\lambda)$ is the local Stokes vector at a particular point within the integration grid, and Ω is the viewing solid angle [52].

4.3.1 3D Geometry

Fig. 4.1 shows the finite beam collection volume and finite solid angle of the collection lens. Across the collection volume the Doppler shift of the emission varies and broadens the measured spectrum. This also leads to a spread in the measured polarisation angle. For the IMSE system, this spectral broadening leads to a reduction in the inteferogram fringe contrast, as the delay ϕ_0 required to constructively interfere π and σ emission to achieve maximum contrast will vary over the collection volume.

The distance between the detector and collection lens is significantly smaller than the distance to the neutral beam. As such, MSESIM uses a thin lens approximation with pixels on the detector in the focal plane of the lens. In IMSE systems a three lens system is usually employed with an initial collecting lens, a second collimating lens and a third lens to image the object onto the detector. It is assumed that the spectrum produced by MSESIM is what would be imaged within the virtual image plane between the first

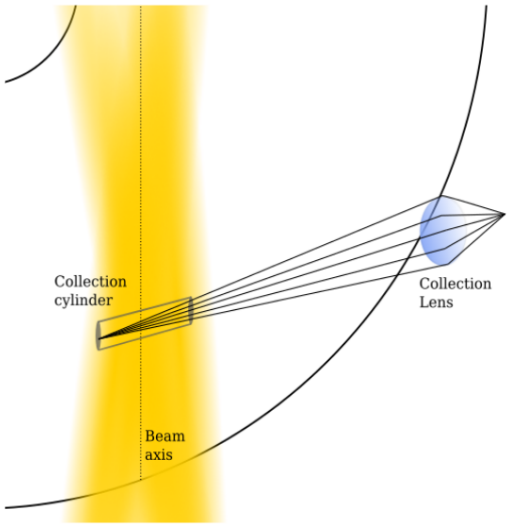

Figure 4.1: Diagram of the 3D geometric effects which lead to broadening of the MSE multiplet.

and second lens of the full IMSE system, without considering magnification effects in detail.

4.3.2 Neutral Beam

The neutral beam model in MSESIM considers the finite dimensions of the beam ion source grid, which on MAST consists of 262 circular 'beamlets' in a grid shown in Fig. 4.2. Each beamlet is assumed to have a divergence angle χ of 0.5°, such that the beam velocity is actually a distribution of 3D velocity vectors. The beamlet divergence then is related to the width of this velocity distribution, which is described by a Gaussian distribution with a half $1/e$ width. In the far field this is equal to the beamlet divergence. A beam which is strongly divergent perpendicular to the beam axis leads to the velocity distribution having a component orthogonal to the beam axis. This is particularly important to model accurately to forward model the IMSE diagnostic, as the beam velocity distribution variation can be significant in the vertical direction and can lead to asymmetric 2D polarisation angle contours [49].

Modelling the neutral beam attenuation is important to correctly model the

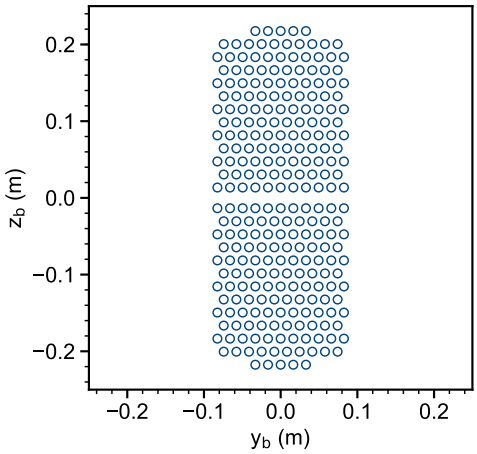

Figure 4.2: Neutral beam source grid on MAST Upgrade, consisting of 262 ion source 'beamlets' with finite angular divergence. The source focuses horizontally 14m from the ion source grid, and vertically 5.17m from the source in order to fit through the neutral beam port.

signal to noise of the IMSE system. MSESIM has a simple beam model, whereby the beam density profile is assumed to decay exponentially along the length of the beam,

$$n_{beam} = n_0 \times \exp\Big(\int_0^l -Q_{ion}(l) n_e(l) dl\Big) \tag{4.3}$$

where l is the distance from where the beam crosses the LCFS, Q_{ion} is the ionisation rate of beam particles, the derived effective beam stopping coefficient from ADAS [114]. Perpendicular to the beam axis, the beam density has a Gaussian profile. To calculate the beam emission rate, the electron density n_e is assumed to be a quadratic function of ψ, and calculated given a specified electron density at the magnetic axis position. The typical operating regime for MAST-U is between 3-4$\times 10^{19}$m^{-3}. This could be improved by providing measured electron density profiles from the HRTS system when MAST-U plasmas are available. The profiles of the beam emission rate, beam density is shown in Fig. 4.3.

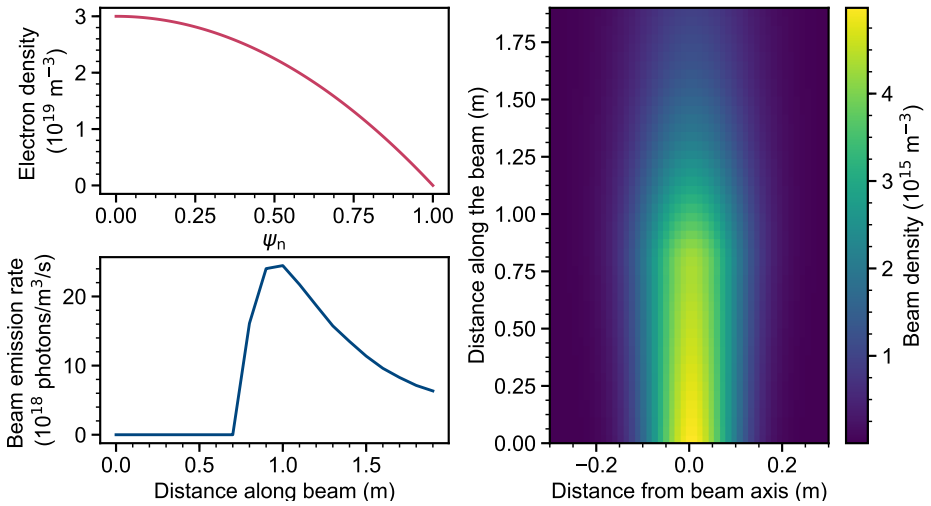

Figure 4.3: Top left: Parabolic electron density profile as a function of normalised poloidal flux. Bottom left: Beam emission rate as a function of distance along the beam. In this case the plasma boundary is located 0.7m from the beam duct. The beam emission rate then attenuates as the plasma density increases. Right: Beam neutral density along the beam and across the beam axis. This graph illuminates the collection volume which each line of sight is integrated over to retrieve the modelled spectrum.

4.3.3 Stark-Zeeman States

Since the original MSESIM publication was written[115], there have been a number of improvements to the code focussing on atomic modelling [116]. In Sections 2.1.2 and 2.1.1 the perturbation to the energy levels of the atom placed within a external electric or magnetic field were outlined. For the fast neutral beam atoms, they experience both the generated Lorentz electric field E = V x B and the plasma magnetic field. Normally the influence of the Zeeman effect on the MSE spectrum is neglected, but can contribute a significant circular polarisation fraction. Comparing the relative strengths of the Stark splitting ϵ and Zeeman splitting γ for MAST-U,

$$\frac{\epsilon}{\gamma} = \frac{6ea_0m_e|\mathbf{E}|}{e\hbar|\mathbf{B}|} \approx 6. \tag{4.4}$$

for a beam velocity of $v = 2.6 \times 10^6$m/s and beam injection angle relative to the magnetic field of 58.7°. It is expected then that the Stark effect dominates due to the low magnetic field on MAST, but the inclusion of the Stark-Zeeman states allows for the circular polarisation fraction to be calculated.

Other significant additions to the code, which is more MAST relevant, are the unequal π/σ line intensity ratios, which assume a non-statistical upper state populations calculated by Gu [66]. Non-statistical upper state populations occur in the Stark-Zeeman lines at low plasma densities. We must note that, although development of the atomic physics model was not within the scope of this thesis, other work such as Thorman[49] has pointed out that there are errors in the implementation of the model by Gu[66]. An improved model of the statistical populations at fusion relevant plasma densities has been done by Marchuk[117], however does not address the Zeeman effect. Further development of the MSESIM code should look to apply the non-statistical state populations from [117] at MAST-U plasma densities and beam energies to the Stark-Zeeman states given by Thorman [49] for a more complete atomic model. If the line intensity ratios are modelled incorrectly then this can lead to incorrect determination of the circularly polarised fraction, which can be up to 10% on MAST. For the IMSE system design however, as long as the interferometric delay is optimised to maximise the linear polarisation fraction then the Stark-Zeeman circular polarisation contribution to the measurements should be minimised.

4.3.4 Diagnostic Geometry

Finally to model the synthetic spectra appropriately we must consider the diagnostic geometry. Fig. 4.4 shows the location of MSE diagnostic port relative to the south-south (SS) neutral beam axis. We expect then the modelled wavelengths are Doppler red-shifted with respect to the D_α wavelength.

To accurately model the spectrum to produce forward modelled 2D images, the location of the pixels with respect to the optic axis must be considered, assuming that the center of the sensor aligns with the center of the diagnostic collection lens. The geometry in the collection lens co-ordinate system is also shown in Fig. 4.4 for a d=38mm diameter lens, and focal length f=85mm, with the Photron-SA4 square CMOS sensor pixel locations overlaid. The specific diameter and focal length of the collection lens was as an initial starting point for the design process, as these lens properties are similar to the collection lens for the conventional MSE system and provide a good field

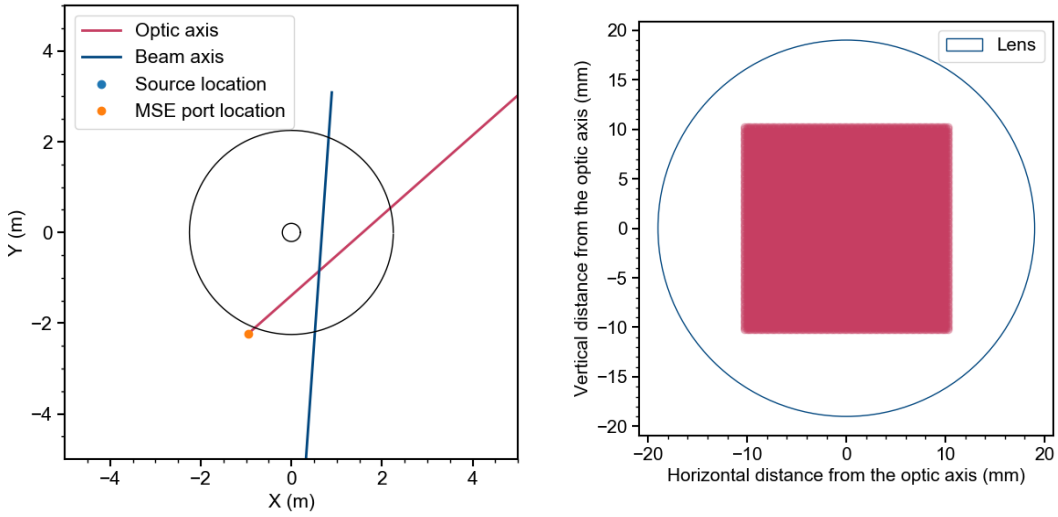

Figure 4.4: Left: Top down view of the MAST tokamak in machine co-ordinates. The intersection between the diagnostic optic axis and the SS neutral beam is shown. Right: In the collection lens co-ordinate system, the sensor pixel locations are shown with respect to the optic axis of a 38mm diameter lens used for the modelled collection lens.

of view across the plasma. Additionally choosing a system with 1:1 magnification allows us to overcome the simplistic single lens model in MSESIM. Naturally one could choose a different focal length for the collection lens to the collimating and final lens, at which point both vignetting and magnification of the image between the intermediate and final image on the sensor would need to be considered.

4.3.5 Resulting Spectrum

An example of the resulting spectrum from MSESIM is shown in Fig. 4.6, for both an edge (R=1.2m) and core (R=0.92m) channel. In Fig. 4.5 the resulting spectrum from using a simplistic 1D model where a mono energetic beam of infinitesimal width is assumed is presented. The fully modelled spectrum shows that the π and σ components are unresolvable, resulting in a single Gaussian shape for the spectral intensity, instead of the distinct transition lines shown in the ideal spectrum.

Asymmetric spectral broadening of the π wings is apparent, arising from inclusion of the spread of beam energies and the finite collection volume,

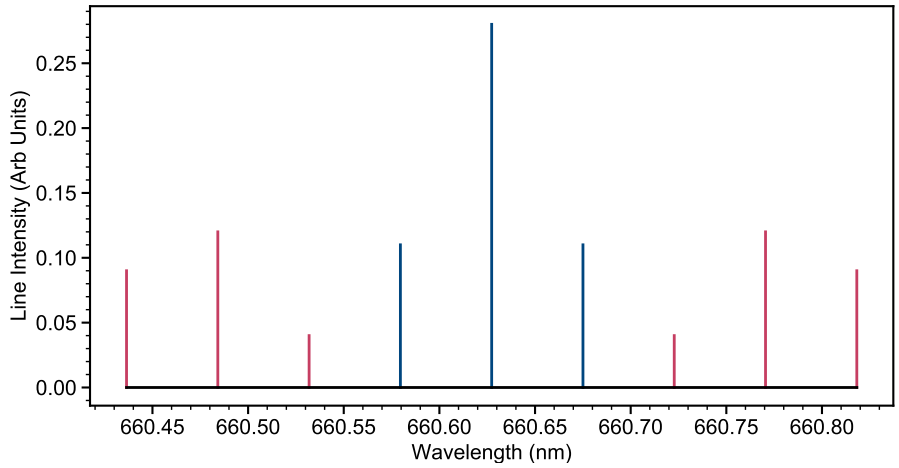

Figure 4.5: Simple MSE spectrum assuming the neutral beam is infinitesimally thin, such that the transition lines are unbroadened and are represented by delta functions. Bright π transition lines are shown in red, with σ transitions shown in blue.

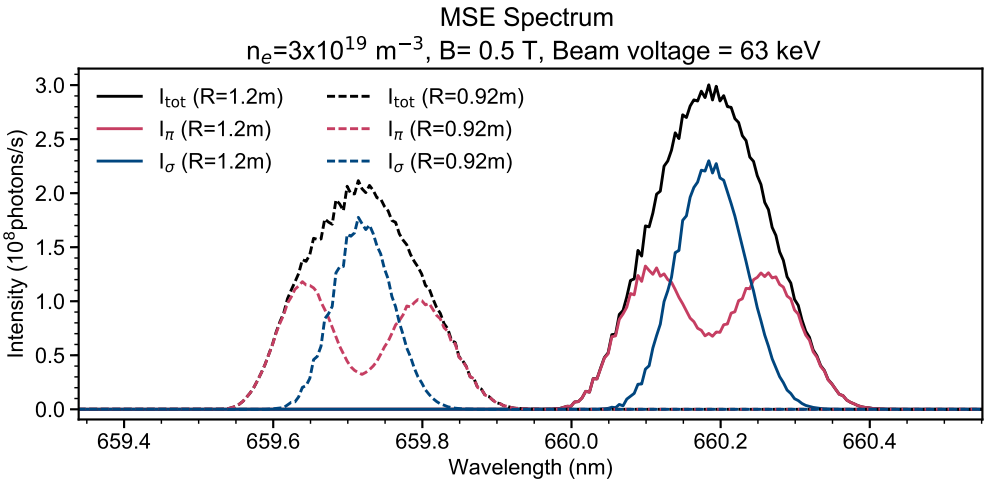

Figure 4.6: Modelled MSESIM spectrum including spectral broadening due to finite collection lens, 3D collection volume and beam divergence. The spectrum as measured by the detector (black), where π (red) and σ components (blue) become fully blended and unresolvable. The spectrum for a core channel at R = 0.92m (dashed line) and for an edge channel at R=1.2m (solid line) is shown. The beam emission attenuation is evident, given the lower total intensity for the core channel vs the outer edge channel.

with the width of π^+ component at $\delta\lambda$ = 0.1nm compared to $\delta\lambda$=0.05nm for the π^- component. Neutral beam atoms with a higher beam velocity experience an increased Doppler shift towards longer wavelengths. For the π^- component (blue shifted with respect to the central σ component) this

increased Doppler shift is counteracted by the Stark splitting, which acts to increase the wavelength separation between the transition lines within the π^- component. For the redshifted π^+ components, both the Stark shift and Doppler shift act to move the π^+ wing towards longer wavelengths, leading to the asymmetric broadening of the π wings in Fig. 4.6. This effect is more apparent for the core channels, where the Stark shift is increased due to the higher magnetic field.

Note that a similar effect occurs due to the viewing volume across the finite neutral beam width. This leads to a variation in the magnetic field and beam velocity vectors across the viewing volume. Towards the far side of the beam, at a point further into the plasma there is an increased magnetic field strength and increased Stark shift, and also the view angle with respect to the far side of the beam is more shallow, increasing the Doppler shift of the emission. These effects then combine to increase the spectral broadening for the π^+ components, and counteract for the π^- wing, leading to the observed asymmetry within the modelled spectrum. Considering the impact of the asymmetry of the MSE spectrum for the IMSE system, this would act to change the period of the sinusoidal filter required for maximum net polarised signal and lead to a reduction in the fringe contrast for channels viewing towards the plasma core.

4.4 Generating Forward Modelled Images

Now the spectrum output from MSESIM is coupled to a python forward model developed to generate the synthetic interferograms. A flowchart is presented in Fig. 4.7, where the process to convert the output Stokes vector from MSESIM to a measured signal by the observer. After the displacer and delay plate crystal properties are defined, the refractive indices n_e, n_0 are calculated using Eq. 2.28. Then the phase delay imposed by the waveplates is calculated using Eq. 2.30. The polarimeter response is then calculated using Eq. 2.37 to find the measured light intensity. Light intensity, measured in photons/s, is converted into analog to digital units (ADU) as measured by the detector. Read noise is added to the ideal images by taking the number of photo-electrons N on a pixel and including random sampling of a Gaussian

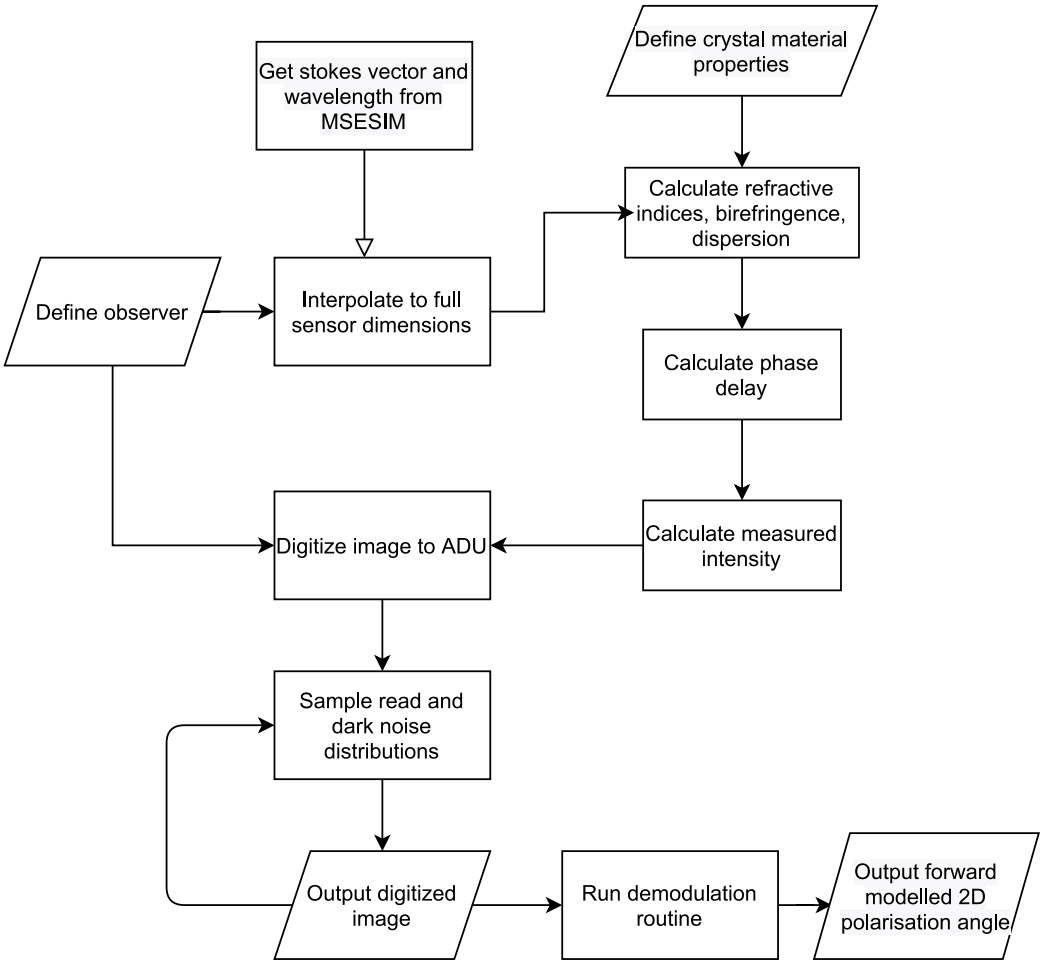

Figure 4.7: Code workflow to generate the forward modelled IMSE images. The source code is available at: https://github.com/sgibson-mse/IMSE/

distribution $\mathcal{N}(\mu_N, \sigma_{\text{read}})$ with a mean μ_N and standard deviation σ_{read} given by the read noise in electrons/count by the manufacturer. Shot noise is also included by sampling a Poisson distribution with $f(N, \sqrt{N})$. These distributions are sampled 5000 times in order to obtain a true measurement of the standard deviation in the polarisation angle due to noise.

The polarisation angle as measured by the polarimeter is retrieved through Fourier demodulation of the interferograms S_+ and S_-. Information retrieved from the interferogram includes the fringe contrast ζ, dependent on the beam emission relative to the background emission intensity, as well as the net spectral polarisation fraction. The difference of the interferogram phases retrieves the polarisation angle γ, and the sum of the interferogram phases retrieves the delay $\phi(\alpha,\beta,\lambda)$, which can be used to calculate the Doppler

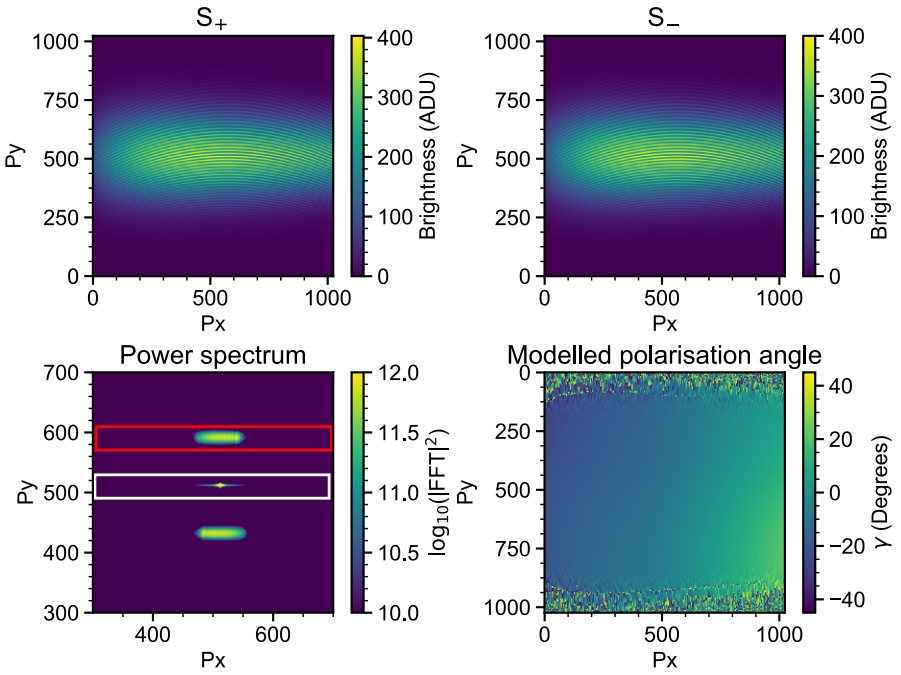

Figure 4.8: Synthetic images generated for both states of the FLC. The power spectrum of the Fourier transform for a single interferogram is shown, where the carrier frequency is highlighted within the red rectangle, and DC frequency within the white rectangle. The phase and amplitude of the DC and carrier frequencies are extracted for the S_+ and S_- interferograms. The demodulated noisy polarisation angle is retrieved (bottom right).

shifted emission wavelengths. Fig. 4.8 shows the demodulation process used to extract the phase and contrast information. The phase is extracted from the interferogram by performing a discrete Fourier transform (DFT) and filtering the carrier frequency using a 2D window function, such as the Hann window. Its tapered profile allows sharp edges, between signal and noise boundaries and at the edge of the images to be apodised and reduces the chance of signal ringing and artifacts in the demodulated polarisation angle.

4.4.1 Computational considerations

The majority of the MSESIM code was written in the IDL programming language. One of the main drawbacks of the code is the calculation time. The main spectrum calculation routine loops through each individual channel to calculate the Stokes vector as a function of wavelength. The compu-

tational time required per channel depends on the number of beamlets to integrate over for the beam divergence calculation, and the number of segments the collection lens is divided into. The calculation time for a single channel when integrating over the entire 252 neutral beam ion source 'beamlets' takes approximately 22 seconds per pixel. Ideally the spectral intensity S(x,y,λ) would be modelled for every pixel in the image to generate full resolution spectral intensity, but for a single megapixel image, at full beamlet resolution, this corresponds to a run time of at least 267(!) days. To improve computational speed the resulting spectrum is modelled on a sparse grid of 32x32 grid of pixels for quick computations or 200x200 for the images presented in this chapter, as opposed to every pixel co-ordinate on the sensor. These grids are then interpolated to the full sensor size, as shown in Fig. 4.9.

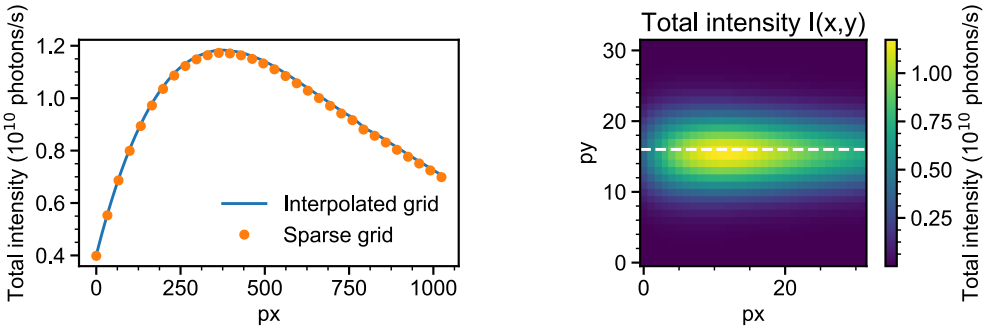

Figure 4.9: The total modelled intensity S_0 for the sparse 32x32 sampling grid.

4.5 Diagnostic Design

In this section the design and optimising process of the IMSE system is outlined. The components were designed based upon the magnetic field strengths and beam energy capabilities of the previous MAST tokamak. In Table 4.1 the individual system components and their properties are outlined as informed by the design work, with further reasoning outlined within the following subsections.

For MAST-U plasmas there will be an increase in the toroidal field strength ≈0.9T at absolute maximum capabilities, as shown in the MAST Upgrade

Component	**Properties**
Collection Lens L_1	Focal length f=85mm Diameter d = 38mm
Collimating Lens	Focal length f=85mm
Delay Plate	α-BBO uni-axial waveplate Optic axis cut angle Θ = 0 ° Thickness L=15mm
Displacer Plate	α-BBO uni-axial waveplate Optic axis cut angle Θ = 45 ° Thickness L=3mm
Bandpass Filter	λ_{cwl} = 660.2m (0° AOI) FWHM = 1.2nm Three-cavity filter
Camera Lens L_3	Focal length f = 85mm
CMOS Camera	Photron SA-4 CCD 1024 x 1024 pixels Pixel size 20 x 20 μm 12 bit ADC

Table 4.1: Overview of the IMSE components and their properties, used for modelling synthetic diagnostic MAST-U measurements. Further camera specifications can be found in Table 4.2.

scenarios used to predict the diagnostic performance. For the first campaigns however for monitoring of the stress on toroidal field coil joints the magnetic field strength will be approximately 0.5T. The interferometer design is based upon a MAST plasma equilibrium, as at the time MAST-U equilibrium were not readily available. At this shift in the magnetic field strength, the increase in the Stark shift is $\lambda_S = 0.025$nm. This increased magnetic field strength, whilst keeping the same delay plate, would shift the delay by less than half a wave. Even with the increased field strength this delay would still produce a net polarised signal, at a slightly reduced contrast, but the measurement is feasible.

4.5.1 Choice of Interferometer Components

Choosing interferometer components requires careful consideration of the appropriate material, thickness and cut angle of the optical axis to constructively interfere π and σ components and produce a net polarised signal. Using Equation 2.30 to calculate the phase shift $\phi(\lambda)$ for a given a range of delay and displacer plate thicknesses, the fringe contrast was calculated for the given spectrum using the amplitude of the Fourier transform in equation 2.36 of the individual emission lines in the MSE multiplet and the sinusoidal filter introduced by the delay and displacer plates.

In Fig. 4.11, the fringe contrast across the field of view is calculated using the realistic broadened spectrum from MSESIM in Fig. 4.6. Simulating the fringe contrast with the 'ideal' spectrum where broadening effects are not considered, the predicted contrast averages 80% across the field of view. Calculating the fringe contrast using the ideal spectrum does not reach 100%. The MSE multiplet consists of 9 bright transition lines, with three transition lines encompassed within each of the π^+, π^- and σ components in the MSE spectrum. The sinusoidal filter period is matched to the period of the mean wavelength for the π wings and σ component and so some contrast is lost due to this inherent line width and summing of these individual interferograms. From Fig. 4.11, targeting a combination of waveplate thicknesses which apply a total delay of $\phi = 2814$ waves, as shown by the white dashed line, would achieve the maximum possible contrast for emission at $\lambda = 660$nm. The

displacer optic axis cut angle and thickness is generally chosen first alongside the camera lens focal length, to optimise the fringe frequency. Then any combination of plate thicknesses up to 18.8mm would be appropriate to satisfy the required number of waves of delay to obtain maximum (or near maximum) fringe contrast. The chosen properties of the crystals can be found in Table4.1.

The fringe contrast in Fig. 4.11 ranges from 20% in the core to 40% at the plasma edge, where the beam emission intensity is strongest. Across the field of view there is a reduction in the available fringe contrast of 20%. This reduction in contrast across the plasma is due to a combination of increased Doppler broadening for the most red shifted wavelength emission and decreasing tangency to flux surfaces which increases the contribution of line integration to spectral broadening. However there are competing effects which would act to improve the fringe contrast; The toroidal magnetic field increases towards the inboard side of the machine leading to increased Stark splitting and reducing spectral broadening and increasing net polarisation fraction.

Impact of Background Emission

Up to this point, only changes in the fringe contrast and fringe intensity due to 3D geometry and spectral broadening effects have been considered. Additional sources of broadband background light are present in tokamak plasmas, where the dominant background emission is due to visible Bremsstrahlung, where the emissivity is given by[118],

$$\epsilon(\lambda) = \frac{0.95 \times 10^{-19}}{4\pi\lambda} g_{\text{ff}} n_e^2 Z_{\text{eff}} \sqrt{T_e} \times \exp\left(\frac{-hc}{\lambda T_e}\right) \tag{4.5}$$

where λ is the wavelength in units of nm, T_e is the electron temperature in units of eV, n_e is the electron density in units of m^{-3}, Z_{eff} is the effective ion charge which is approximately 1.2 for MAST[119] and g_{ff} is the Gaunt factor, which is approximately 3 for fusion relevant electron temperatures [118]. While broadband sources of unpolarised emission do not contribute to the interferogram fringes, the presence of unpolarised emission reduces the

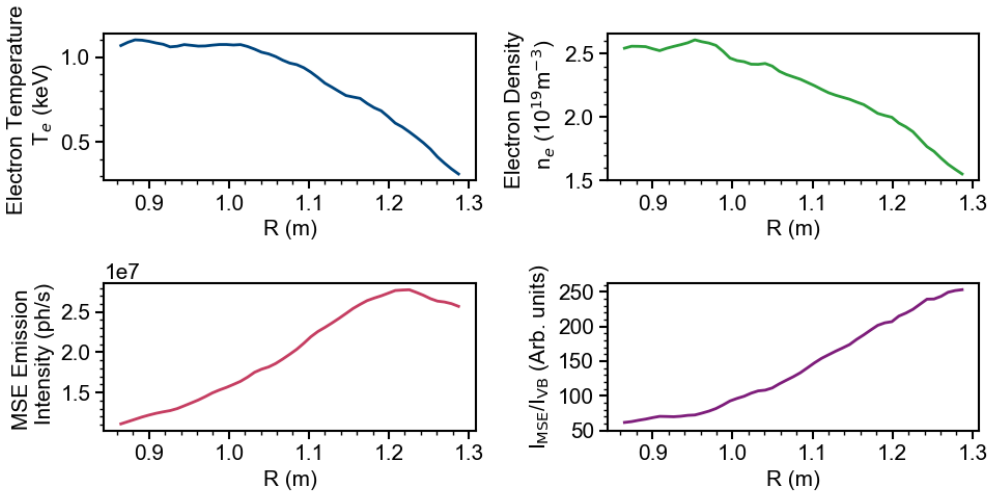

Figure 4.10: **Top:** Electron temperature (left) and electron density (right) profiles as measured by the Thomson scattering system[1], from MAST plasma 24409 at t=0.25s. Data provided from the MAST database. **Bottom:** Modelled MSE emission intensity (left) across the plasma, and the ratio of the predicted MSE emission and calculated visible bremsstrahlung (right).

fringe intensity, and reduces the signal to noise ratio.

Using typical electron temperature and density profiles for MAST plasmas, as shown in Fig. 4.10, the expected level of visible bremsstrahlung is calculated. The ratio of the MSE emission intensity relative to the visible bremsstrahlung is shown in Fig. 4.10. In the core region of the plasma the level of bremsstrahlung is largest, as bremsstrahlung scales with n_e^2. In the plasma edge region, the beam emission is still orders of magnitude larger than the predicted Bremsstrahlung emission, and so a large net polarisation fraction can still be achieved. Therefore, for edge IMSE measurements the Bremsstrahlung contribution is anticipated to be small.

Field-widened Delay Plate

The displacer plate thickness was chosen to be as thin as possible to reduce the impact of the hyperbolic phase term from equation 2.32. The cut angle was then chosen to be $\Theta = 45°$ to maximise the fringe contrast across the field of view and minimise the contribution of $\phi_{\text{hyperbolic}}$. At this cut angle

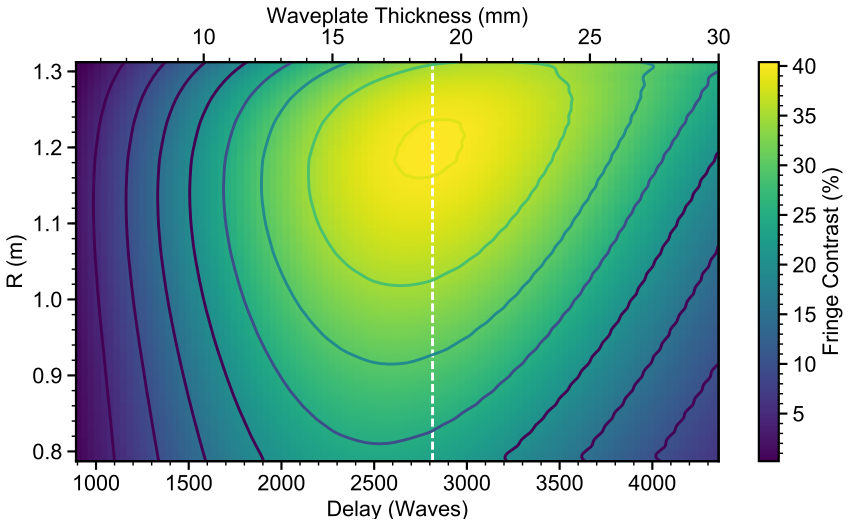

Figure 4.11: Fringe contrast variation with applied delay in waves. The corresponding waveplate thickness is plotted as an additional x axis. Maximum contrast is achieved across the plasma with a combined thickness of L=18.8mm for the delay and displacer plate. However there is a range of delays which would produce sufficient fringe contrast, and so a trade off between introduction of fringe curvature for increasing plate thickness and maximum fringe contrast must be considered.

the highest fringe frequency per thickness of the displacer is achieved.

Including the optimised displacer and delay plates within the IMSE forward model, the modelled interferogram fringes are strongly curved towards the edges of the image sensor. The effect can be compensated for using the field widening technique [44, 120], where the delay plate can be split into two delay plates of equal thickness, and a half waveplate sandwiched in between. This then acts to switch the ordinary and extraordinary rays in the second plate to 'cancel out' the unwanted second order hyperbolic pattern in the delay. Fig. 4.12 shows the difference in the fringe curvature for a modelled system with and without the field widened delay plate. In these regions the fringe frequency is decreased which reduces the horizontal spatial resolution. Evidently using a field widening plate reduces the fringe curvature, but does not eliminate it entirely, as some residual fringe curvature remains due to the displacer waveplate. With additional plates in the optical system, there could be additional surface reflects at the interfaces between the plates in the field widened delay plate, but these can be counteracted with anti-reflection

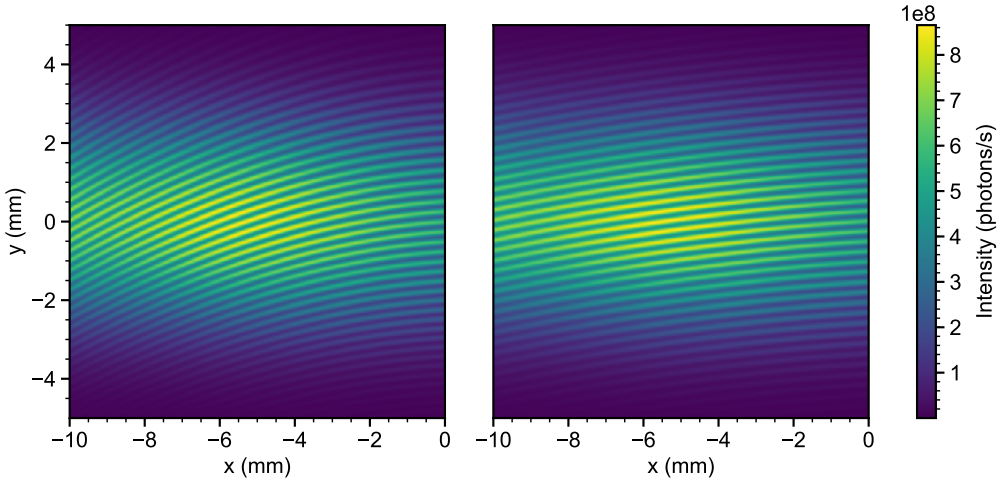

Figure 4.12: Comparison of modelled interferogram fringes with (right) and without (left) a field widened (FW) delay plate. Fringe curvature is reduced when including FW delay plate, however some residual curvature remains due to contributions from the displacer plate.

coatings at each interface.

4.5.2 Choice of Fringe Frequency

The number of pixels each fringe in the inteferogram spans, known as the fringe frequency k_y in Eq. 2.32, is set by the crystal thickness, optic axis angle and the focal length of the final camera lens. The spatial resolution along the axis perpendicular to the interferogram fringes is set by the fringe frequency. One must make a trade off between the fringe frequency and fringe contrast; High fringe frequencies lead to a reduced fringe contrast (and therefore reduced signal to noise) due to imperfect focussing of the final lens. A fringe frequency of 10 pixels per fringe would provide a fringe width of $\approx$ 0.2mm on the photron sensor, and corresponds to $<$ 0.5cm resolution in the plasma across the vertical extent of the beam. Previous coherence imaging systems have performed well with good spatial resolution at similar fringe frequencies [121].

Although it may seem in Fig. 4.13 that a steep optic axis cut angle would improve the fringe frequency, when combined with a short focal length camera lens the second order incidence angle effects become more significant leading

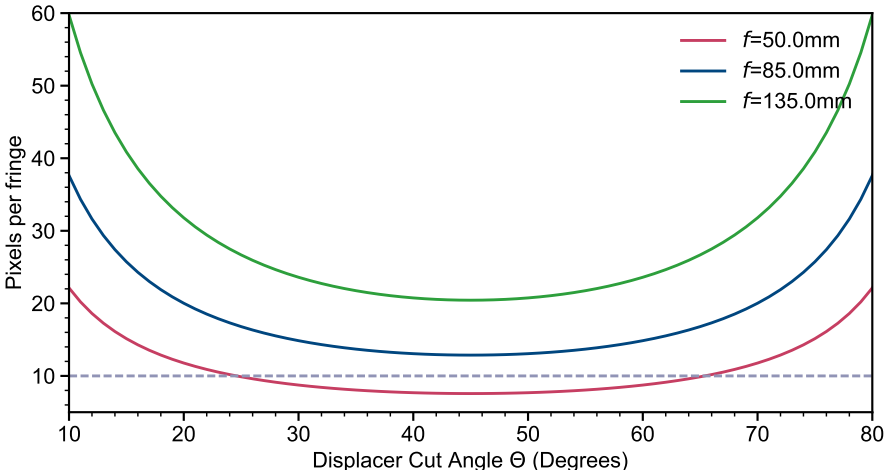

Figure 4.13: Interferogram fringe frequency as a function of optic axis cut angle Θ for a range of focal lengths. The 'cut off' fringe frequency of 10 pixels per fringe is shown (dashed grey line). At $\Theta = 45°$ both an $f = 85$mm and $f = 135$mm lens would provide sufficient fringe frequency. For further modelling an $f = 85$mm final lens is used, as this provides a good field of view across the plasma. Other lens combinations could be considered with additional optical modelling.

to curved fringes at the sensor edges. Therefore we optimise the cut angle and final lens focal length to both reduce fringe curvature and provide good fringe frequency. Using an $f = 85$mm lens and cut angle $\Theta = 45°$ achieves 13 pixels per fringe.

4.5.3 Detector

Two cameras were considered for the choice of detector; A Photron-SA4, currently available within the department, and the PCO-edge 5.5 camera, previously used within the IMSE system on the K-STAR tokamak. The Photron camera is capable of exposure times down to 1ms resolution, which would be necessary to study dynamics within a slow ELM period. The limiting specifications of the Photron camera is the read out noise, which is high due to noise on the signal amplifier. Full specifications of both cameras are compared in Table 4.2. The quantum efficiency of the Photron is poor (QE $< 40\%$) in the wavelength region of interest ($\lambda \approx 660$nm), something where a more efficient sCMOS sensor would prove beneficial, particularly if the signal to noise is low.

The signal to noise was analytically calculated using the camera specifications and calculating the number of photons incident on each pixel from the MSESIM model for a given exposure time τ,

$$I = n_\gamma F \eta \tau G \tag{4.6}$$

where F is the fill factor of the pixels, η_γ is the quantum efficiency of the detector and G is the detector gain. The SNR is then,

$$\text{SNR} = \frac{I}{\sqrt{\sigma^2_{\text{read}} + \sigma^2_{\text{shot}} + \sigma^2_{\text{dark}}}}, \tag{4.7}$$

where σ_{read} and σ_{dark} were provided by the manufacturer, and σ_{shot} was calculated using the method outlined in section 4.4.

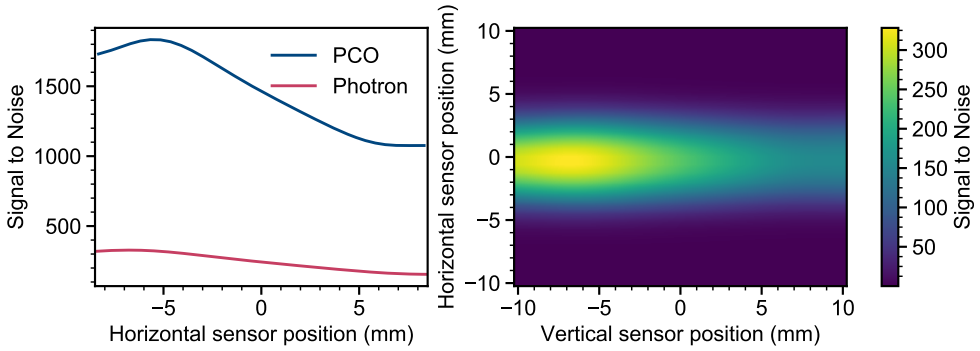

Figure 4.14: **Left:** Signal to noise ratio of the Photron-SA4 camera at exposure time $\tau = 1$ms and the PCO-edge 5.5 camera at $\tau = 5$ms across the centre of the image. **Right:** SNR across the Photron detector given the photon intensity modelled using MSESIM. Beam attenuation lowers emission intensity towards the inboard side of the plasma, leading to reduced SNR.

Fig. 4.14 shows the SNR across the center image for the PCO and Photron cameras for their minimum exposure time of 5ms and 1ms respectively. Evidently the SNR is significantly improved for the PCO camera due to lower read noise and longer exposure time. The 12 bit ADC of the Photron camera has a lower dynamic range than the PCO-edge 16 bit ADC, but even if the gain

	PCO Edge	**Photron SA4**
Pixel Size (μm)	6.5 x 6.5	20 x 20
Readout (rms e-)	2.2	41.2
Dark noise (e-)	2	3.55
Gain (e-)	0.46	11
Pixel Fill Factor	100%	50%
Quantum Efficiency ($\lambda = 660$nm)	54%	42%

Table 4.2: Specifications of the PCO-Edge 5.5 and Photron-SA4 cameras

were to be reduced on the sensor, it would be more likely to saturate with a large fraction of the dynamic range is wasted due to high readout noise.

Realistically only the dynamics of type-I ELMs with a low repetition rate, or between long ELM free periods, could be studied with temporal resolution at 5ms or longer. To improve the SNR pixel binning could be performed. This could be particularly useful for the photron camera, where reading out fewer pixels could improve the camera read out time, but must be considered carefully as this would also reduce the interferogram fringe resolution. Post demodulation, downsampling of the measured polarisation angle would improve the uncertainty in the measurement. Assuming the noise on each pixel is shot noise limited, the uncertainty in each pixel is given by $\sqrt{N}$ where N is the number of measured photons. If these pixels were then downsampled by a factor m the standard error on the measurement improves by a factor $1/\sqrt{m}$. Evidently, assuming square bins are used, this also reduces the resolution by a factor m. Other methods without sacrificing individual pixel resolution could be considered, such as averaging profiles using several similar ELM cycles within plasma shot to obtain accurate profiles [118, 122].

4.5.4 Bandpass Filter

A bandpass interference filter was designed to select the full energy component MSE multiplet. Bandpass filters consist of multiple cavities made from thin film dielectric layers with different refractive indices. Varying the space between layers and number of cavities, the central wavelength, and

optical transmission profile can be tuned over the wavelength region of interest. Generally these bandpass filters are designed to work for low angles of incidence (AOI) and so must be placed within the collimated region of the optical train to reduce the range of incidence angles through the filter. The central wavelength of the filter is blue shifted according to the incident angle,

$$\lambda_\alpha = \lambda_0 \sqrt{1 - \left(\frac{\sin\alpha}{n*}\right)^2} \tag{4.8}$$

where λ_0 is the wavelength at normal incidence and $n*$ is the refractive index of the bandpass material.

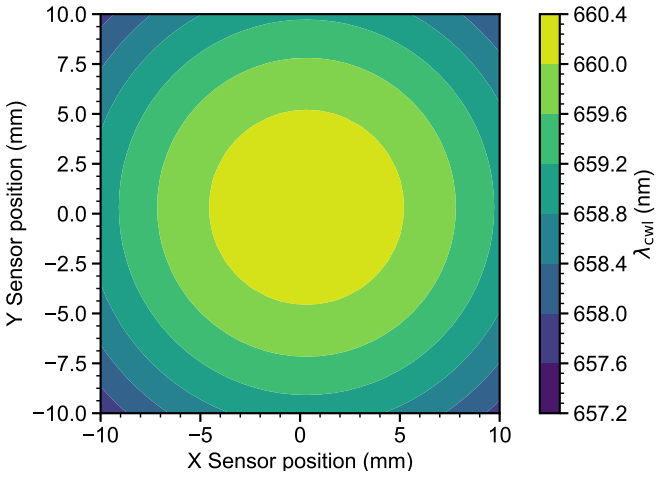

Figure 4.15: Blue-shift of the bandpass filter center wavelength ($\lambda_{\text{cwl}} = 660.2$nm for axial rays) for the range of incidence angles α, made from material with an effective refractive index n_*=1.85.

For the IMSE system, a bandpass filter must be designed such that:

- Second and third beam energy components and any nearby polarised contaminant lines are avoided.
- The full energy multiplet is captured entirely across the field of view. Clipping the spectrum can lead to small shift in the measured polarisation angle, due to beam divergence effects.
- The full width half maximum (FWHM) of the filter must be wide enough to tolerate variation in neutral beam voltage.

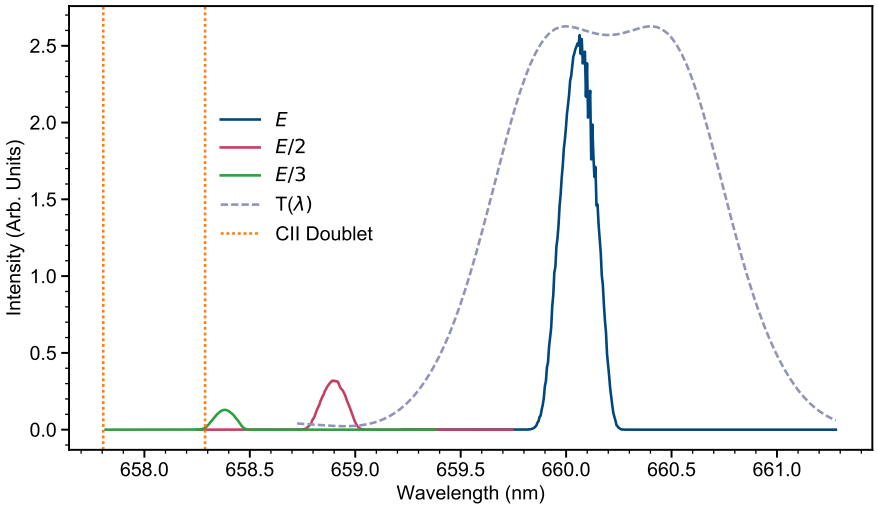

Figure 4.16: Full, half, and third energy components of the MSE spectrum modelled at R=1.04m. The filter transmission function (dashed light blue) has been scaled relative to the intensity of the full energy component. For the center of the sensor, at low incidence angles, the full energy multiplet is entirely captured, and the second, third energy components and nearby contaminant carbon II lines (orange dotted) are avoided.

As the MSE multiplet is Doppler shifted depending on the angle between the neutral beam and each line of sight, the central wavelength blueshift effect is used advantageously to avoid spectral clipping when designing the bandpass filter. In Fig. 4.16 and Fig. 4.17, the modelled spectral intensity is shown for both a central and edge pixel on the sensor. At the extreme edges of the sensor the incidence angles can reach up to $\alpha = 6°$, leading to a significant blue shift of the filter central wavelength. By tilting the filter away from the vertical axis, in this case by $\theta_{\text{tilt}} = -2°$, this effect can be somewhat negated, such that the spectrum can be fully captured by the bandpass filter across the field of view. Fig. 4.16 and Fig. 4.17 show the predicted bandpass transmission profile $\lambda_{\text{CWL}} = 660.2$nm (at 0° AOI) with a FWHM= 1.2nm, with the spectrum modelled for a central and edge pixel. Nearby CII contaminant lines are shown as dotted lines, which are outside of the bandpass filter range. If these carbon lines were to be included within the bandpass filter and this emission was partially polarised via reflection then this would shift the measured polarisation angle.

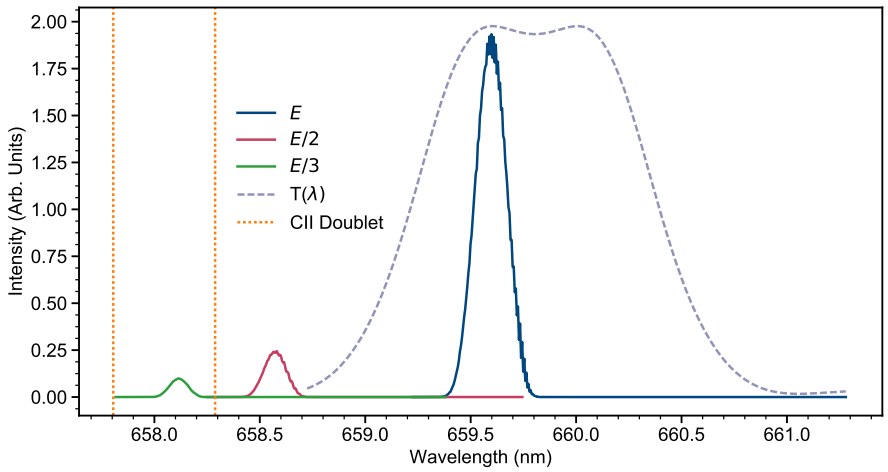

Figure 4.17: Full, half, and third energy components of the MSE spectrum modelled for an edge pixel at R=0.791m. Note that due to the increased incident angle the central wavelength of the filter is blue-shifted.

4.5.5 Spatial Registration and Radial Resolution

The diagnostic field of view is shown in Fig. 4.18 across a typical low elongation MAST-like plasma, for a collection lens with focal length f=85mm. This allows for retaining measurements at the magnetic axis position, which provide a reference zero polarisation angle (ie. $B_z = 0$) for calibration. The location of the zero angle can then be cross checked against the conventional MSE system or a kinetic equilibrium for absolute offset measurement. If required, a longer focal length lens could be used (f=135mm), without sacrificing fringe frequency, to zoom in to the pedestal region with adjustment of the optic axis. However, for higher elongation plasmas on MAST-U the boundary location is expected to be at $R \approx 1.35$m, which is close to the center of the field of view, and so changes to the front lens may not be required.

It is not possible to significantly improve upon the radial resolution of either the conventional or imaging MSE system. The finite neutral beam width and intersection angle between the beam and line of sight sets a fundamental limit on the maximum radial resolution that can be obtained due to line integration effects, with an average of ΔR= 2cm across the field of view. The spatial resolution for the diagnostic is shown in Fig. 4.19, where the radial resolution is calculated as the distance over which 80% of the beam

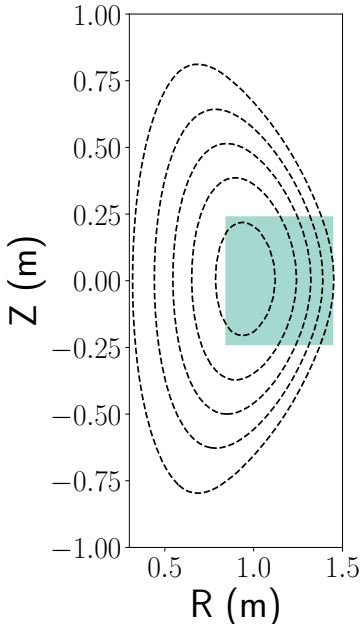

Figure 4.18: Field of view for the diagnostic (shaded square region) projected upon poloidal flux contours (black dashed lines) of a mast plasma.

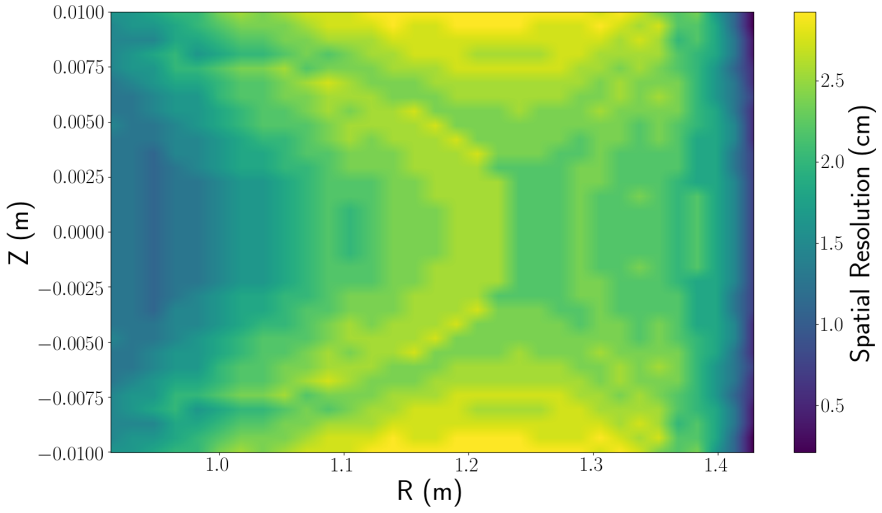

Figure 4.19: Spatial resolution across the field of view. MAST-U plasmas will likely have a separatrix position ranging between R≈1.35-1.4m depending on the elongation.

emission is captured within the collection volume. An imaging system will provide more spatial information (in the form of more spatial measurements compared to the conventional system) which can be averaged over to reduce

uncertainty in any sharp changes to the polarisation angle profile and could be used to compare two models of the predicted bootstrap current. In Fig. 4.19 the beam divergence effects become apparent, where the spatial resolution is lower further away from the beam center-line.

4.6 Modelled Performance

4.6.1 MAST plasma

Forward modelling the synthetic images revealed that for the high powered beam cases, the 12 bit ADC detector of the Photron camera would become saturated at 2ms time resolution. However, including a reduction in the intensity due to absorption/reflection of the incident light through the optical system, the saturation is reduced as shown in Fig.4.20. To run at longer exposure times with this camera, then an additional neutral density filter could be obtained, or use a camera with a higher bit depth.

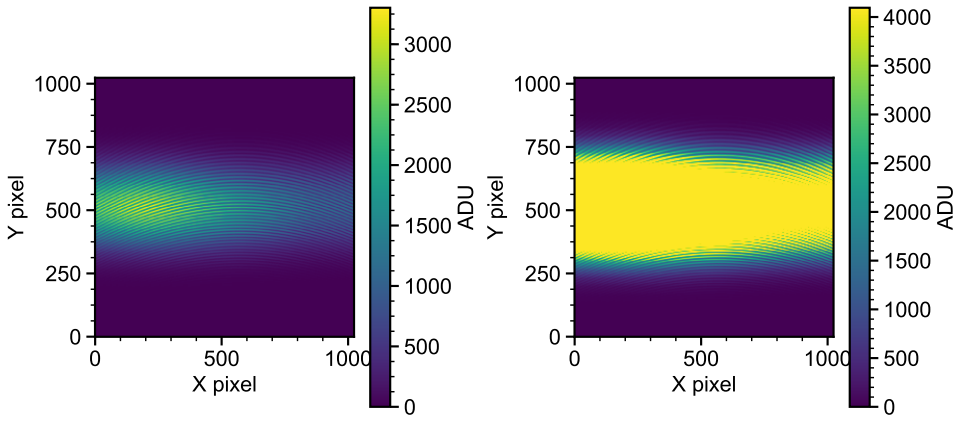

Figure 4.20: Right: Digitized synthetic measurement where the Photron 12bit ADC detector has saturated. Left: Accounting for imperfect transmission through the optical components, detector saturation can be avoided.

Fig. 4.21 shows synthetic measurements for a low powered, low field MAST plasma. An image with the interference pattern is shown with the FLC with its axis orientated to 45°. An estimation of the expected uncertainty due

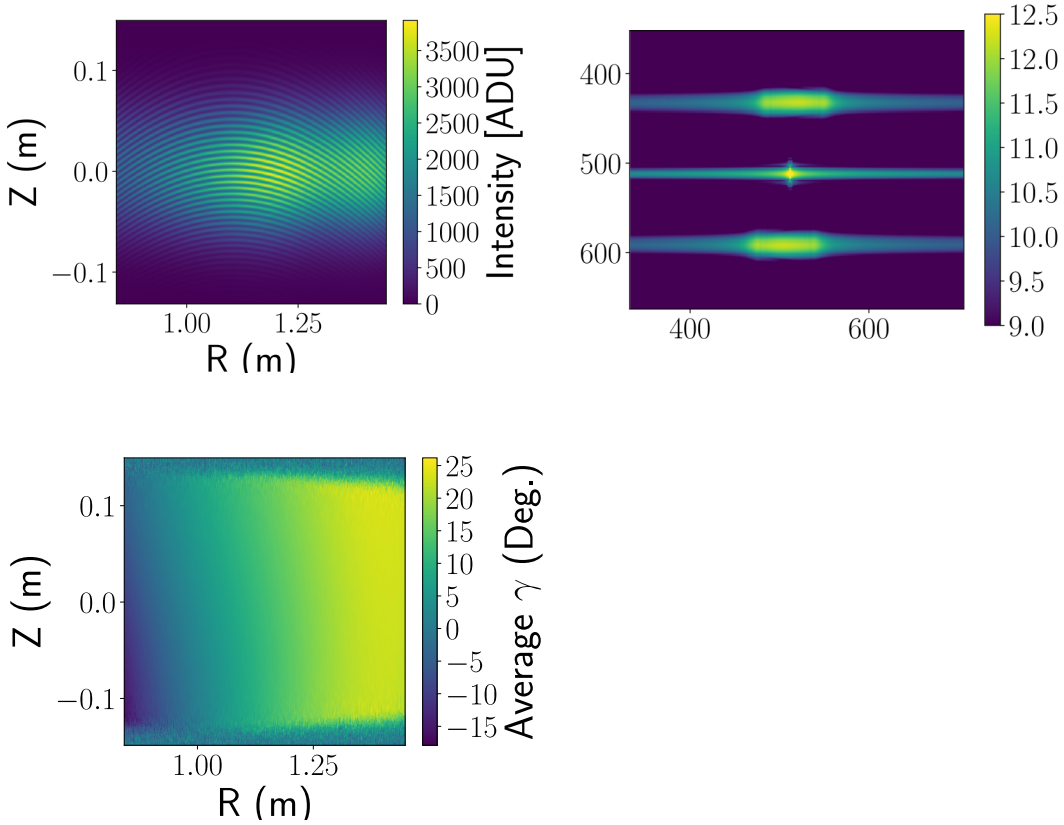

Figure 4.21: Forward modelled image digitized according to the camera specifications. The FLC axis is orientated of 45°. The Fourier transform power spectrum of the image, with the carrier frequency and DC frequency shown. A forward modelled image is produced in each of the FLC states and are demodulated to retrieve the 2D polarisation angle profile.

to dark noise and read noise were included using the methods outlined in section 4.4. The images were then digitized according the the sensitivity of the camera sensor. The standard deviation shown in Fig.4.22 in the measurement was found to be σ=±0.5° at 1ms exposure time. Whilst this is comparable to the uncertainty in the conventional MSE measurements, pixel binning could be used to reduce the uncertainty further.

4.6.2 MAST-Upgrade Scenarios

The MAST-U plasma equilibrium used within MSESIM were generated by the FIESTA equilibrium code[123], which calculates the plasma response to applied coil currents in the poloidal field coils. These FIESTA equilibrium were produced and provided by Dr. Andrew Thornton (CCFE). Fig. 4.23

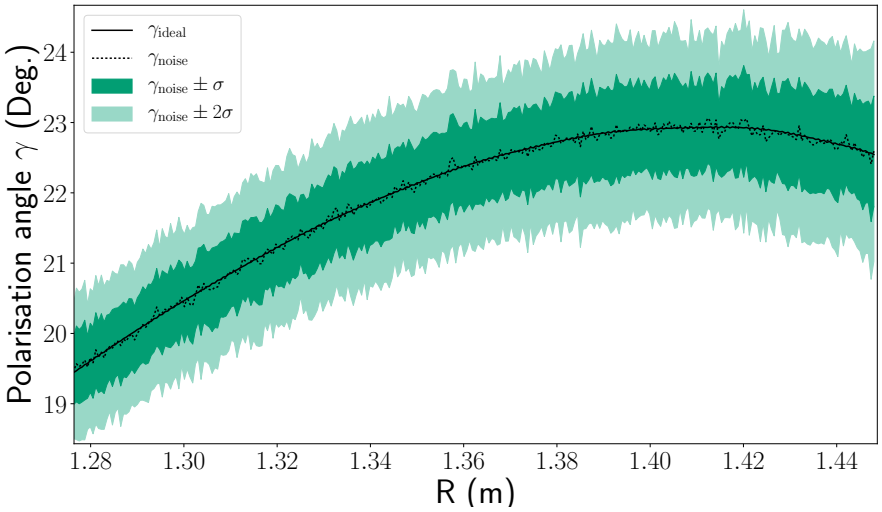

Figure 4.22: A 1D horizontal slice through the center of a noisy forward modelled image. 1σ and 2σ confidence intervals on the noisy polarisation angle profile are shown. This uncertainty could be reduced through longer exposure times or multiple frames.

shows the three plasma equilibrium normalised poloidal flux for the 'conventional', 'high elongation' and 'low elongation' plasmas. The first is a 'conventional' MAST-U plasma. MAST-U plasmas will have a lower inductance ($\ell_i = 0.6$) than in MAST to allow plasma shaping using the divertor coil currents and to generate the extended divertor leg configurations. Low inductance plasmas have less current in the plasma centre, and given that the q profile is inversely proportional to the current density, producing a reverse sheared q profile. This is the case for conventional tokamaks, however due to the naturally high elongation and plasma shaping in spherical tokamaks, there is a significant increase in the magnetic shear and increased q_{95}[124]. Driving current (eg. through neutral beam heating) acts to reduce the magnetic shear, but is counteracted by the naturally high magnetic shear of the spherical tokamak. Because of this, it is feasible to realise plasmas with monotonic q profiles with slightly hollow current profiles in STs, explaining the corresponding current density and q profiles plotted for each scenario in Fig. 4.25[125].

Initial MAST-U plasmas however will run at a lower toroidal field due to maximum current limits. Additionally the maximum available NBI heating power is 5MW for the initial campaign, which will increase to 10MW with

an additional off axis neutral beam system [27]. The k25 scenario is a high elongation plasma with 5MW of injected neutral beam power, more typical of the initial plasma scenarios in the first MAST-U campaign. We also compare the predicted diagnostic performance in these high powered, elongated plasmas to a low injected power 'MAST-like' plasma, with lower elongation and higher inductance, and therefore reverse sheared q profile, without a current peak at the plasma edge. The current, pressure and vertical and toroidal field profiles for these three scenarios are shown in Fig. 4.24.

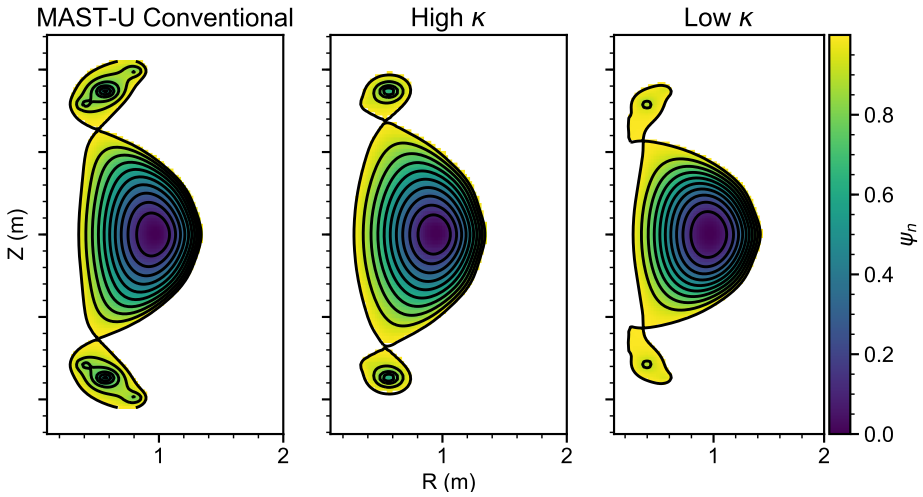

Figure 4.23: Normalised poloidal flux contours up to $\psi_n = 1$ for the three MAST-U plasma scenarios.

Fig. 4.26 shows the demodulated polarisation angle for each MAST-U scenario as a 1D radial profile taken from the center of the 2D profile. The uncertainty in the polarisation angle due to shot noise is $\delta\gamma < 0.2°$ in these plasma. This is due to modelling the neutral beam voltage at 70kV, rather than the typical ≈60kV beam voltage on MAST. There is a clear shift in the measured polarisation angle between the low κ scenario and the conventional plasma which has an edge current peak at the plasma edge. The diagnostic should comfortably resolve large variations in the current profile. When forward modelling these more structured current profiles compared to the smooth current profile case in the MAST plasma, it is evident that the resolution of the spectral model is introducing oscillations into the modelled profiles. Increasing the resolution of the MSESIM run used to generate the spectrum for the forward model is possible, however at significant computa-

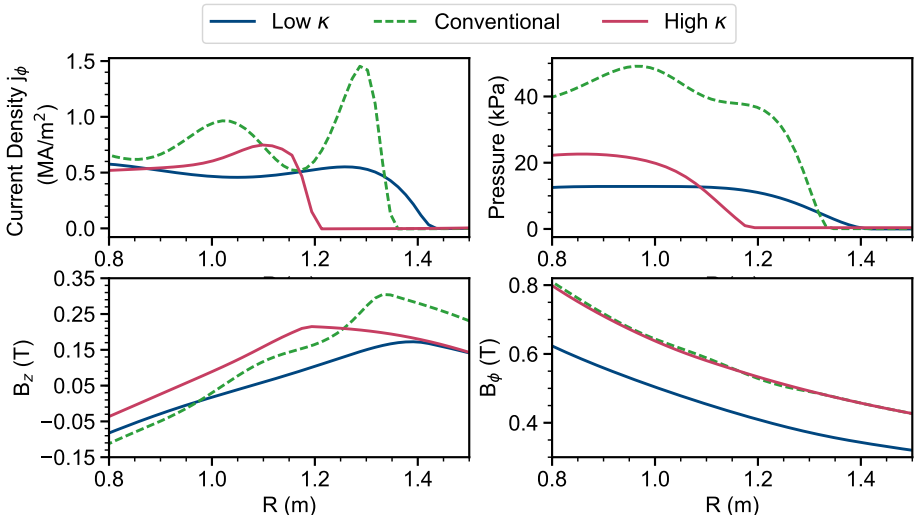

Figure 4.24: Top Left: Current density profiles for each MAST-U plasma. Top right: Electron pressure. Bottom Left: Mid-plane vertical field B_z profile. Bottom Right: Mid-plane toroidal field profile. Note that the high elongation and conventional scenarios employ the maximum toroidal field capabilities of MAST-U, with the low κ scenario toroidal field a more likely candidate for initial campaigns.

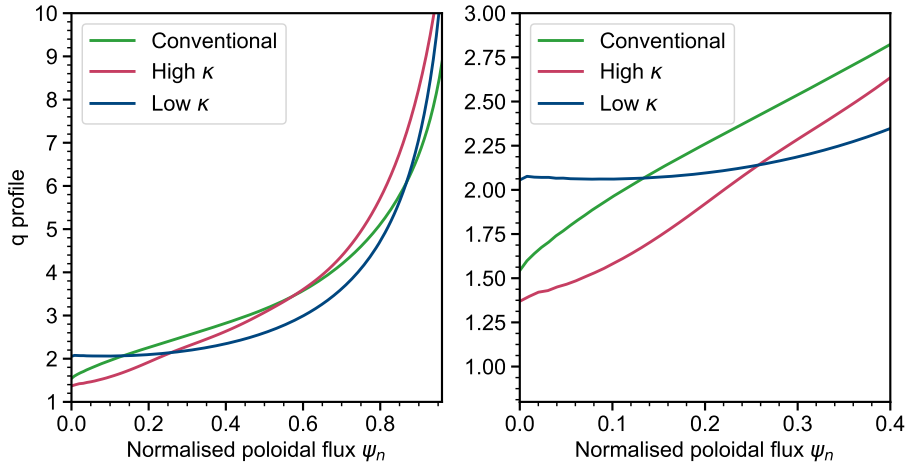

Figure 4.25: Safety factor profile as a function of normalised poloidal flux. The high κ and conventional scenarios have significantly increased to 6MW and assume full neutral beam heating capabilities (3-4 neutral beams), compared to 3MW heating (2 neutral beams) in the low κ mast-like plasma.

tional cost.

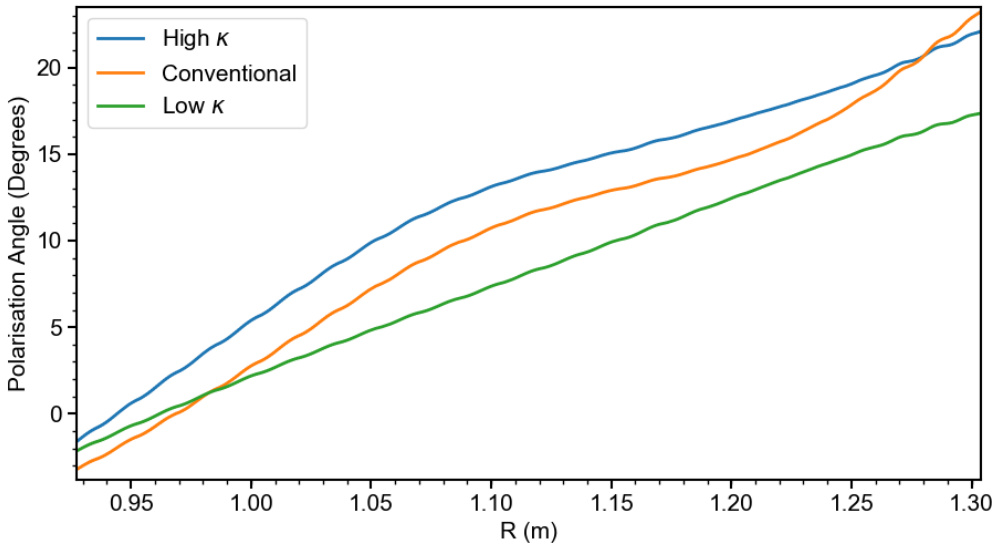

Figure 4.26: Polarisation angles forward modelled using the IMSE diagnostic design for the 'MAST-like' plasma with no edge current (green), large edge current 'conventional' MAST-U plasma (orange) and high elongation MAST-U plasma (blue).

4.7 Future Development

Further practical design work would be required to realise the full IMSE system for MAST-U. Considering the interferometer components, particularly for the delay and displacer plates, stress-free mounts are paramount to avoid stress induced birefringence in the crystals, which could lead to drifts in the measured polarisation angle. Other coherence imaging based systems have noted that temperature variability, which causes thermal expansion of the crystals and changing the applied delay leading to phase drifting, which can be avoided by using temperature controlled ovens [126].

The objective of first measurements with the IMSE system would be for reliable measurements, consistent with the equilibrium reconstruction, and proof of diagnostic principle on low field, spherical tokamaks. The existing MSE port on MAST-U HM-07A, which is the location assumed for the design work in this chapter, is the ideal place to put the system short term. The port is situated at the mid-plane, with good view of the neutral beam and lines of sight are mostly tangential to flux surfaces. The entire sector, including the MSE port is shown in Fig. 4.27.

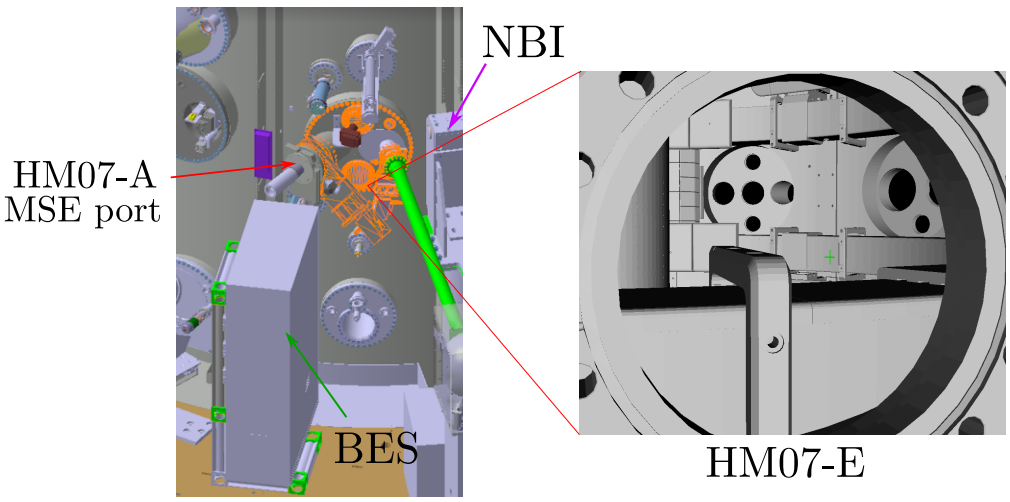

Figure 4.27: Left: CAD View of surrounding diagnostics and available ports in sector 7. Space is restricted by the beam emission spectroscopy (BES) diagnostic, however would be possible to floor mount the IMSE system either behind BES for HM-07A (the current MSE port) or HM07-E adjacent (right). HM07-E view is partially restricted by a magnetic field coil and support structure.

It would require removal of the conventional MSE system whilst IMSE measurements were taken. Another port HE-07E, adjacent to the conventional MSE port is available, however the view is partially restricted by a magnetic field (see Fig. 4.27). Consideration as to whether to the diagnostic should be machine mounted or floor fixed will be needed. Other coherence imaging systems found that vibrations from movement of the vessel during plasmas led to movement of the interferogram fringes due to relative movement between the interferometer components and the detector[121]. This could be particularly tricky for mounting the device at the mid plane. Alternatively the diagnostic could be mounted to a structure on the floor, limited only by space constraints within that particular sector.

Ideally a dedicated port for both the conventional system and IMSE system would be allocated to run both diagnostics simultaneously. This would be beneficial for diagnostic cross validation and could open up the opportunity for further measurements derived from both diagnostics, for example, measuring the radial electric field[86]. Unfortunately, due to the shift in the MAST-U

operational timeline it was infeasible to further the design for implementation of the diagnostic.

4.8 Conclusions

This chapter presented a forward model used to generate synthetic measurements of an imaging MSE diagnostic designed for MAST Upgrade. Using the spectral modelling code MSESIM, the MSE spectrum was modelled for for MAST and MAST-U plasmas, including considerations of line integration effects. This showed that, although the toroidal field strength is increased for MAST-U plasmas, spectral broadening is still significant, and the individual π and σ lines cannot be resolved.

A forward model of the IMSE system was developed to couple to MSESIM to optimise the diagnostic design and produce forward modelled synthetic measurements. Due to the low magnetic field on MAST-U, and hence small Stark splitting, thick interferometer waveplates are required to target the appropriate interferometric delay and maximise the fringe contrast. Including second order incidence angle effects in the model of the waveplates revealed that the fringe curvature would be severe at the edges of the sensor. The waveplate properties were then chosen to minimise this affect, by using a thick L=15mm delay plate and L=3mm displacer plate. Modelling of the synthetic images demonstrated that by using the field-widening technique for the delay plate, fringe curvature is reduced. A three cavity optical bandpass filter was optimised for the system to limit spectral contamination from half third energy components and nearby contaminant carbon lines.

A method to sample the noise characteristics of the detector was implemented, to estimate the uncertainty in the measured polarisation angle and provide an indicator of the diagnostic performance. At 2ms time resolution, assuming shot noise is the dominant source of uncertainty, the predicted polarisation angle uncertainty is expected to be $\delta\gamma/dR < 0.5^\circ$ in the MAST plasma used to design the diagnostic. Synthetic diagnostic images were presented which show the performance of the system in a range of typ-

ical MAST-U plasma scenarios. Comparing the polarisation angle profiles for the 'mast-like' plasma and conventional MAST-U scenario, there is an increase in the polarisation angle at the plasma edge attributed to the increased local current density.

Chapter 5

IMSE Measurements on the High Field Side of the DIII-D Tokamak

An imaging MSE (IMSE) diagnostic was deployed on the DIII-D tokamak for an experimental campaign in 2019. Measurements were made throughout various plasma scenarios. The diagnostic had a unique view on the high field side of the machine, which is rarely diagnosed with beam spectroscopy diagnostics. Within the optical system a ferro-electric liquid crystal (FLC) waveplate was replaced with a twisted nematic binary rotator waveplate. This enabled measurements of the polarisation angle which were consistent with the conventional MSE system in forward toroidal field plasmas. This chapter discusses the calibration of the polarimeter system and the consistency of the measurements with the conventional MSE system in different plasma scenarios. Some discrepancies between the inboard measured polarisation angle and the equilibrium reconstruction predicted angles arise at the plasma edge in reverse toroidal field plasmas, and potential explanations for this are explored. Finally, the outlook for the IMSE diagnostic and possible future measurements are explored.

Prior to the experimental campaign, the IMSE system was designed and developed by Dr Steve Allen (LLNL) and Dr Brian Victor (LLNL). The in-

dividual IMSE optical components calibrations were performed by the named collaborators and this data is presented in section 5.3.1. The analysis and interpretation of this data in section 5.3.1 was performed by the author of this thesis. Additional calibration procedures, presented in 5.3.2, were performed both by the thesis author alongside Dr Brian Victor and Dr Steve Allen. The calibration analysis, application to data presented in the thesis, and interpretation of the data rests with the thesis author. Data analysis was performed using the demodulation routines within the forward model written by the author and presented in Chapter 4. All additional data analysis and interpretation in section 5.5 are the work of the author of the thesis.

5.1 Motivation for high field side measurements

The high field side (HFS), or inboard region, of fusion tokamaks is poorly diagnosed due to access restrictions and lack of space for diagnostics much larger than magnetic probes along the vessel centre column. For spectroscopic diagnostics relying on neutral beam emission, HFS measurements can pose a challenge due to significant neutral beam attenuation, hence low available signal, towards the inboard side. Additionally the radial resolution is limited, as the neutral beam becomes more parallel to the flux surfaces. Deploying the IMSE diagnostic on the HFS of the machine provides a unique opportunity to measure the local vertical magnetic field across the entire plasma cross section, fully covered by the field of view of the conventional MSE diagnostic viewing the outboard low field side, and the imaging MSE system on the inboard high field side. These measurements, as described in Section 3.3, are used to constrain the equilibrium reconstruction code EFIT[53]. These measurements provide local constraint for the basis function ff' across the full radial extent of the plasma. If regions of the plasma flux surfaces are left without constraint, then equilibrium codes can resolve inconsistencies between diagnostic measurements by placing erroneous current in these poorly diagnosed regions. This leads to nonphysical current and pressure profiles, such as large spikes in the current profile over small length scales, or

negative core pressure. The question remains whether including these additional measurements leads to a significant change the reconstructed current and pressure profiles.

5.2 The DIII-D IMSE Polarimeter

5.2.1 Diagnostic Geometry

The diagnostic was situated at the 285° viewing port, observing beam emission from the 30° neutral beam line, which contains both a left and right source known as 30L and 30R in Fig. 5.1, with the IMSE sight lines intersecting both beam sources. In theory it is possible to determine the relative contributions to the measured polarisation angle from each beam source if they were to be fired simultaneously. However the accuracy depends on the source injection angles[127] and would require detailed modelling of the individual beam sources. Also, the spatial resolution of the polarimeter line of sight (LOS) is significantly worse for the 30L beam, as the injection angle leads to more radial than tangential LOS through the neutral beam. The 30L and 30R beams are operated at different beam voltages, 81keV and 75keV respectively, and are interleaved in time when operating. This minimises the contribution of emission overlap from the two sources at similar wavelengths disturbing either diagnostic. Conventional MSE measurements can be made using the 30L source and IMSE measurements using 30R at 20ms time intervals.

The 285° viewing port is restricted by RF shielding, shown in Fig. 5.2. The radial view of the diagnostic extends from R=1.0m to R=1.45m, encompassing from the center column to 15cm away from the magnetic axis position. The diagnostic field of view (FOV) is shown with respect to the poloidal flux contours of a DIII-D plasma in Fig. 5.1. An image taken through the IMSE port with backlighting of the vessel is shown in the right hand plot of Fig. 5.2. The front lens focal length of the IMSE system is set to the position of the 30R beam center line, and the FOV is shown as red square outline in the left plot of Fig. 5.2. An RF shield is visible within the FOV, which

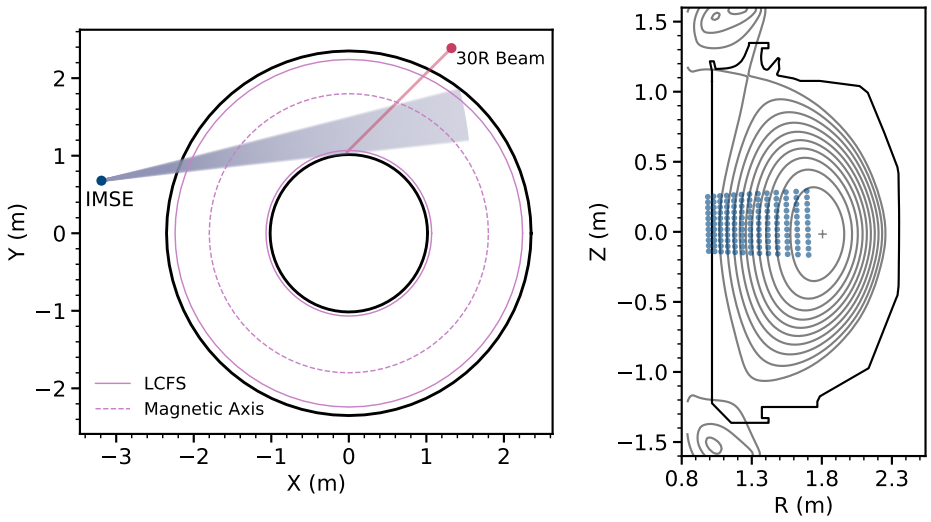

Figure 5.1: Left: Top down view in machine co-ordinates of the IMSE sight lines (light blue) intersecting with the 30R beam (red). Typical locations for the inner and outer LCFS are shown. The IMSE channels view past closed flux surfaces on the inboard side of the machine. Right: Poloidal plasma cross section, showing the poloidal flux contours ψ. IMSE pixels are binned into individual 'channels', and can be averaged along the vertical extent to provide a 1D radial measurement of the polarisation angle. IMSE channels (blue circles) towards the low field side are obstructed by the RF shield, the furthest view into the plasma extends to R=1.45m.

vignettes the image and limits the maximum radial extent to R≈1.45m. Although it was not expected that the RF shield shadow would disrupt the phase encoding, sharp changes in image brightness around the edges of the RF shield could lead to ringing artifacts in the demodulated polarisation angle.

A spatial map of the polarimeter FOV was generated by fitting to the positions of distinct vessel features such as sharp wall tile edges seen in Fig. 5.2 during a disruption event, to the pixel position on the CCD sensor. The spatial mapping was calculated and provided by Bill Meyer (LLNL). This map is produced between the pixel co-ordinates and (R,Z) location in the machine, shown in Fig. 5.1 within the poloidal plane. There is some small uncertainty in the pixel mapping, potentially due to minor movements of the optics relative to the machine during operation which may occur as the polarimeter is floor mounted rather than attached to the vessel.

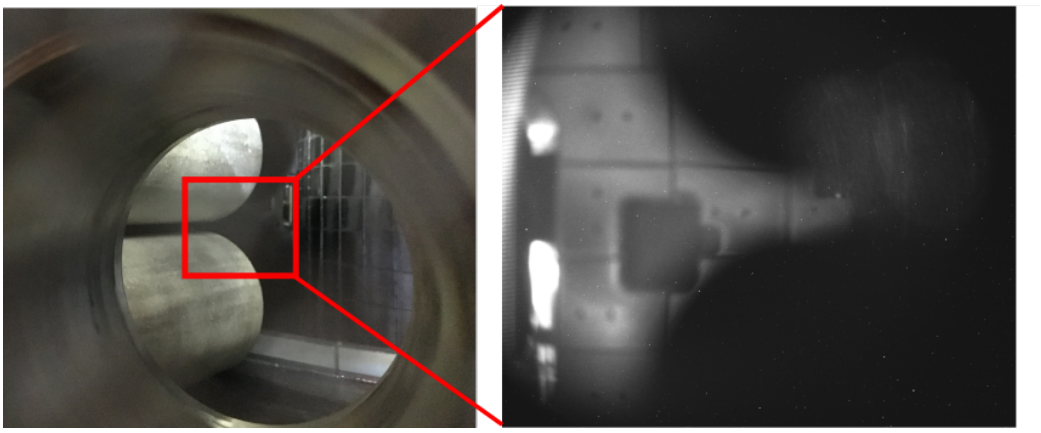

Figure 5.2: Left: Image taken close up to the 285° port using a general camera, with the viewing region for the IMSE system shown in the red square. Right: The region imaged by the diagnostic. The view is partially obstructed by the RF shielding, which produces a horn shaped shadow in the image that unfortunately inhibits measurements towards the magnetic axis.

5.2.2 Polarimeter Components

The DIII-D IMSE system employs the temporally switched single spatial heterodyne (TSSSH) technique, as outlined in section 2.4.2. An image of the polarimeter setup at the side of the tokamak is shown in Fig. 5.3. A three lens system is utilised, as is typical on coherence imaging based systems, which allows the light to be fully collimated through the polarimeter components with flexibility in the focal point in the plasma. Full details of the optical components can be found in Table. 5.1.

In previous IMSE measurements made on DIII-D a ferro-electric crystal (FLC) waveplate was used for phase modulation [49]. This liquid crystal waveplate switches the orientation of the liquid crystal molecules such that its fast axis orientation switches by 45° in $\approx 10\mu$s, enabling high temporal resolution measurements. Thorman [49] showed that these devices can exhibit spatial non-uniformity in the applied delay, meaning the diagnostic calibration is particularly sensitive to the illumination of the ray paths through the optical system. To overcome this issue the calibration light source and integrating sphere must be placed inside the vessel at the position of the neutral beam emission, to illuminate and fill the optical components in precisely the same manner as would be expected during a plasma discharge, but an in-situ

Component	**Manufacturer**	**Description**
Camera	pco.	pco.edge 5.5 sCMOS camera 2560x2160 pixels, Dynamic range: 16 bit Pixel size: 6.5μm square Max frame rate: 100 fps with rolling shutter Quantum Efficiency: $\approx$ 60% at 650nm
Polariser		
Quarter waveplate		
Bandpass Filter	Alluxa	OD5 Bandpass Filter $\lambda_{\text{cwl}} = 651.3\text{nm}$ $\lambda_{\text{FWHM}} = 1.89\text{nm}$ $n_* = 1.85$
Twisted Nematic Binary Rotator	Meadowlark Optics	LTN - 200 - λ Optical quality synthetic fused silica Diameter: 50.8 mm Clear aperture: 17.8 mm Thickness: 19.05 mm IR wavelength range: 600 - 950nm
Lens l_1 Lens l_2 Lens l_3	Zeiss Nikon Nikon	Telephoto f=135mm lens, f/2.8 F mount $f = 85\text{mm}$ $f/1.4$ F mount $f = 85\text{mm}$ $f/1.4$ F mount
α-BBO Displacer Plate	United crystals Inc.	40mm diameter L = 5.8mm, Optic axis cut angle Θ=30° no AR coating

Table 5.1: Summary of components in the DIII-D IMSE diagnostic. The orientation and delay of the binary rotator was calibrated using the technique outlined in 5.3.1.

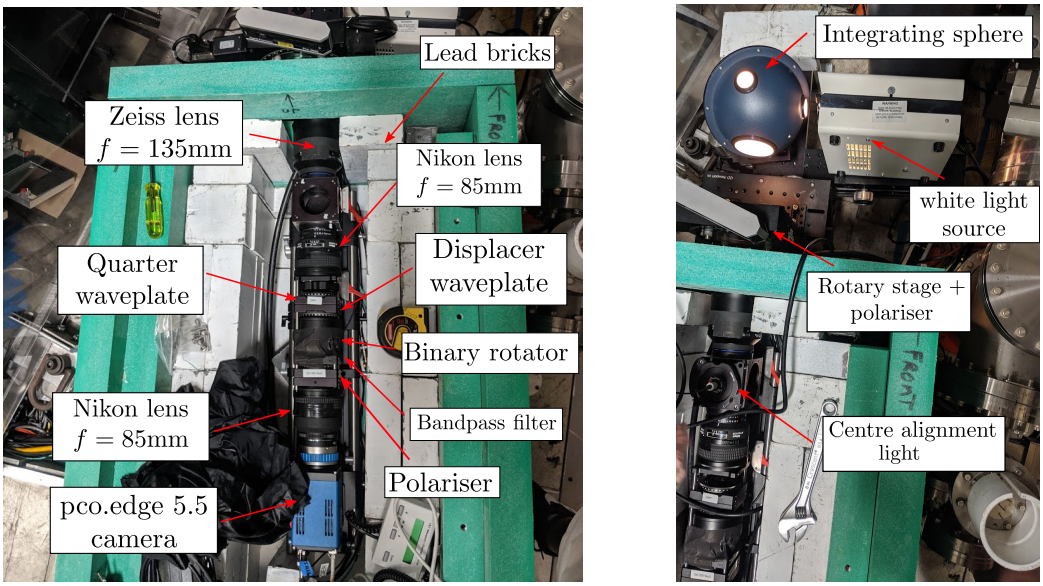

Figure 5.3: **Left:** DIII-D IMSE polarimeter setup with individual components annotated. The polarimeter was shielded with lead bricks to mitigate neutron damage of the camera sensor and optics. **Right:** Calibration setup at the side of the vessel. A broadband white light source filtered using a narrowband optical filter with λ_{cwl}=651nm, was coupled into an integrating sphere with a rotating polariser.

calibration requires significant vessel opening and access. Instead, procuring an alternative switching waveplate with uniform delay could improve the measurement reliability without requiring an in-situ calibration.

For the DIII-D IMSE polarimeter discussed in this chapter, the FLC was replaced with a twisted nematic liquid crystal (TNLC) binary rotator. Binary rotators act in one state to rotate linearly polarised light along the director of a layer of twisted liquid crystal molecules. In a second state zero rotation is applied. The effective outcome is the same whether an FLC or TN LC device is used, both acting as a switching half waveplate. The mechanism for the FLC relies on the LC molecules possessing a spontaneous polarisation which interacts with the electric field, and switches the fast axis orientation between the two states by 45°. In contrast the TNLC devices rely on the relaxation of the twist angle of the TNLC layer to produce a 90° rotation of incident linearly polarised light. The switching response time of a TNLC device therefore is much longer (t∼60ms) than FLCs, which limits the temporal resolution of the polarimeter. These longer timescales for switching

between states however are required to provide enough time for the LC twist angle to relax and contract fully and apply the required delay.

5.3 Diagnostic Calibration

This section includes discussion of the calibration of the polarimeter. Calibration measurements of the twisted nematic binary rotator switching waveplate in section 5.3.1 were undertaken prior to the campaign, in the laboratory by Dr Steve Allen and Dr Brian Victor. The full polarimeter calibration was performed by the author and named collaborators at the side of the DIII-D tokamak.

5.3.1 Characterisation of the binary rotator

The optical properties of uniformly twisted nematic liquid crystals (LC) have been studied for many applications, including LCD displays and holography[128–130]. A simple model of a twisted nematic liquid crystal layer uses the Mueller matrix for a uni-axial retarder and polarisation rotator,

$$\mathbf{M}_{\mathrm{TNLC}}(\rho,\phi) = \begin{pmatrix} 1 & 0 & 0 & 0 \\ 0 & \cos 2\rho & \sin 2\rho & 0 \\ 0 & -\sin 2\rho & \cos 2\rho & 0 \\ 0 & 0 & 0 & 1 \end{pmatrix} \cdot \begin{pmatrix} 1 & 0 & 0 & 0 \\ 0 & 1 & 0 & 0 \\ 0 & 0 & \cos\phi & \sin\phi \\ 0 & 0 & -\sin\phi & \cos\phi \end{pmatrix} \quad (5.1)$$

where ϕ is the delay applied by the rotator and ρ is the orientation of the optic axis of the LC layer[128, 131]. The orientation of the TNLC layer in the binary rotator is shown for in Fig. 5.4. The molecule orientation in the LC layer is twisted through 90°.

In the 'off' state (ie. zero applied voltage) of the rotator S_-, incident linearly polarised light follows the optic axis of the twisted LC layer as the incident ray passes through the cell, a process known as '*adiabatic following*'. Upon exiting the TNLC, incident light has been rotated by 90°.

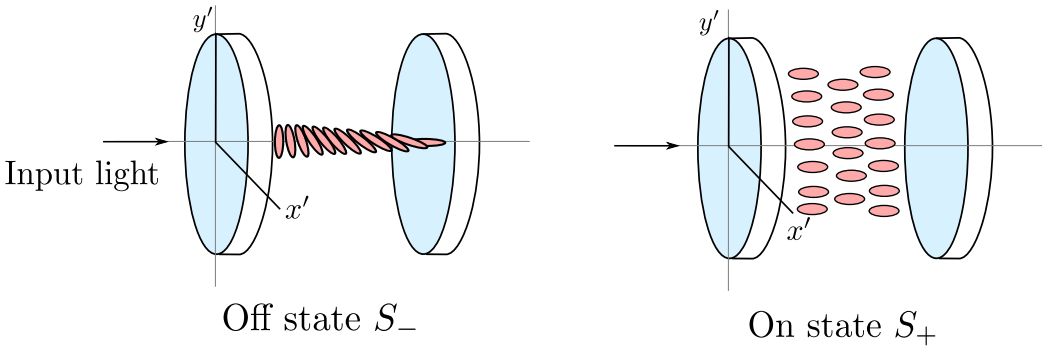

Figure 5.4: Simplified diagram of the twisted nematic liquid crystal layer. With zero voltage applied S_-, the liquid crystal layer is twisted such that input linearly polarised light experiences a 90° rotation. When voltage is applied, in the S_+ state, the LC layer stretches such that the input light is unaffected.

In the 'on' state S_+ (ie. where voltage is applied), the TNLC layer stretches, aligning parallel to the applied electric field. In this state incident polarised light remains unchanged on exiting the TNLC layer.

The transmission intensity of the output light was measured as a function of input polarisation angle θ by placing the binary rotator between a rotating polariser and a fixed polariser at an orientation angle of 45°, as shown in the schematic Fig. 5.5. A theoretical model was fitted to the measured transmission intensity curves to extract the applied delay in each state of the rotator, for each pixel location across the aperture of the rotator. It is assumed that the binary rotator operates ideally, such that in the S_+ state the output intensity should be equivalent to two crossed polarisers, and in the off S_- state the binary rotator acts as a uni-axial waveplate with an optic axis orientation to be determined. For the on state, denoted by S_+, the light intensity is given by,

$$S_+ = \frac{I_0}{2}(1 + \sin(2(a - \gamma))) \tag{5.2}$$

where γ is the input polariser angle and a is the relative offset between the fixed and rotating polariser. In the S_+ state then $\rho = 0$. In the off state the output intensity, denoted by S_-, is given by,

$$S_{-} = \frac{I_0}{4}(2+2\cos(2\rho)\cos(\phi)\sin(2(a-\gamma+\rho))+\sin(2(a-\gamma+2\rho))-\sin(2(a-\gamma))), \tag{5.3}$$

where ρ is the optic axis orientation and ϕ is the retardance applied by the rotator. Misalignment of the optical components can be accounted for by including ρ, ϕ as free parameters in the fitting function. Mueller matrix analysis of the entire polarimeter can be performed if the values of ρ and ϕ are calculated for each optical component. Then a model of the polarimeter output can be constructed, including the exact orientation and retardance of each component, to model the polarimeter data and account for any systematic offsets which may be present in the data.

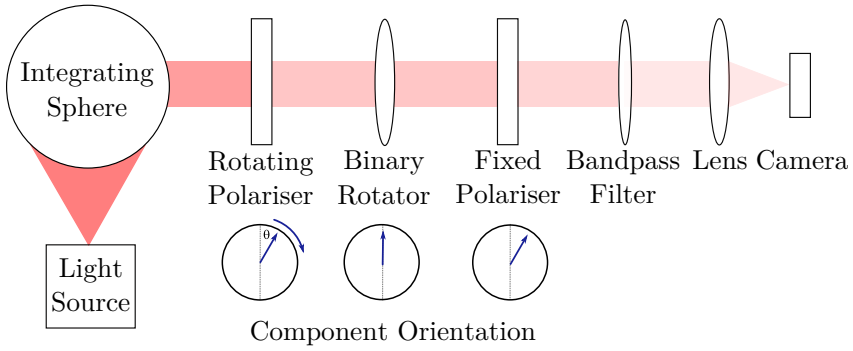

Figure 5.5: Optical setup for calibration of the binary rotator switching waveplate. An integrating sphere is fed using a halogen lamp and provides a uniform light source, which passes through a polariser placed on a rotary stage, followed by the component to be calibrated (in this case the binary rotator) and a measuring polariser at a fixed angle. The bandpass filter used in the polarimeter setup was used with specifications from Table 5.1.

Fig. 5.7 shows the transmission intensity profile as a function of polariser orientation, for each state of the binary rotator. As a background image was not taken with this dataset, a dark frame taken from the initial exposures of a plasma discharge was used to estimate the number of background counts which were then subtracted. When fitting of the theoretical transmission curves, a background offset should not be a free parameter in the fit, because

any deviation of the transmission curves from full extinction is an indication that the phase shift of the binary rotator is non-ideal. The reduction in transmission intensity for off axis pixels, particularly those close to the extreme edges of the image is likely due to to lens vignetting, rather than non-uniformities within the binary rotator. The transmission intensity across the rotator aperture in both states is shown in Fig. 5.6, then the intensity of a central and edge pixel is shown as a function of the input polarisation angle in Fig. 5.7.

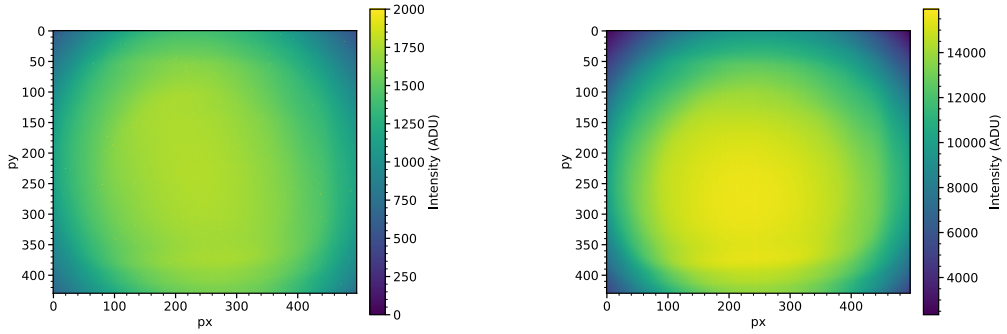

Figure 5.6: Transmission intensity across the rotator aperture for the switched (left) and unswitched (right) state, with the rotating polariser at $\theta = 0°$. Darker regions in the extremities of the image indicate the lens aperture.

Fitting equations 5.2 and 5.3 to the intensity curves extracts the offset angle a between the initial and final polarisers, the orientation of the optic axis of the binary rotator ρ and the applied delay ϕ. Fig. 5.8 shows the fitted offset between the two fixed polarisers, and the delay applied by the binary rotator across its aperture. We also should note that this dataset was taken with the binary rotator in the collimated region, which precludes commenting on the surface position dependence of the delay. To achieve this, additional measurements must be made whereby the lens is set to focus the sensor image onto the surface of the rotator such that each pixel on the detector then corresponds to a spatial location on the binary rotator[49].

Ideally the applied retardance should be constant across the rotator aperture, and be at the specified value of ϕ= 180°, but the fitted retardance is on average 191.3°. From Fig.5.8, it is clear to see that the delay depends on the range of incidence angles through the rotator. The slight linear ramp

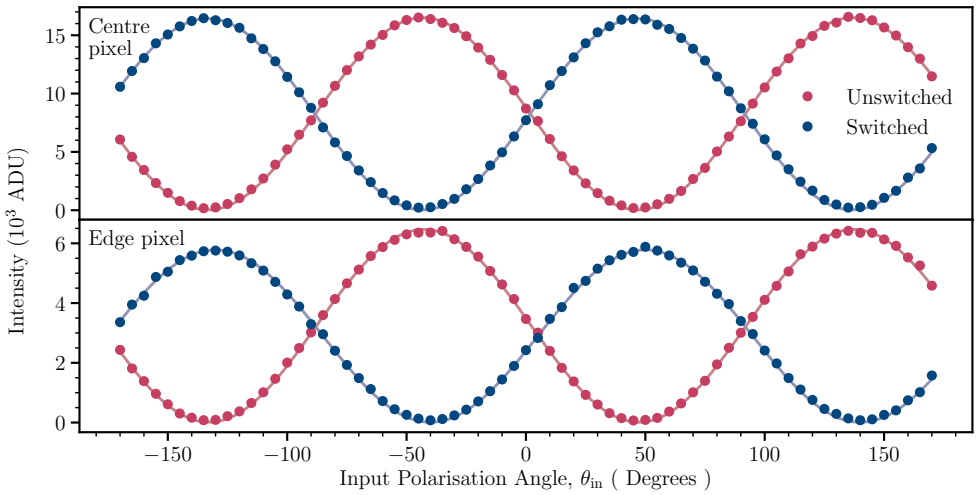

Figure 5.7: **Top**: Transmission intensity curves from the center pixel for the switched and unswitched binary rotator states. Images were taken whilst rotating the rotary stage polariser in increments of 5°. The symmetry of the crossing point of the two curves shows that switching between the two states of the binary rotator is ideal at the center of the image. The measured transmission intensity is fit to equations 5.2 and 5.3 using least squares regression, and the resulting fit is shown (solid lines).
Bottom: Measured and fitted transmission intensity curve for a pixel towards the edge of the camera sensor.

in the delay likely means that the optic axis of the rotator is not exactly parallel to the surface, and so the rotator acts like a weak displacer in the unswitched state. Similar behaviour has previously been observed in liquid crystal variable retarders [80]. One of the advantages to the binary rotators over other liquid crystal devices such as the FLCs is the ability to change the applied voltage in the switched and unswitched states to ensure the switch between the two states is close to a half wave delay. Therefore, future calibration of the binary rotator should include a scan of the applied voltages whilst measuring the surface position delay dependence by placing the rotator in the focal plane of the camera lens.

Due to this displacer-like behaviour, it may not fully valid to model the TNLC waveplate with a combination of rotation and waveplate Mueller matrices without considering including an optic axis angle Θ. Fitting to the intensity curves for off axis pixels was much more difficult without imposing restrictive bounds on the free parameters ρ, ϕ in equation 5.3, which implies that non-axial rays may need to be considered. The LC twisted layer in fact includes

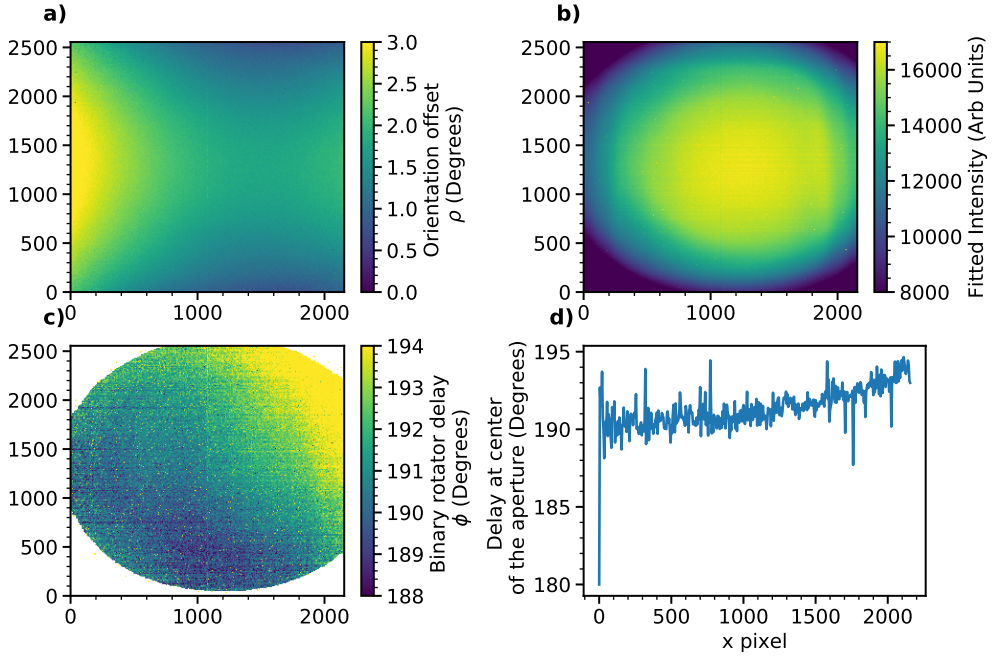

Figure 5.8: **a)** Fitted orientation angle offset. **b)** Fitted transmitted intensity across the rotator aperture in the off (S_) state. **c)** Delay applied by the binary rotator in state S_-. **d)** Delay across the centre of the aperture. Note that the fitted applied retardance average is $\phi = 191.3°$, which is $11°$ more than the specified $180°$. Note that the uniformity of the retardance (albeit higher than anticipated) is within $\pm 3°$ of the mean value across the aperture.

N molecule layers and each should be modelled as an individual waveplate with the optic axis at an angle within the plane of the waveplate ρ_j. The Stokes vector of light exiting the N-1 layer then is,

$$S_0 = \prod_{j=1}^{N-1} \left[M_{\text{rot}}(\rho_j) \cdot M_{\text{retarder}}(\Gamma_j) \cdot M_{\text{rot}}^{-1}(\rho_j) \right] \cdot S_i \tag{5.4}$$

where Γ_j is the retardance imposed by the jth layer, and is given by equation 2.30 [79]. This multiplication would need to be performed computationally with given knowledge of the LC layer properties to find an exact Mueller matrix for the specific binary rotator. An alternative, more comprehensive treatment would be achieved using the Berreman method [128], where the electric field components of the transmitted and reflected light is calculated for every interface in the LC layer, which could be achieved with an optical ray tracing code which preserves polarisation information. This would allow

for full characterisation of non-axial rays within a liquid crystal layer.

5.3.2 Polarimeter Calibration

The response of the IMSE polarimeter to incident linearly polarised light of known polarisation angle was measured experimentally using the optical arrangement shown in Fig. 5.5, with the additional lenses and waveplates described in Table 5.1 included between the rotating and fixed polarisers. The polarimeter response to the input polarisation angle γ_{in} is calculated by filling the optics using a broadband halogen lamp coupled into an integrating sphere, with an optical bandpass filter with central wavelength $\lambda = 651\text{nm}$.

To reiterate, when integrated over the MSE spectrum the light intensity measured by the polarimeter in each state of the binary rotator is,

$$\begin{aligned} S_+ &= \frac{I_0}{2}\left(1 + \zeta \sin\left(\phi_0(y) + 2\gamma + 4g(\gamma)\right)\right) \\ S_- &= \frac{I_0}{2}\left(1 + \zeta \sin\left(\phi_0(y) - 2\gamma + 4h(\gamma)\right)\right) \end{aligned} \tag{5.5}$$

where ζ is the fringe contrast, $g(\gamma)$ and $h(\gamma)$ are the phase offsets in each state due to minor misalignment of optical components and other non-ideal effects within the polarimeter, γ is the input polarisation angle and $\phi_0(y)$ the retardance imposed by waveplates within the polarimeter system. Then, the polarisation angle measured by the polarimeter is found from the phase difference Δp of the interferogram fringes imaged with the binary rotator switching state,

$$\begin{aligned} \Delta p &= \left(\phi_0(y) + 2\gamma + 4g(\gamma)\right) - \left(\phi_0(y) - 2\gamma + 4h(\gamma)\right) \\ \Delta p &= 4(\gamma + g(\gamma) - h(\gamma)) \end{aligned} \tag{5.6}$$

For an ideal polarimeter the response to input linearly polarised light was expected to be linear (ie. γ_{out} measured by the polarimeter equal to the input polarisation angle γ_{in} on the rotary stage). The linear response parameter m and the angle offset c were found by fitting the function $\gamma_{\text{out}} = m{*}\gamma_{\text{in}}{+}c$ to the demodulated polarisation angle for each input polarisation angle (between -20° and 20° across the vertical axis of the polariser), as shown for the central pixel in Fig. 5.9.

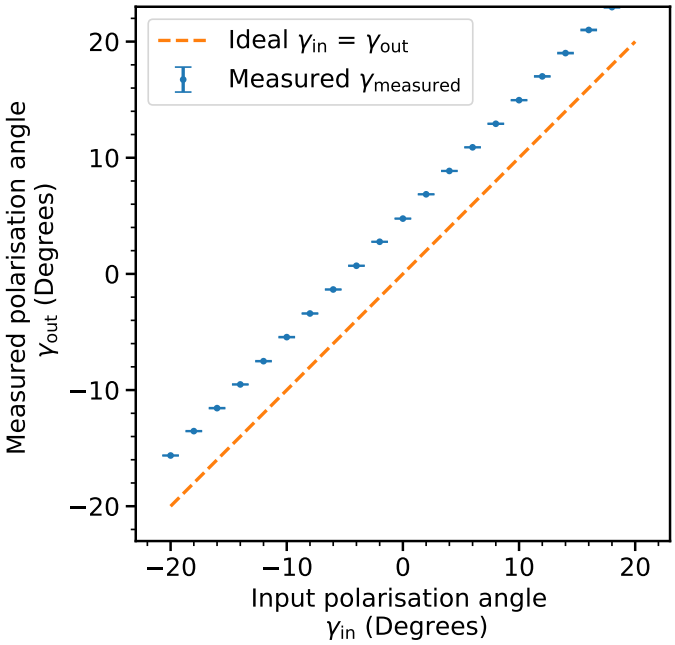

Figure 5.9: Demodulated polarisation angle γ as a function of input polarisation angle on the rotary stage. The range of input angles is approximately the range of polarisation angles measured during forward or reverse toroidal field plasmas.

Fig 5.10 shows the measured linear response and polarisation angle offset as a function of pixel position on the sensor. The response exhibits some non-linearity at the extreme edges of the image, which could be due to incident light having larger oblique incidence angles at the corners of the camera sensor. IMSE systems which include a switching waveplate have previously attributed non-linear behaviour to the non-uniformity in the switching waveplate[49]. The average offset across the aperture was measured to be 4.3°. Generally absolute offsets relative to the input angle indicate additional polarisation rotation within the optical system; either caused minor misalignment of an optical component or additional rotation by either the switching waveplate or quarter waveplate. The polarisation angle offset $g - h$ varies by 0.2° across the centre of the sensor when rotating the input polarisation angle by 90°, either across the vertical or horizontal axes of the rotating polariser. The cause for this remains unclear, though minor deviations in the surface quality of α-BBO waveplates could change the reflected and transmitted components of the incident light linearly polarised parallel

or perpendicular to the optic axis.

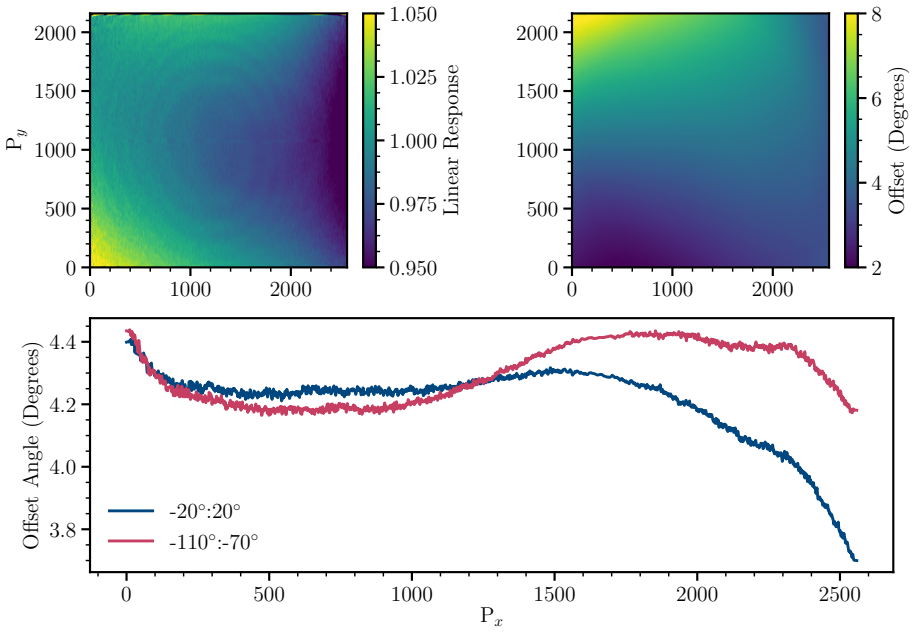

Figure 5.10: **Top Left:** The polarimeter has some non-linear response to incident light at the extreme edges of the sensor. **Top Right:** Offset polarisation angle calculated for incident polarised light between -20° and 20° on the rotating polariser. **Bottom:** Measured polarisation angle offset measured along the horizontal axis of the detector. There is a distinct change in the measured offset when rotating the polariser by 90°, but the cause of this is not well understood.

Calibration of the instrument phase

Aside from the polarisation information retained within the fringe pattern, it is also possible to obtain information on the 'instrument' phase ϕ_0 using the sum of the interferogram phases. The instrument phase includes any contributions to the spatial carrier due to birefringent waveplates in the optical system. When viewing plasma emission, the instrument phase depends on the range of Doppler shifted wavelengths of the MSE emission. The measured instrument phase $\phi_0 = \phi_c + \phi_d$, where ϕ_c is a measure of the instrument phase using a calibration source, such as a lab light source at the rest wavelength, and ϕ_d the additional phase contribution due to the Doppler shift of the emission lines. Naturally since the Doppler shift is set

by the beam velocity and view geometry, the Doppler contribution to the instrument phase provides information on the spatial distribution of the beam velocity and the beam divergence provided that the view geometry is well known. For IMSE polarimeters using the switching waveplate for phase modulation, it is assumed that the instrument phase remains constant between two successive frames taken around the same time period. If the instrument phase is measured to remain constant throughout periods of the discharge, this would open the possibility to switching the rotator less frequently and increase the polarimeter temporal resolution.

The calibration instrument phase ϕ_c was retrieved from the polarimeter calibration data using the sum of the interferogram phases, for each input polarisation angle on the rotary stage. Fig. 5.11 shows the variation in the instrument phase $\Delta\phi_c$ relative to the first set of calibration images which in total were taken over the course of around an hour. The instrument phase was shown to drift by up to half a wave over the course of the calibration time. The instrument phase is not a function of the input polarisation angle, however the properties of the crystals are known to vary with temperature [121, 132]. Ambient temperature variation at the side of the tokamak throughout the time taken to complete the calibration, or over a day of plasma discharges, would lead to small changes in the thermal expansion coefficients for the α-BBO displacer plate, leading to a shift in the refractive indices and therefore a drift in the instrument phase over time. On the timescales of interest for polarisation angle measurements, variation in the instrument phase between successive exposures is negligible. However for retrieving the Doppler phase from the images, if the instrument phase derived from the calibration is significantly different to the instrument phase measured in the plasmas then this can lead to phase jumps in the derived Doppler phase. Later in section 5.5.3 we see that additional spectral effects can hinder the measurement of the Doppler phase in real plasma measurements. In coherence imaging flow systems, this issue is compensated for by obtaining the instrument phase prior to each plasma discharge using a tunable laser source and placing waveplates within temperature stabilisation ovens[126].

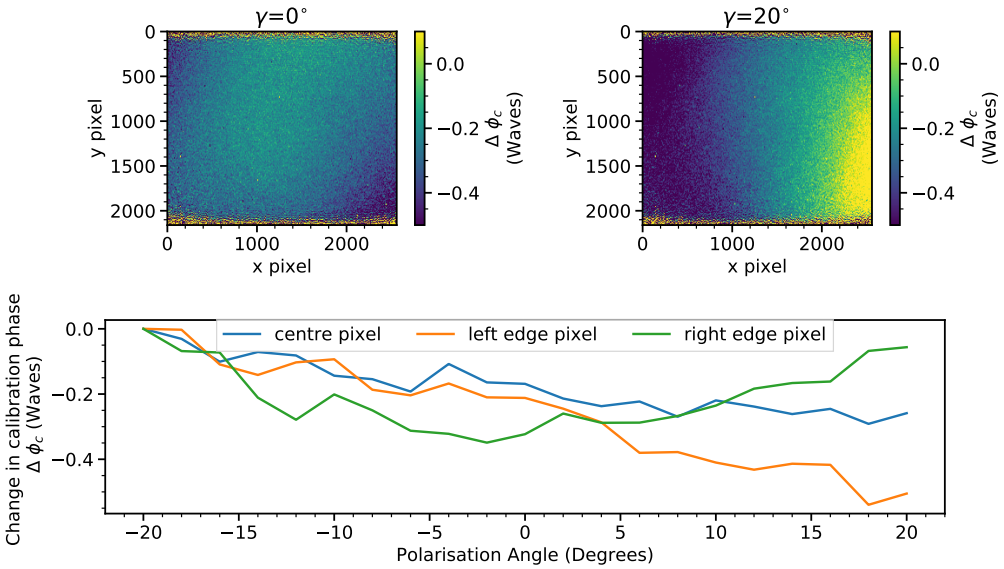

Figure 5.11: Top left: Variation in the instrument phase ϕ_c measured with input polarisation angle $\gamma = 0$ relative to the instrument phase measured in the first calibration images. Top right: Change in the instrument phase between the first and final calibration images. Spatial variation in ϕ_c is observed. Bottom: Variation in the calibration phase relative to the first calibration images at the centre of the image (blue), and for pixels at the extreme left (orange) and right (green) of the image.

5.3.3 Calibration Summary

The IMSE polarimeter calibration for measurements of the polarisation angle can be summarised as follows. The 'true' polarisation angle is retrieved by calculating,

$$\gamma_\sigma = \frac{\Delta p}{4} + [g(\gamma) - h(\gamma)] + \frac{\Delta\gamma}{\Delta B_\phi} B_\phi + \theta_{\text{pol}} - \frac{\Delta\gamma}{\Delta E_r} E_r \tag{5.7}$$

where $\Delta p/4$ is the phase difference between the interferograms produced in each state of the binary rotator and [$g(\gamma)$ - $h(\gamma)$] is the offset angle measured using the integrating sphere in section 5.3.2. A small constant angle offset is included due to the slight angle of the rotating polariser stand at the vessel relative to the polarimeter. This was measured using a digital spirit level, and was measured to be $\theta_{\text{pol}} = 0.42°$. To measure the absolute polarisation offset, an additional calibration would be required using a source with well known polarisation angle (for example using a laser diode), however this was

not performed here. The term $\frac{\Delta\gamma}{\Delta B_\phi}$ is the ratio of the polarisation angle rotation due to the Faraday effect in the port window, induced by variation in the magnetic field across the polarimeter field of view. Finally, the term $\frac{\Delta\gamma}{\Delta E_r}$ is the ratio of the polarisation angle variation due to the radial electric field E_r. These two final terms are discussed in further detail in section 5.5.

5.4 Data Analysis

In this section the demodulation python routine written to retrieve the polarisation angle from the measured interferogram is outlined. This is built upon the routine used to demodulate the modelled IMSE images for Chapter 4, with adaptations for complications in using real data. This includes: hot pixels, statistical noise and ensuring the window function extracts the carrier and DC frequencies without Gibbs phenomenon, which are ringing artifacts present in a filtered signal due to the finite impulse response of the signal filter. The signal availability across different plasma scenarios is discussed, and finally develop a routine to estimate the measurement uncertainty in the polarisation angle by understanding the noise in the interferogram phase.

5.4.1 Demodulation routine

To retrieve the polarisation information from each image, the interferogram must be demodulated to find the phase and amplitude of the carrier wave. The demodulation routine is shown pictorially in Fig. 5.12. Even with additional neutron shielding in the form of surrounding lead blocks, neutrons still contribute to a significant number of hot pixels, which vary from frame to frame. This salt and pepper noise is removed by using a 2D median filter of width 13 pixels horizontally, and 3 pixels vertically, across the raw interferogram. The filter kernel width was kept as possible to avoid over-smoothing the data. Additionally, a windowed Hanning filter is applied to the raw images to avoid ringing in the demodulated polarisation angle at the edge of the image. The interferogram signal in each frame is given by,

$$S_{\pm} = \frac{I_0}{2}(1 + \zeta \cos(\phi(y) \pm 2\gamma) \tag{5.8}$$

where γ is the polarisation angle of incident light, $\zeta(x, y, \lambda)$ is the fringe contrast, and $\phi(y, \lambda)$ is fringe phase. A 2D Fourier transform is performed, and the carrier f_c and DC f_{DC} frequencies are extracted using a 2D Tukey window function in the Fourier domain. Various window functions with different roll off properties, were trialled to ensure the level of noise carried through via filtering was minimised. There is a low spatial frequency present in the horizontal component k_x which can be attributed to curvature of the fringes at the edge of the image. The shape of the RF shield shadow leaves a sharp signal to noise boundary in the real image, as seen in Fig. 5.12, which may also contribute to some additional spurious frequencies in the Fourier domain. The difference between the phase of the carrier frequency in successive interferograms retrieves the polarisation angle, and the contrast is calculated using the ratio of the amplitude of the spatial carrier and the DC amplitude. The fringe contrast is a useful quantity to calculate as it informs the signal level available within the image, and is used to mask out regions of low signal within the 2D polarisation angle profile.

5.4.2 Signal availability

One of the main challenges of measuring beam emission from the high field side is the signal level. At high core plasma densities the fast injected neutrals cannot penetrate as deeply within the plasma, due to neutral beam attenuation, causing a reduction in beam emission intensity and polarised Stark emission. Normally the neutral beams are only fired into high enough density such that the beam is fully attenuated before reaching the inner wall of the machine, to protect the tiles and centre column on the inner wall from beam shine through. In some plasmas however the density was so high that the interferogram fringes were not present in the image, suggesting that the beam emission from the 30R beam no longer penetrates to the inboard side (see Fig. 5.25 in section 5.5.2.)

Fig. 5.13 shows the variation in the interferogram fringe contrast as a func-

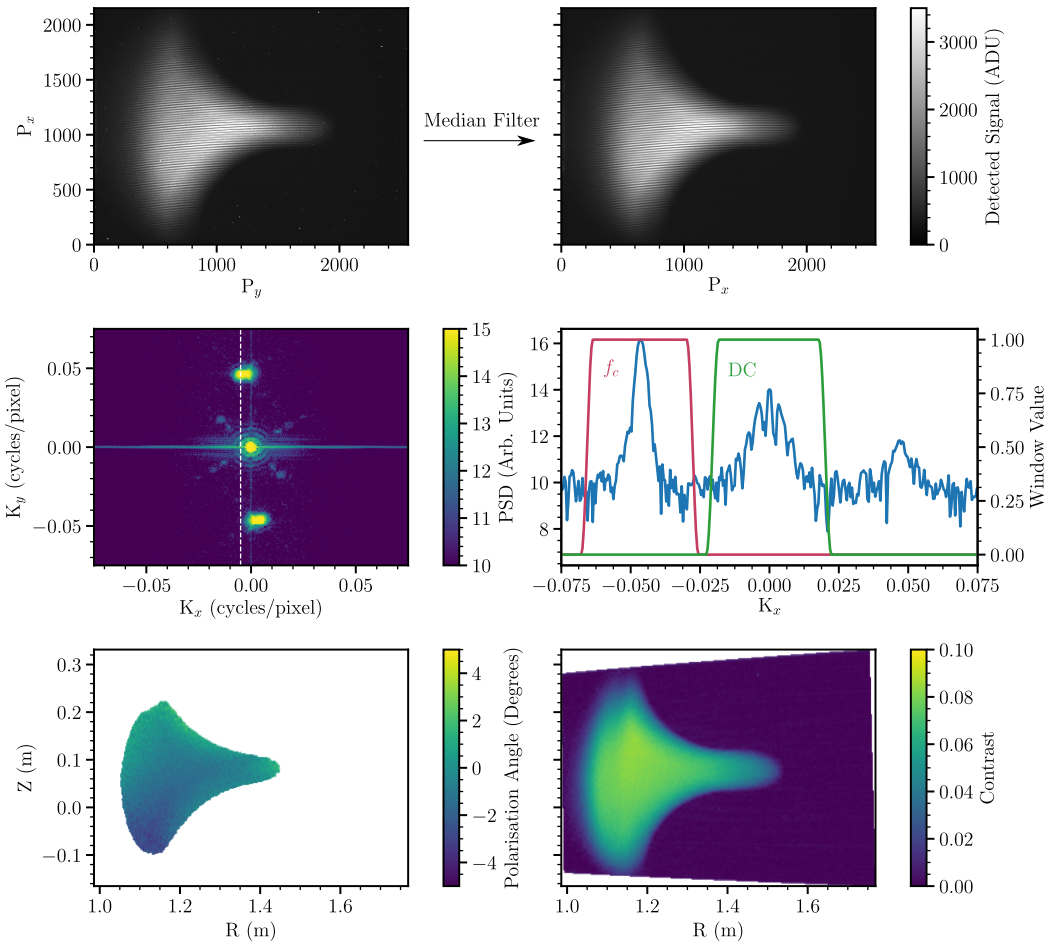

Figure 5.12: Demodulation process which recovers information on the polarisation angle using the phase difference between two successive interferograms. The power spectral density shows the single spatial carrier f_c. The carrier frequency f_c and DC component f_{DC} are filtered using a tapered Tukey window (red and green solid lines respectively). The resulting fringe contrast and polarisation angle are shown, where the 2D contrast provides a mask over regions of low contrast.

tion of plasma density for the forward B_ϕ plasma pulse 180088. Frames from the raw data where the 30R beam was not operating, where the interferogram would not be visible, have been removed. The measured fringe contrast over a subset of pixels looking at the same radial location (R=1.15m) and a vertical extent of 2cm were averaged to provide a measure of the average

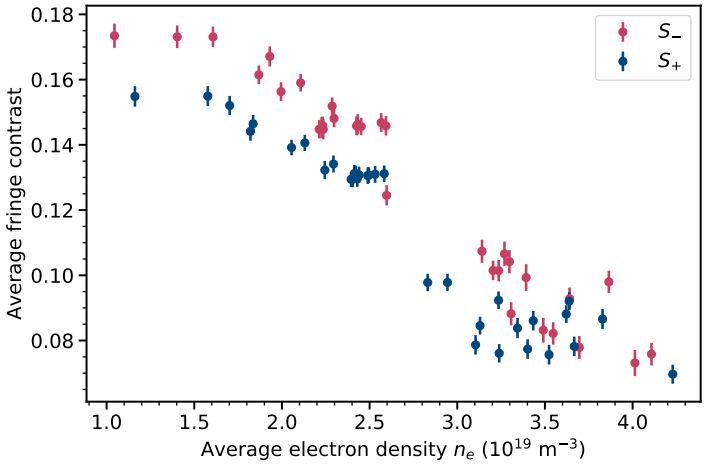

Figure 5.13: Variation in the interferogram fringe contrast as a function of the average core plasma electron density. As the electron density increases, the beam neutrals cannot penetrate as far into the plasma and beam attenuation increases.

fringe contrast in the image. As expected, the fringe contrast reduces as a function of electron density, as with increasing plasma density the level of visible Bremsstrahlung increases, reducing the overall polarised signal level.

However there is a minor difference in the average fringe contrast, depending on the state of the switching binary rotator. In frames where the binary rotator is in the switched state (applying zero delay to incident polarised light) the fringe contrast is systematically higher than in the unswitched state (applying a half wave delay). This is likely caused by a slight misalignment of the orientation the optic axis of the binary rotator in the switched state relative to the final polariser, leading to a reduction in the polarised emission through the binary rotator and overall reduced fringe contrast. This systematic difference becomes less apparent at higher core electron densities, since the signal level is already significantly reduced in both states due to both the beam attenuation and rising Bremsstrahlung background level.

5.4.3 Including measurements in EFIT

To include IMSE polarisation angle measurements in EFIT, subsets of pixels were binned into a small 2D grid. Using the mean and standard deviation

of the measured polarisation angle within these binned regions, a 1D radial profile, similar to the conventional MSE measurements, could be passed to EFIT as a constraint. A subset of pixels over ±1cm in the vertical extent is shown in Fig. 5.14, alongside a histogram of the polarisation angle measured within that region. The uncertainty due to random noise in the IMSE measurements is calculated using the standard deviation in the measurement over the selected vertical extent. To maximise the radial extent on the IMSE channels, measurements were taken across the centre of the image, where the tapering of the signal due to the RF shield is less severe.

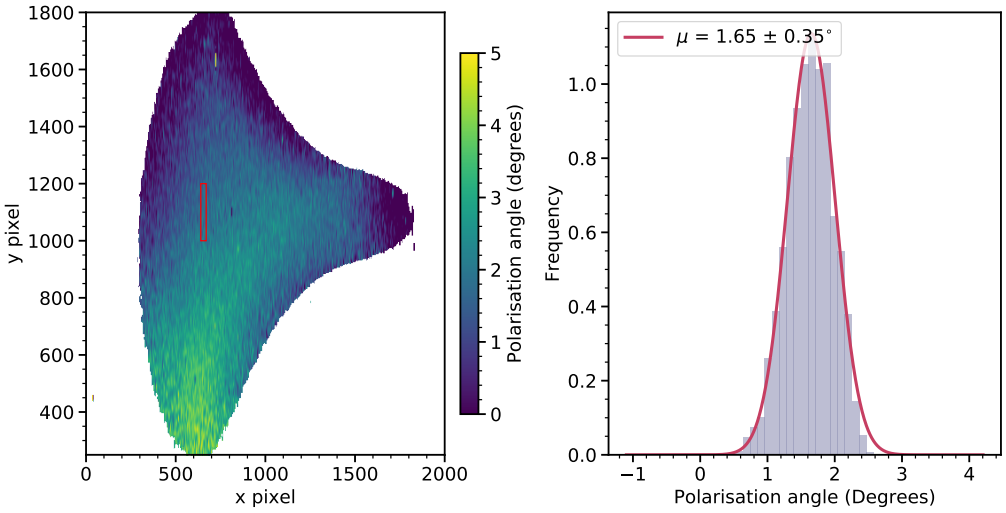

Figure 5.14: Left: Demodulated 2D polarisation angle, which is binned down into subsets of pixels to provide an averaged 1D radial measurement for use in the EFIT reconstruction code. A subsection within the red rectangle is chosen, which corresponds to a vertical extent of ±1cm. Right: Histogram plot of the measured polarisation angles for each pixel within the binned region (red rectangle). Fitting these pixel values to a Gaussian distribution reveals a standard deviation in the measurement over the vertical extent of $\sigma = \pm 0.35°$.

5.5 Observations in plasmas

5.5.1 Measurements in forward toroidal field plasmas

The majority of the plasma discharges where the 30R beam was available for IMSE measurements were run in the reverse toroidal field configuration.

During the campaign two discharges 180088 and 180062 were run with forward and reverse toroidal field respectively, and the plasma current direction remaining the same, providing opportunity to check the consistency of the measurements in both magnetic field configurations. These pulses were not 'identical', as can be seen in Fig. 5.15, where the reverse field shot had an increased plasma density and uses a current overshoot, resulting in a lower plasma current later in the discharge. The difference in the plasma density has implications on the level of neutral beam attenuation, particularly for the IMSE view towards the high field side, which can influence the measured polarisation angle due to changes in the observation volume. There were no dedicated identical plasma shots in L mode with minimal injected NBI power in both forward and reverse toroidal field configurations, but these two discharges provided IMSE data with good fringe contrast throughout the pulse and so were chosen for comparison.

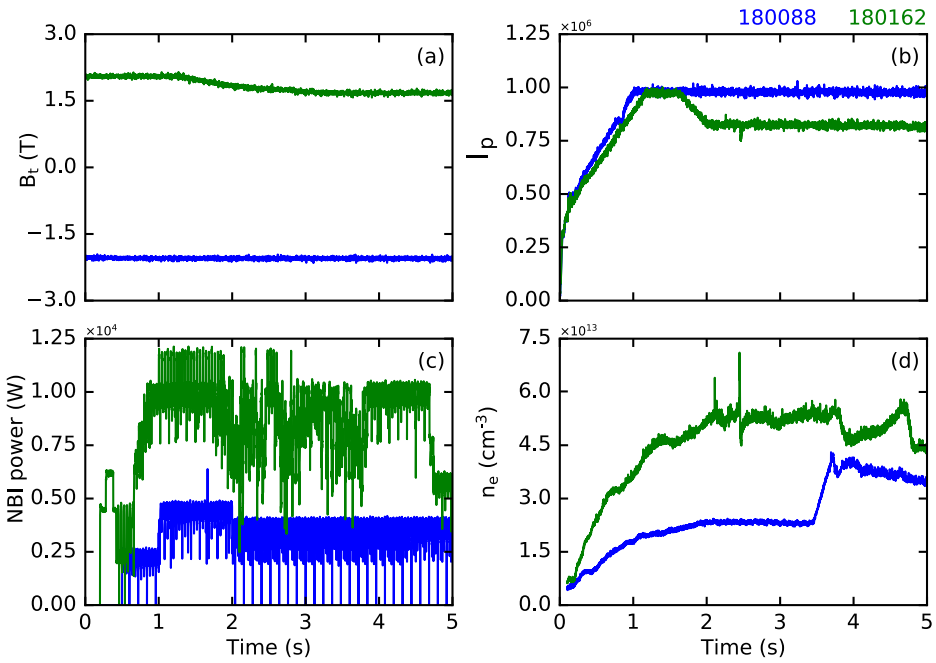

Figure 5.15: Plasma parameters in the forward toroidal field (180088, blue) and reverse toroidal field (180162, green) discharges. The magnitude of the toroidal field (top left) are similar but with the reverse direction in discharge 180162. The reverse discharge has a higher electron density, NBI power and lower plasma current.

An initial test for whether the IMSE system is providing reliable measure-

ments is to check for consistency with the conventional MSE system, which has been used routinely for equilibrium reconstruction[133]. Fig. 5.16 shows the variation in the measured polarisation angle profiles for both the IMSE (circles) and conventional MSE (triangles) systems during a forward toroidal field shot. The consistency between the outermost IMSE channels and inner most MSE channels around R = 1.5m is good, allowing EFIT to predict a smooth curve between both sets of measurements. EFIT provides a consistent fit to the both the conventional MSE and IMSE channels. The reduced χ^2 for the measurement remains stable over many time slices, with each timeslice fully converging, where the change in the poloidal flux function between iterations is $<10^{-4}$, showing that the measurements from both systems are consistent with one another over the entire plasma discharge.

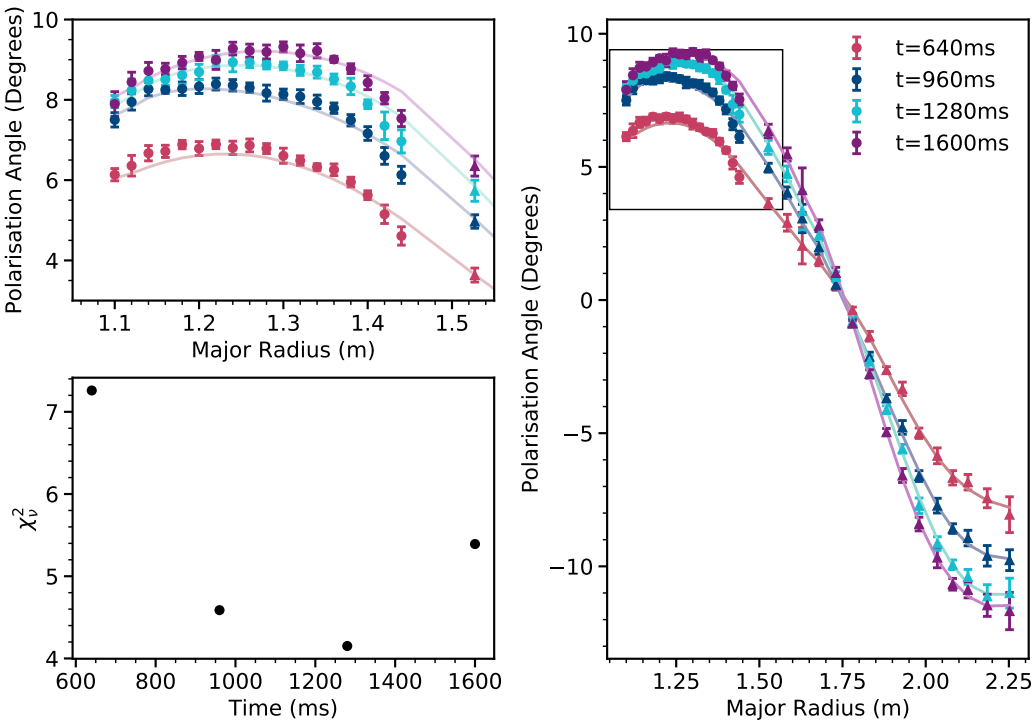

Figure 5.16: Measured pitch angles for several timeslices of the plasma discharge 180088. IMSE measurements (circle markers) show very good agreement with the conventional MSE system measurements (triangle markers). EFIT fits well to the IMSE data and obtains a low reduced χ^2 value.

Comparison of q profiles

The predicted q and toroidal current density profiles from an equilibrium with and without the 1D IMSE measurements included as a constraint are compared, as shown in Fig. 5.17 and Fig.5.18, to ascertain the influence of the IMSE constraint on the equilibrium profiles. Because the IMSE and conventional MSE measurements are self consistent, and as EFIT provides a good fit to both sets of data, there are only minor changes to the reconstructed q and current profiles in Fig. 5.17. EFIT was constrained using only IMSE measurements and excluding conventional MSE data. This provided q and current profiles more like EFIT constrained only with magnetics data. This is likely because the IMSE data only covers less than a third of the radial extent of the plasma. This leaves large areas of the poloidal flux unconstrained, and in particular the magnetic axis location, which also informs the value of q_0.

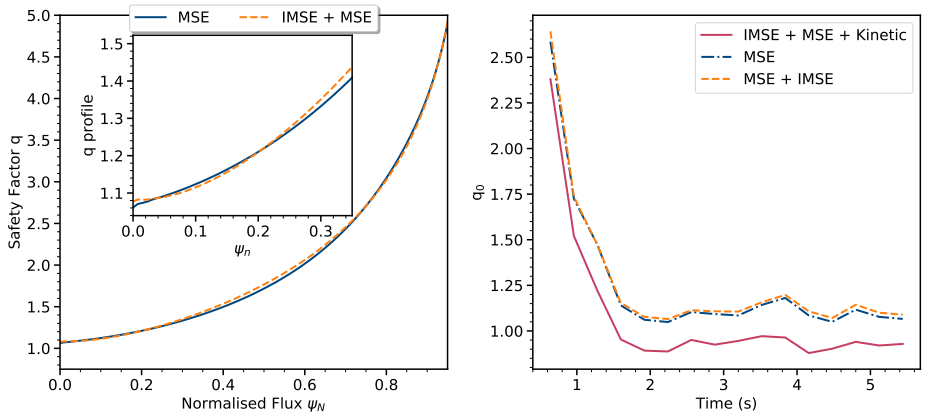

Figure 5.17: **Left:** Safety factor profiles produced by constraining EFIT using first only conventional MSE measurements (blue), then including both conventional MSE and IMSE measurements (orange). **Right:** Temporal evolution of q_0 when including additionally the MSE (blue), IMSE (orange) and kinetic (red) constraints into the equilibrium reconstruction.

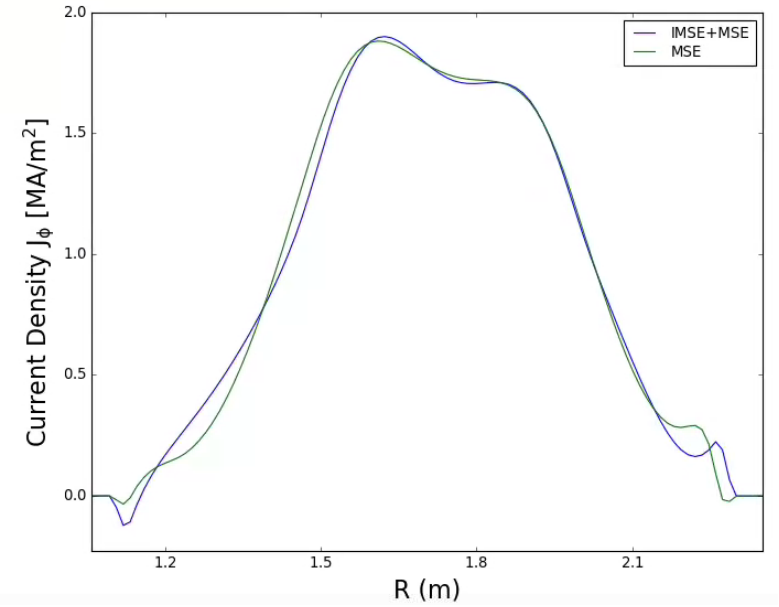

Figure 5.18: The toroidal current density computed by EFIT using the conventional MSE measurements (green) and then also including the IMSE measurements (blue) for the forward B_t discharge 180088 at t=1280ms. Including the IMSE measurements shifts current towards the high field side separatrix.

5.5.2 Reverse toroidal field plasmas

The measured polarisation angle is first compared to the computed polarisation angle by EFIT. Fig. 5.19 shows the measured 2D IMSE measured polarisation angle along with contours from the EFIT (constrained with magnetics and conventional MSE) computed polarisation angle. Good agreement between the location of the polarisation angle contours is found for the inner channels, however the measured polarisation angle is larger by around 2.5° than predicted by EFIT for the outer channels. This systematic offset occurs throughout the entirety of the discharge 180162, and for other reverse toroidal field discharges analysed. A change in the polarisation angle of $\delta\gamma$ = 2.5° over a distance of 10 cm, leads to a local current density of j_ϕ = -0.8 MA/m^2, which is approximately half of the total current density on axis. It has been shown that large transient current density peaks can be present at the plasma edge during H mode [134], however from Fig. 5.20 this current density would need to be present from the current ramp and through the flat top phase of the discharge. This suggests either the IMSE system measures a

consistently large current density at the plasma edge which is not predicted by the equilibrium in reverse B_ϕ plasmas, which is unlikely, or that there is a systematic uncertainty in the measurement which has not been accounted for. Therefore, we will explore possible systematic uncertainties which could affect the IMSE measurements at the plasma edge.

Asymmetry in the polarisation angle in the vertical extent is present beyond R=1.15m. If the neutral beam was infinitesimally thin and divergence free, then the polarisation angle contours should be up-down symmetric. If there was an asymmetry in the vertical beam velocity distribution, for example, a decrease in the vertical velocity component would lead to a decrease in the measured polarisation angle, due to its dependence on the beam velocity.

The discrepancy between the measured angles and the EFIT prediction is more clearly shown in Fig. 5.20, showing the midplane radial profile of the polarisation angle measured by the IMSE system, and the predicted angles from EFIT. The inner channels show good consistency with the conventional MSE system, but the slope of the outer IMSE data is larger than that predicted by EFIT.

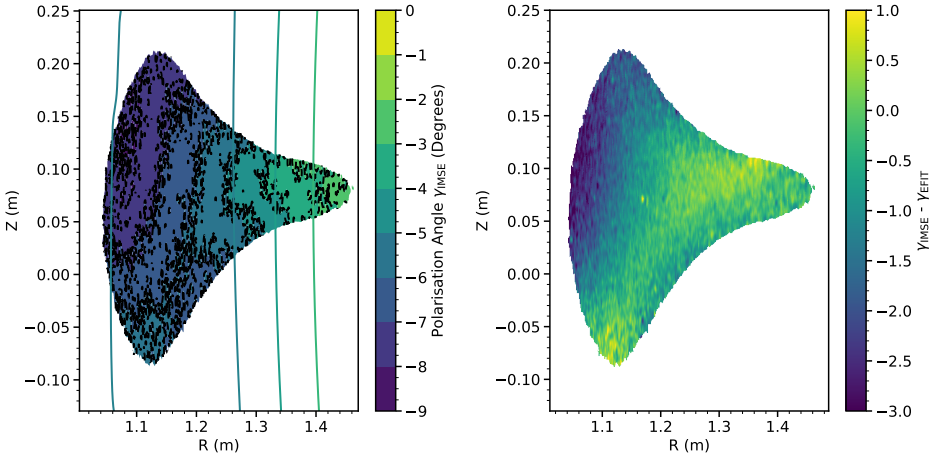

Figure 5.19: Left: Measured 2D polarisation angle for discharge 180162 t=1265ms, with EFIT predicted polarisation angle contours (lines) overlaid. Good agreement between the contour locations is found for the inner IMSE channels, but some asymmetry in the vertical extent of the polarisation angle is present towards the plasma edge. Right: Difference in the measured polarisation angle and expected polarisation angle calculated using the magnetic field components from a conventional MSE constrained equilibrium.

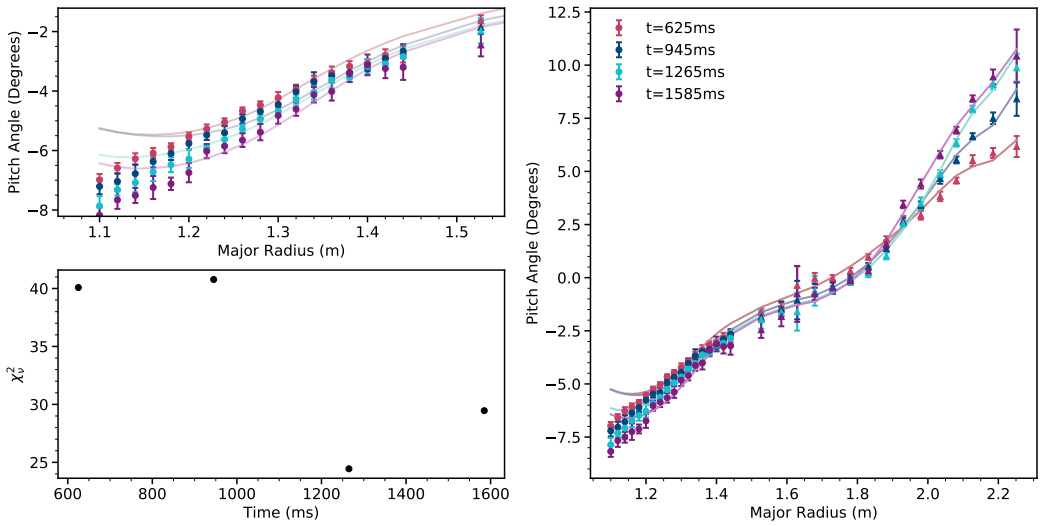

Figure 5.20: Top left: 1D polarisation angle measurements made by the IMSE polarimeter with the predicted values from EFIT (solid lines) for various times within the reverse B_t plasma discharge 180162. Bottom left: Reduced chi squared for the IMSE measurements when compared to the EFIT prediction. Note that χ^2_ν is significantly higher for the reverse field shot than in Fig. 5.16. Right: Measurements from both the IMSE polarimeter (circles) and the conventional MSE system (triangles) across the full radial extent of the plasma.

Consistency with magnetic probe measurements

Magnetic flux loops and probes situated in the mid-plane on the centre column provide a measurement of B_z close to the plasma boundary. This can be used to cross check B_z derived from the IMSE measurements at the plasma boundary where the discrepancy between the expected and measured polarisation angle occurs. In Fig. 5.21 the vertical field measured by the magnetic probes along the centre column is shown. Additionally the poloidal field is calculated from the polarisation angle using the geometric A coefficients[86] and the toroidal magnetic field component provided by an EFIT01 (magnetics only) equilibrium. When comparing the IMSE measured poloidal field to the inner magnetic probes, measurements closest to the separatrix are inconsistent with the poloidal field measured by the probes, leading to the discrepancy between the EFIT prediction and the IMSE measurements. The gradient of the derived Bz profile suggests there is an increase in the current density towards the plasma boundary (at R=1.1m), which is not captured by the equilibrium constrained with either the magnetics or conventional MSE system alone. Given that there was good agreement between

the edge channels and the magnetic probes in the forward toroidal field cases, there could be more current at the HFS plasma boundary than previously thought. Other additional corrections to the measured polarisation angle, such as Faraday rotation and the radial electric field terms in equation 5.7, are now discussed.

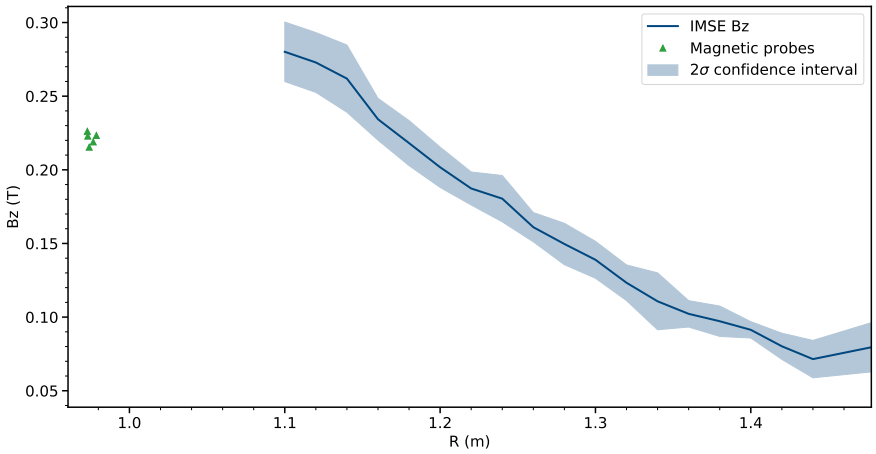

Figure 5.21: B_z profile derived from the IMSE polarisation angles. The mismatch in the B_z values measured at the plasma edge by the IMSE polarimeter and the magnetic probes along the center column explains the 'roll off' behaviour of the EFIT computed pitch angle profiles.

Radial Electric Field Effects

Plasma rotation and diamagnetism have been shown to influence the polarisation angle measured by MSE systems by giving rise to a significant radial electric field component, particularly at the plasma edge where the pressure gradient in H mode plasmas is significant [86]. The radial **E** field acts to shift the total electric field vector, and as such the angle of the polarisation angle with respect to the electric field. E_r contributions to the polarisation angle are accounted for through additional geometric A coefficients and an estimate of the radial electric field given the plasma toroidal rotation and pressure gradient contribution, $E_r = v_\phi \times \mathbf{B} + \nabla(n_i T_i)/e n_i$, assuming that the poloidal plasma rotation is small and the toroidal rotation term dominates in H mode discharges with strong neutral beam heating. It is difficult to distinguish between a change in the measured vertical field due to the local

current density or due to a contribution from E_r, and so it is useful to check the contribution of E_r to the measured polarisation angle, and whether this can explain the measurement discrepancy in reverse B_ϕ. The method for 'fast' E_r correction has been outlined elsewhere [135], under the assumption that measurements are made close to the vertical extent of the magnetic axis position, which is indeed the case for both conventional and averaged 1D IMSE measurements. In Fig. 5.22 the correction to the measured polarisation angle is $<0.15°$ for the imaging MSE channels. The correction then cannot alone explain the systematic deviation in the measurement of the edge channels in comparison to the prediction given by EFIT in the reverse B_t plasma scenarios.

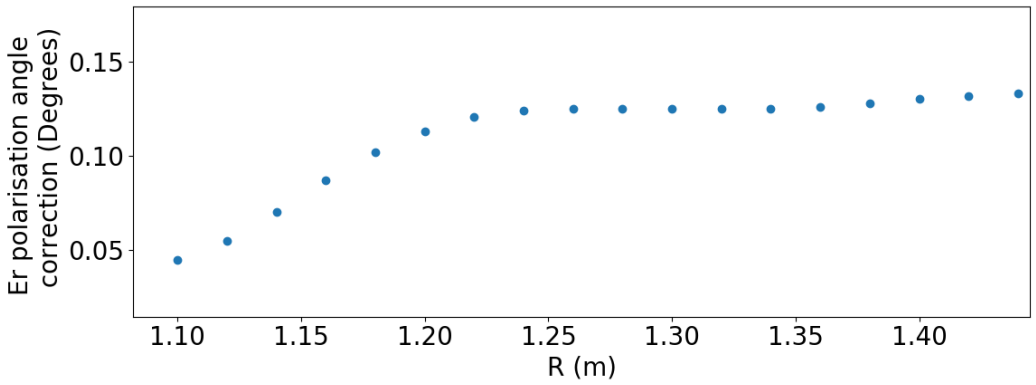

Figure 5.22: Correction to the measured polarisation angle due to radial electric field effects, calculated using the charge exchange recombination spectroscopy diagnostic[136], which for all IMSE channels is smaller than the difference between the EFIT prediction and measured polarisation angle and so cannot alone explain the measurement discrepancy in reverse B_ϕ.

Polarised Reflections

In many shots over the course of the campaign, particularly in initial frames or during a large disruption, an intense crescent was observed at the very high field side of the raw images. This occurred even in the absence of the 30R (or 30L) beam emission, and interferogram fringes were observed, suggesting an alternative source contributing polarised light from near the plasma edge. A frame from the plasma shot 180162 with poloidal flux contours from EFIT is shown in Fig. 5.23, indicating that the source lies beyond the boundary

and into the scrape off layer. It has been documented that partially polarised light can impact polarisation sensitive measurements [41]. Partially polarised light is attributed to sources such as reflections off vessel tiles[137], vessel walls consisting of highly reflective metals[138] and from components within optical systems such as mirrors[139]. There are no mirrors within the IMSE optical system at the 285° and so can be discounted as an explanation. However the intensely bright region aligns with a port vessel used for the polarimetry diagnostic shown in the left plot of the far wall within the vessel in Fig. 5.23, which includes a mirror at the front of the optical train. However if this was the contributing factor, we would expect to see similar observations as in Fig. 5.23 in the forward toroidal field plasmas as the field of view is unchanged between the two plasma scenarios. In Fig. 5.24, the beam emission intensity measured by the polarimeter at a later time in the discharge is shown, where the emission brightness is significantly enhanced at the plasma edge. The measured fringe contrast within this region is a small compared to a region towards the inboard side of the machine where beam emission is present, but is non-zero, indicating some of the emission in this region must be partially polarised.

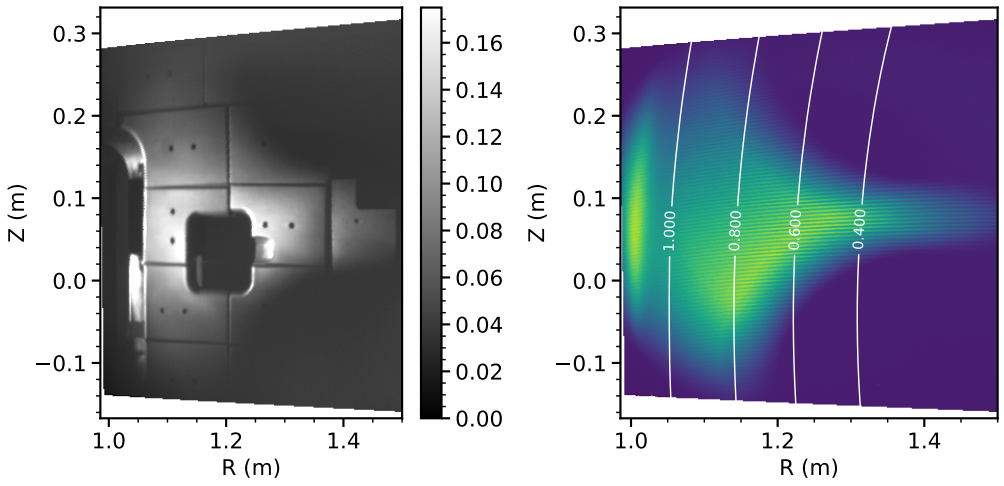

Figure 5.23: Left: View captured through the 285° IMSE port. Raw interferogram from reverse Bt shot 180162. Right: A distinct crescent of emission is present outside of the plasma boundary. Interferogram fringes are faint but visible within this region. Contours of normalised poloidal flux are overlaid (white) to show the boundary ψ_N=1 at R=1.05m.

Impact of D_α emission

Long exposures (τ=20ms) were required to improve the signal to noise availability in most plasmas due to the high plasma density and subsequent beam attenuation. Strong bursts of D_α emission during an ELM can illuminate the vessel and become a source of partially polarised emission. Fig. 5.25 shows several frames from the reverse field pulse, where in early and late times in the discharge the intense light is present at the plasma edge. The D_α emission intensity is plotted in Fig. 5.26 around the time of the exposures in Fig. 5.25. The full camera exposure time is indicated by the red shaded regions, showing that the time of the exposures there is minimal D_α activity, particularly for the early (t=260ms) and late (t=5620ms) times in the discharge, and as such D_α emission due to ELMs is not thought to be a factor. To further ensure the MSE emission is not swamped by D_α emission, an OD6 H-alpha blocking filter could be incorporated into the optical system at the D_α rest wavelength, however from this analysis it is reasonable to assume that D_α emission is not the cause of the discrepancy.

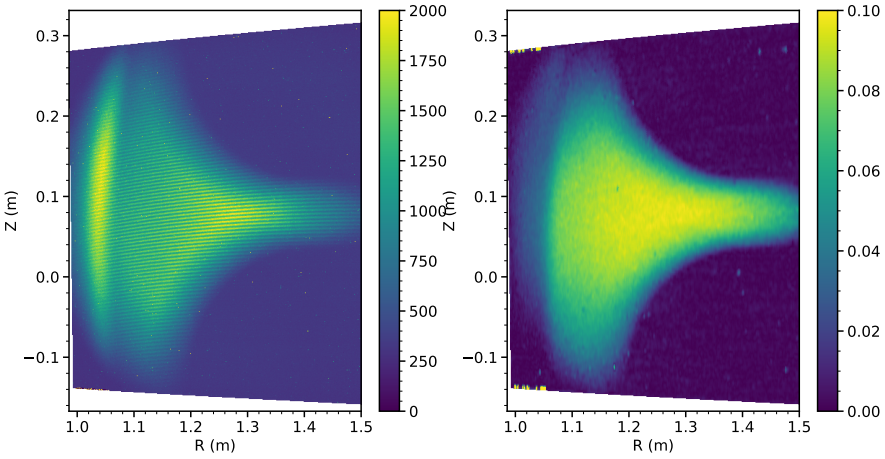

Figure 5.24: Left: Frame at a later time t=ms of the beam emission intensity measured by the polarimeter. Right: The measured fringe contrast for the interferogram fringes in the left plot. The measured fringe contrast at the location of the bright emission observed near the plasma boundary is small but non zero, suggesting there is a source of weakly polarised emission within that region.

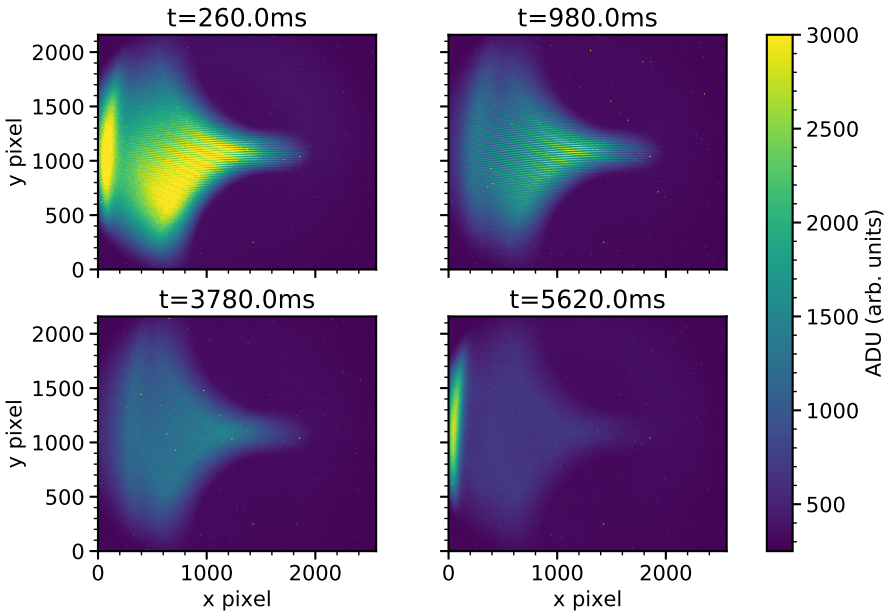

Figure 5.25: Time evolution of the 2D beam emission intensity measured by the IMSE polarimeter in discharge 180162. By the middle of the shot at t=3780ms the interferogram fringes are extremely faint as the beam neutrals are attenuated due to the high core plasma density. By the final few frames of the discharge, the 30R beam is no longer operating and so no fringes are present across most of the field of view, however the bright edge emission is present with faint interferogram fringes indicating some polarised light is present.

Zeeman split D_α and molecular D_2 emission

The temporal evolution of the intense crescent in Fig. 5.25 gives some indication that the source originates from the scrape off layer region, as the shape of the emission closely follows shape of the plasma boundary. The plasma boundary runs close to the inner wall, as shown by the radial location of the inner LCFS in Fig5.27, in the reverse toroidal field plasma. This could lead to increased plasma wall interactions, particularly if the discharge is started/ended by limiting the plasma onto the inner wall within the IMSE FOV. Other potential sources of polarised emission in the same wavelength region of the bandpass filter include D_2 molecules. The presence of D_2 molecules within the SOL have been measured previously on the DIII-D tokamak[140]. The Fulcher-alpha band spectrum for molecular deuterium has transition lines within the range 600-650nm, some of which would fall within the bandpass filter range for the edge IMSE channels. The strong toroidal field at

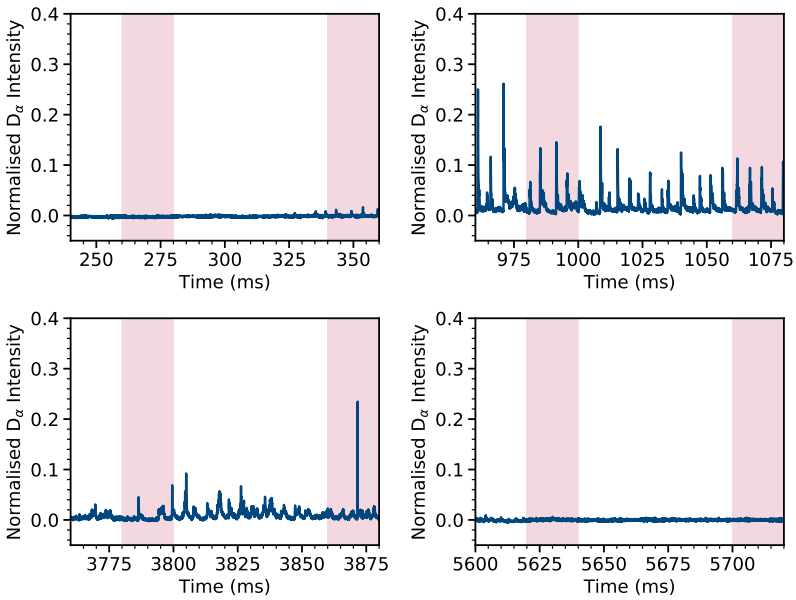

Figure 5.26: Evolution of the D_α emission intensity over the image exposures in Fig. 5.25. Frequent ELMs are observed at t=980ms and t=3780ms, but the supposed edge emission is not present. Therefore variation in D_α intensity due to ELMs is not thought to be the main source of the localised edge emission.

the HFS of the machine could additionally lead to Zeeman splitting of either the D_2 molecular lines or passive D_α line. Unfortunately it was not possible to obtain visible spectroscopic measurements at this time, and so for future campaigns passive spectroscopy measurements within the wavelength range λ=645-655nm would be useful to rule out emission contribution from any potential contaminant lines.

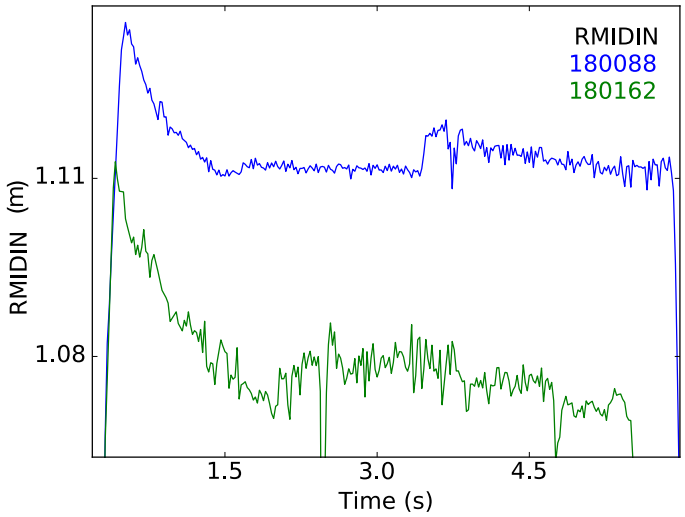

Figure 5.27: Radial location of the inner plasma boundary for the forward field (blue) and reverse field (green) discharges. The inner boundary is $\Delta R_{\text{in}} \approx 4$cm closer to the inner wall for the reverse field discharge.

5.5.3 Measurement of the Doppler phase

As described in section 5.3.2 the phase difference between interferograms produced in each state of the switching waveplate reveals the linear polarisation angle. Additionally the phase of each interferogram also includes the instrument phase ϕ_0, which depends on the Doppler shift of the MSE emission. An absolute measure of the Doppler shift contribution to the instrument phase can be retrieved if the instrument phase at a fixed wavelength is known; for example, through the calibration procedure in section 5.3.2. The contribution to the instrument phase due to the Doppler shift is given by $\phi_d = (\phi_{0,\text{plasma}} - \phi_c)/\phi_c$ where $\phi_{0,\text{plasma}}$ is the instrument phase measured in the plasma discharge and ϕ_c is the instrument phase measured at a fixed wavelength. Fig. 5.28 shows the derived emission wavelength from the instrument phase measured in plasma discharge 180238. There is a distinct phase jump in the measured wavelengths, which suggests that the calibration instrument phase ϕ_c is not representative of the contributing instrument phase in the real plasma data. There is a quadratic dependence to the measured wavelengths which is not present in the expected emission wavelengths calculated using the IMSE view geometry and location of the 30R beam. Without an improved understanding of the difference in the ray paths in the optical system in plasma discharges and during the calibration, it has not

been possible to correct this quadratic feature. As shown in section 5.3.2 the measured instrument phase even over the course of the calibration was susceptible to small drifts, and so drifts between the calibration and plasma instrument phase are extremely likely.

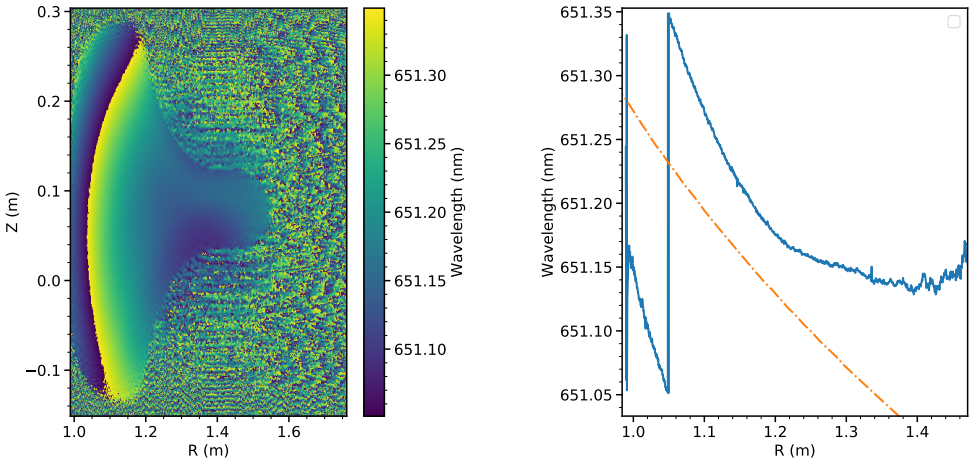

Figure 5.28: Left: Measured emission wavelengths calculated from the Doppler phase contribution. Right: Comparison of Z=0.08m measured wavelengths (blue) in left figure to the expected (dashed orange) wavelengths given the IMSE viewing geometry and neutral beam location.

Although the absolute value of the Doppler phase is difficult to fully quantify, the *relative* variation in the Doppler shift throughout a plasma discharge can be measured with relative ease. Between two frames captured within $\approx$ 60ms of each other, the instrument phase should remain constant, and so a reference Doppler phase can be measured from two initial exposures in the plasma discharge, and then the subsequent variation in the Doppler phase measured over time. In discharges with constant 30R beam voltage, and provided that the view geometry is well calibrated, the Doppler phase should also remain constant as the Doppler shift depends only on the beam velocity and view angle to the beam. In Fig. 5.29 the change in the instrument phase is shown for the plasma discharge 180173. In this discharge the toroidal field strength was slowly decreased, and the plasma current remained constant over the time the 30R beam fired. For the majority of the IMSE channels the contribution from the Doppler phase remains steady, with the Doppler phase drifting for channels outside of the plasma boundary. This contrasts to

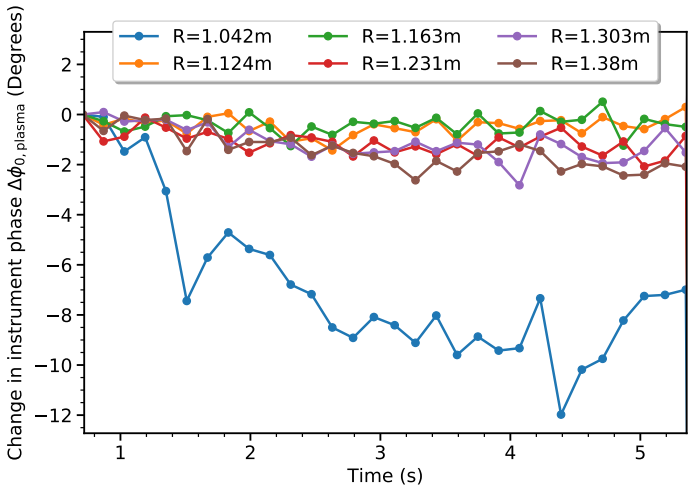

Figure 5.29: Variation in the measured instrument phase over plasma discharge 180173. For all IMSE channels located within the plasma the drift in the instrument phase is ±1°.

previous measurements of the instrument phase made using an FLC switching system[80] where drifts of up to 30° were noted during plasma discharges even when the beam voltage remained constant, but the toroidal field strength was varied. This is a positive result, meaning that for IMSE measurements made during the main heating phase of the discharge, the binary rotator could switch states once, increasing the time resolution of the measurements. This initial frame would act as the 'reference' instrument phase, and then the relative change in the polarisation angle would be measured by subsequent frames.

5.6 Conclusions

5.6.1 Summary

The DIII-D imaging MSE diagnostic operated successfully during a DIII-D experimental campaign from August to October 2019, with a unique view of the high field side of the machine where the inboard side of the plasma is poorly diagnosed. The 285° port posed some challenges including an RF shield obstructing the overall field of view, but allowed for measurements between R=1.0 and R=1.45m, meaning that for the first time measurements

of the polarisation angle were available over the full radial extent of the plasma.

In this iteration of the IMSE polarimeter, the ferro-electric liquid crystal (FLC) switching half waveplate was replaced with a twisted nematic liquid crystal (TNLC) switching half waveplate, as FLCs have previously exhibited significant spatial non-uniformity. The TNLC waveplate calibration revealed that the applied delay was more angularly uniform than the FLC, with variations of $\delta\phi = \pm 3^\circ$ from the average delay, which was larger than half wave at $\phi = 191.3^\circ$. This suggests that the TNLC is acting as a weak displacer, and could be contributing to the $\approx 4^\circ$ polarisation angle offset. Additional calibration measurements to precisely measure the orientation of the optical axis, could help to understand the origins of this offset. The IMSE polarimeter was successfully calibrated at the tokamak, showing that the polarimeter response was linear. A large systematic offset was measured relative to the input polarisation angle, suggesting minor misalignment of an optical component or additional rotation applied either by the quarter waveplate or TLNC waveplate. Including an additional rotation Mueller matrix and partial polariser matrix in the polarimeter Mueller analysis replicated the average offset measured by the polarimeter.

Although neutral beam attenuation was significant in high density plasmas ($n_e > 3.5\text{x}10^{19}\text{m}^{-3}$), good interferogram fringe contrast was achieved in many low density discharges. Analysis in this chapter demonstrates the consistency between polarisation angle measurements from the conventional MSE system and the IMSE system, particularly in the forward toroidal field plasmas. When including the IMSE measurements into EFIT, the reconstructed q profile and $q0$ evolution was similar to those inferred using only the conventional MSE measurements as a constraint. The additional of HFS measurements as an extra diagnostic constraint changed the distribution of the current density at both the inboard and outboard plasma edge. This resulted in increased current density at the HFS when compared to equilibrium constrained only with conventional MSE. The same impact on the current density was observed in reverse toroidal field plasmas.

Measurements in reverse field however showed some discrepancies with the

polarisation angle predicted by EFIT at the inboard plasma edge. Contributions to the polarisation angle from Faraday rotation in the port window ($\delta\gamma$ <0.4°) and the radial electric field arising from plasma rotation ($\delta\gamma$ <0.15°) were included. Combined these effects are insufficient to explain the 2.5° difference between the EFIT predicted and measured polarisation angles. An inconsistency in the poloidal magnetic field measured by magnetic probes on the inner wall and the inner IMSE channels was discovered, which is consistent with the slope of the EFIT predicted polarisation angles at the plasma edge. Other potential systematic uncertainties were explored. Bright intense polarised emission was observed at the HFS plasma edge, indicating reflections within the vessel is probably a source of partially polarised light. Other potential sources which could produce polarised emission within the wavelength range of the bandpass filter include; reflected beam emission from the inner wall, molecular Deuterium emission, other impurity lines, or Zeeman split D_α emission. The contribution of reflected beam emission to the interferogram phase would be particularly difficult to correct. For the latter, high resolution visible spectrometer data should be used to confirm the presence of any contaminant lines within the filter bandpass.

The temporal resolution of the diagnostic was limited by the switching time of the binary rotator. The waveplate switched states every other frame to ensure that variation in the instrument phase due to instrumental effects (caused by stress induced birefringence, temperature related drifts, etc.) was not coupled to the measured polarisation angle. However the instrument phase was shown to be stable to within ±1° over the majority of a plasma discharge. For future measurements, it will be possible to switch the binary rotator once to provide to determine the instrument phase contribution to the carrier phase and then retrieve the polarisation angle from each successive frame, boosting the temporal resolution to < 40ms.

Chapter 6

Summary and Conclusions

The goal of the work is to assess the capabilities of two motional Stark effect diagnostic techniques to recover information on the current profile in tokamak plasmas. In this chapter we provide an overview of the work and original contributions to diagnostic fusion research presented in this thesis. We discuss the potential impact on future work from this thesis, and finally place this research into a wider context with a discussion of future MSE diagnostics.

6.1 Thesis Summary

In this section we summarise the main findings presented in this work and discuss their implications.

In chapter 2, we reviewed the effect of external electric and magnetic fields on hydrogenic atoms to describe the motional Stark effect. We introduced the mathematical formalisms of the Stokes vector and Mueller matrices to calculate the effect of optical components on partially polarised light. For the conventional MSE system, we showed mathematically how the polarisation angle is encoded into the harmonic amplitude of photoelastic modulators (PEMs). Finally, we discussed the imaging MSE diagnostic, which uses a spatial carrier to modulate the full MSE multiplet and produce a net polarised signal. We showed that by using a combination of a switching halfwave plate and waveplates with arbitrary optic axis angles, polarisation information can

be encoded within the phase of a resulting interferogram.

6.1.1 Edge current density measurements on MAST

In chapter 3 we looked to measure the toroidal current density within the pedestal region using two approaches: Inference through constrained plasma equilibrium reconstruction and directly using conventional MSE diagnostic measurements. We first described the equilibrium code EFIT++ and the diagnostic constraints implemented within the code. We then showed that quality of the fit to the diagnostic data strongly depends on the chosen basis function representation. We showed that a spline basis function representation, and choosing knot points closely spaced near the plasma boundary are essential to fit the steep pedestal gradients in the pressure profile and fit structure in the MSE data on MAST. The basis functions and numerical settings were optimised and remained consistent for all analysed discharges in this thesis, which produced good convergence rates. MAST equilibria relied heavily on measurements from the D_α diagnostic for the plasma boundary constraint, due to noisy measurements from the outer magnetic probes. This lead to inconsistencies between the location of the plasma boundary between D_α, the Thomson scattering (TS) derived pressure profile and the MSE measurements, and leads to a reduction in the current density relative to the original equilibrium shown in [52]. These new resulting current profiles were then used to compare to the toroidal current density derived directly from the conventional MSE data.

An additional correction to the polarisation angle is required due to the influence of the radial electric field. The sensitivity of the conventional MSE system to the radial electric field was assessed, and for the edge MSE channels was measured to be $\delta\gamma < 0.2^\circ$ for a maximum radial electric field strength of E_r = -10 kV/m. Through knowledge of the viewing geometry and the toroidal field strength, it was shown that the vertical magnetic field component B_z can be derived. Subsequently using the spatial gradient of B_z and Amperes law we derived the toroidal current density. Two MAST plasma discharges were analysed which contained a long ELM free period prior to a type-I ELM. Due to the fast temporal resolution of the MSE system, meas-

urements of the polarisation angle were available for times 2ms before and after the ELM. For discharge 24408, there was both a clear increase in the polarisation angle just prior to the ELM and subsequent decrease in the time just after the ELM crash, implying that the current density increases prior to the ELM. However, due to the large uncertainties in the derived current profile, the uncertainty in the edge current peak would hinder the possibility of accurate stability analysis. Finally, we used the equilibrium reconstruction code EFIT++ to determine the edge current density. This was achieved by constraining the equilibrium with magnetic measurements, MSE measurements, pressure measurements derived from the Thomson scattering (TS) diagnostic, and an estimation of the D_α boundary location. We showed that the resulting current density peak is sensitive to the uncertainties in the diagnostic data, in particular inconsistencies in the location of the boundary measured by the D_α camera and the TS measurements. We concluded that improved integrated data analysis of the profiles in the pedestal would be necessary to improve the accuracy in the edge current density for stability analysis.

6.1.2 Imaging MSE diagnostic design for MAST-U

Given the results in chapter 3, it was clear that achieving routine inter-ELM resolution of the current profile is challenging with the conventional MSE system. An increase in the spatial resolution of the MSE measurements across the pedestal would be required to fully resolve the edge current density. Unfortunately the spatial resolution of beam spectroscopy diagnostics are limited by the finite neutral beam width. However it would be possible to achieve an increase in the measurement resolution by simply increasing the number of measurements made in the pedestal region, given that the important factor in measuring a change in the local current density is that the uncertainty in the *spatial gradient* of the polarisation angle must be minimised.

In Chapter 4, the spectral modelling code MSESIM was used to model the MSE spectrum for MAST Upgrade, including spectral broadening effects. We showed that, even with the increased toroidal field strength, the spectral

broadening effects are still significant on the MAST-U spectrum and the π and σ lines cannot be resolved. We coupled a forward model, written in python, to MSESIM to model the optical components in the IMSE system. This model included the birefringent waveplates and two potential candidate detectors. Mueller matrix analysis of the candidate modulation techniques, the temporally switched single spatial heterodyne was developed symbolically in Mathematica.

Our forward model allowed us to design an imaging MSE system for MAST Upgrade, considering non-ideal effects such as non-axial ray effects. When these effects were in included to generate synthetic diagnostic images, it was clear that a 'field widening' technique was required to reduce the inteferogram fringe curvature caused by the thick displacer and delay plates. We produced synthetic IMSE diagnostic images for a range of typical MAST-U plasma scenarios, using our proposed system. These images demonstrate that in MAST-U H-mode plasmas the diagnostic would be capable of recovering edge current features. When accounting for shot noise, the uncertainty in the recovered polarisation angle is expected to be $<0.5^\circ$ at 2 ms time resolution. While this in itself is comparable to the existing diagnostic, the significant increase in number of measurements due to the megapixel sensor means that the noise uncertainty can be reduced significantly through pixel binning.

6.1.3 Imaging MSE on the high field side of DIII-D

In chapter 5, we presented results from an imaging MSE diagnostic operated on the DIII-D tokamak. The IMSE system had a unique view of the high field side of the tokamak, where generally diagnostics cannot obtain measurements due to access restrictions. For the first time measurements of the magnetic pitch angle were available across the entire plasma, with the IMSE system covering from R=1.0m to 1.45m, and a conventional MSE system situated at another diagnostic port beyond R=1.5m.

We extended the demodulation routine developed in Chapter 4, to account for the challenges of using real plasma data. This included removing hot pixel noise caused by neutrons using a median filter, and modifying the frequency filtering windows to reduce ringing in the demodulated polarisation angle

profile.

Although the neutral beam attenuation was significant in high density plasmas, the interferogram fringe contrast remained above 10% for core electron densities of $< 2.5 \times 10^{19}$ m^{-3}. Good fringe contrast was achieved across many discharges, particularly at the beginning and end of the pulse. Analysis of the IMSE data showed that the measurements from the IMSE system were consistent with the conventional MSE system in forward toroidal field plasmas. Measurements in reverse field however showed some discrepancies with the polarisation angle predicted by EFIT at the inboard plasma edge. Contributions to the polarisation angle from Faraday rotation in the port window ($\delta\gamma$ <0.4°) and the radial electric field arising from plasma rotation ($\delta\gamma$ <0.15°) were included but were insufficient to explain the 2.5° difference between the EFIT-predicted and measured polarisation angles.

Other potential systematic effects were further explored to explain the measurements in reverse field plasmas. One candidate explanation is the presence of polarised line emission at the plasma edge. Bright intense emission was observed in the interferogram at the edge of the plasma throughout many of the reverse field discharges. This was clearly at least weakly polarised, as interferogram fringes were present over this edge region. Using the plasma boundary location from EFIT showed this emission must originate outside of the plasma. Some potential sources include: Reflected beam emission from the inner wall, molecular Deuterium emission, other impurity lines, or Zeeman split D_α emission. The contribution of reflected beam emission from the inner wall to the interferogram phase would be particularly difficult to correct. Visible spectrometer data could assist in explaining the source of the polarised emission, to look for any impurity lines which may be present in the wavelength region of the IMSE bandpass filter.

6.2 Outlook

In this section we describe how the work presented in this thesis, alongside other developments in the field, can be used in future MSE diagnostics.

6.2.1 Equilibrium reconstruction development

There have been several recent advances in automatic profile fitting routines and integrated modelling developments to allow for more routine equilibrium reconstruction including a wider set of diagnostic measurements [93, 141], which could be used to run automatic equilibria on MAST-U. Currently this must be done manually by diagnostic and equilibrium specialists, which requires significant personnel time.

Currently the uncertainty in the equilibrium due to diagnostic measurement uncertainties is not well understood on MAST. This could be improved by a perturbation study, whereby the diagnostic measurements are perturbed within the error bars of the measurements to generate a whole possible set of equilibria which both are solutions of the Grad-Shafranov equation and provide good fit to the data. However this analysis would only be as robust as the uncertainty estimates in the measurements. Alternatively, a Bayesian approach may be attractive [48, 142], but can be computationally expensive and require accurate diagnostic forward models. It is hoped that producing the forward model of the IMSE system in this work will lead to further development of detailed forward models for other MAST-U diagnostics (such as the D_α camera, Thomson scattering diagnostic and magnetic probes) to work towards this Bayesian approach to equilibrium.

6.2.2 Towards routine edge current measurements

One of the main challenges in direct measurement the edge current density routinely on MAST was due to the spatial resolution of the conventional MSE system. For MAST-U plasmas, the location of the plasma boundary will likely shift inwards due to the increase in plasma elongation, into a region where the fiber sightlines are more tangent to flux surfaces. This will hopefully lead to a small improvement in the spatial resolution. However the main development in this area would be through an additional series of plasma pulses specifically designed to measure the edge current density. To test the resolving capabilities of the MSE system, the plasma boundary could be shifted inwards periodically throughout the plasma. It should then

be possible to detect a periodic increase in the polarisation angle across different channels depending on where the plasma boundary is moved.

For MAST-U the synthetic aperture microwave imaging (SAMI) diagnostic [110] will also become available in the near future. SAMI uses back scattered microwave radiation to measure the magnetic field line pitch and hence has the ability to measure the edge current density. Measurements from these two diagnostics should be compared to derive a consistent pedestal current density profile between the two diagnostics.

6.2.3 Development of the MSE forward model

From the work in chapter 4, there are several avenues where the spectral modelling code MSESIM could be further developed, particularly to improve accurate modelling of imaging based MSE diagnostics. MSESIM could be developed to handle more complex optical systems, such as multiple lens systems, which would improve the accuracy in modelling three lens IMSE systems. Including a more generalised étendue calculation would expand the model applicability beyond fiber based MSE systems to more general polarimetry applications.

The MSESIM beam model is relatively basic, but does allow for assessment of the finite beam width effects. Beam emission profiles are available for MAST currently in the code and were used in the simulation work presented in chapter 4. However coupling MSESIM with a neutral beam modelling code [143] would allow for more accurate modelling of other NBI sources with different ion grid geometries, on machines such as DIII-D.

Other plasma modelling and ray tracing codes used at MAST-U such as CHERAB can now successfully forward model active spectroscopy diagnostics for fusion applications, as well as the spectral intensity of the MSE multiplet [144]. Currently the ray tracer coupled to CHERAB does not have the functionality to retain polarisation information of either plasma emission, or light reflected and transmitted through optical components. This is an obvious area for future development, which would be beneficial for modelling both the conventional MSE and imaging MSE diagnostics.

6.2.4 Further Development of the IMSE diagnostic

From the work in chapter 5, it is clear that the IMSE diagnostic is becoming more mature and capable of producing reliable measurements of the magnetic pitch angle. However, to live up to its full potential as a routine plasma diagnostic, there is still scope to improve in several key areas.

Development of the IMSE calibration

Improvements to the calibration procedures, both for the individual components and the full polarimeter could be made in order to more accurately model the polarimeter response. The component calibration using the rotating polariser should be performed for each component in the system individually, starting with solely the crossed polarisers, and taking a background image for each dataset, then repeated for each successive component (eg. the switching waveplate, then the quarter waveplate). Additionally, this reduces the number of free parameters when fitting the transmission intensity curves and would improve the reliability of extracting the delay and orientation of each polarimeter component. The switching waveplate should also be calibrated in the focal region to assess the spatial dependence of the delay. Using this method to retrieve the weighting factors for each Stokes component as described in [80] would improve the forward model of the polarimeter by including the impact of circularly polarised light on the interferogram phase. The 'gold standard' for calibrating MSE diagnostics remains the 'beam into gas calibration', which provides an absolute polarisation angle offset including effects such as Faraday rotation. These specialist shots can be difficult to obtain, however it would be useful to compare these to the polarisation angle offset measured using a polarised light source and integrating sphere.

Potential upgrades to diagnostic hardware

Ultimately the limit on the switching IMSE system is the temporal resolution of the twisted nematic rotator. In order to capture the full dynamics of physics phenomenon, either the switching rate of the waveplate must be improved, or a waveplate with reduced switching time acquired. Although

the uniformity of the twisted nematic based waveplates is improved compared to the FLC counterparts, evidently there is a trade off between the retardance uniformity and the switching rate which must be considered.

The current DIII-D IMSE system had air flow through the diagnostic to stabilise the temperature of the polarimeter components. However, using a temperature controlled oven would minimise drifting of the instrument phase and allow for a reduced switching rate for the binary rotator.

The length and starting time of the beam blips for the neutral beam was shifted depending on the focus of the main experiments. The binary rotator switching rate had to be manually adjusted accordingly. If the diagnostic were to be assigned a permanent diagnostic port, it would be useful to use the 30R beam timings to pre-calculate and set the switching rate with minimal user intervention.

Linking this experimental work to the IMSE design for MAST-U in chapter 4, some real world diagnostic issues were encountered which will undoubtedly improve the diagnostic design further. For example, we should consider shielding of the camera from the magnetic field, recording the input waveform to the switching waveplate to monitor the state of the waveplate and surrounding the crystals in a temperature controlled oven. On the software development side, for routine data analysis we should ensure that the demodulation code is parallelised to reduce computational speed and use 'lazy loading' of raw images when processing to reduce memory requirements [145].

Finally, some exciting developments in micro-polarizer imaging camera technology could provide opportunity for further IMSE diagnostic designs [146]. A spatial carrier would still be required to separate polarisation information from the instrument and Doppler phase contributions, but this could improve mechanical stability at a minor cost to the radial resolution.

Further analysis of the IMSE data

Extensions of the analysis should look to resolve the question of the source of polarised emission at the edge of the plasma on DIII-D, which could be contributing a systematic uncertainty in the reverse toroidal field data. Analysis of visible spectrometer data at the HFS edge can confirm the presence

of any contaminating polarised line emission within the bandpass filter. Development work to understand the impact of reflections from vessel components could include shining an unpolarised light source towards the wall tiles viewed by the IMSE polarimeter. This could be completed at different locations, such as from close to the upper or lower divertor and at the midplane to understand if the polarised light source is highly localised and whether certain incidence angles produce strongly polarised light directed towards the polarimeter. This of course requires significant vessel access and so would only be achievable during machine downtime between campaigns.

Additional data analysis should also look to fully exploit the 2D nature of the IMSE data. The vertical information available at the 285° port was somewhat limited due to the restricted view, were this not the case additional information in the poloidal plane could be inferred. Additionally, if improvements in the calibration of the instrument phase are made, information on both the beam velocity distribution and beam divergence could be inferred [77]. This would be particularly useful for the HFS view where the beam attenuation is strong in high density plasmas, and the beam velocity distribution is not well known.

As this work has shown that the conventional MSE and imaging MSE measurements can be self consistent, additional work should look to routinely include IMSE measurements as a constraint in EFIT. EFIT reconstructions using the IMSE data as a constraint should be cross validated with MHD analysis. This can be achieved by analysing plasma discharges with a 'known' q profile, due to the presence of signature MHD markers, and locating rational q surfaces with MHD analysis in order to cross check the IMSE-constrained equilibrium q profiles.

6.3 Towards an MSE diagnostic suite for ITER

Some effort has been made towards adapting MSE techniques for the next generation of fusion reactors such as ITER. This raises the question: Which of the conventional MSE or imaging MSE diagnostic is better suited for future

fusion reactors?

The conventional MSE approach lends itself well to adapting to real time measurements [76], which are extremely useful for real time feedback on the q profile, which is required to avoid instabilities. ITER requires a temporal resolution of 10 ms, with radial resolution of $\Delta R = 5$ cm, and constraint on the equilibrium reconstruction to resolve the q profile to within 10% [147]. All of these requirements have been achieved with other conventional MSE systems, such as on the JET tokamak [127], a tokamak capable of producing plasmas akin to the conditions for ITER.

In terms of physical diagnostic requirements, long diagnostic optical trains will be required for these larger machines to pass through the cryostat. This will introduce multiple mirrors into the optical system, which have been shown to introduce measurement drifts due to changes in reflectivity properties of mirrors over the lifetime of the diagnostic [41]. Modelling of the mirror reflectivity for ITER suggests that Helium fluxes may significantly reduce the mirror reflectivity and requires further study [148]. This will lead to requiring significant access to the optics for calibration and replacement of mirrors, which does not meet the requirements for the long duty cycle operation that ITER diagnostics will require.

Additionally, the harsh neutron environment degrades the quality of optical fibers and can affect the PEM controllers. Upgrading some components of the conventional MSE diagnostic on JET was required in preparation for the DT campaign in 2020, which included moving the PEM controllers from the torus hall to the basement area to reduce the risk of neutron damage to the controllers. Evidently this too would be an issue for ITER and larger scale tokamaks. These challenges are applicable to both the conventional MSE diagnostic and imaging MSE system, if one were to be developed for ITER.

Finally, background polarised light from reflections in the metallic walls and divertor will be significant in ITER, and has proven to be a problem for many MSE diagnostics [41, 67, 149]. A study [150] proposed a hybrid of the conventional MSE system combined with a birefringent waveplate to match the periodicity of the Stark spectrum as in the imaging MSE systems to reduce the impact of partially polarized background light.

One alternative solution is the MSE line splitting (MSE-LS) technique [39] to measure the MSE spectrum and the Stark shift of the components within the multiplet to calculate the magnitude of the magnetic field. The MSE-LS diagnostic measures the total spectral intensity, and polarisation information is not preserved, so mirror degradation becomes a more minor issue and can be accounted for in spectral fitting. Additionally this technique would suit the strong toroidal fields (6 T on axis) and beam energies (100 keV/amu) of the negative ion neutral beam injector systems, as the Stark wavelength separation will be significant and only the full energy multiplet is produced making spectral fitting less complicated. The MSE-LS approach was modelled for ITER conditions, and for an uncertainty in the q profile of <5%, a sensitivity to the magnetic field of at least $\delta B = 10$ mT is required [151]. Experimental measurements from the MSE-LS "B-Stark" diagnostic on DIII-D [152] showed at least 10 MSE-LS measurement locations are needed, as well as information on the magnetic axis position from other constraints, in order to achieve the required accuracy in the q profile. ITER will only include the MSE-LS diagnostic.

Bibliography

[1] R. Scannell, M. J. Walsh, M. R. Dunstan, J. Figueiredo, G. Naylor, T. O'Gorman, S. Shibaev, K. J. Gibson, and H. Wilson, Review of Scientific Instruments **81**, 1 (2010).

[2] IEA, *Global Energy Review 2020*, Tech. Rep. (Paris, 2020).

[3] V. Masson-Delmotte, P. Zhai, H. Pörtner, D. Roberts, J. Skea, P. Shukla, A. Pirani, W. Moufouma-Okia, C. Péan, R. Pidcock, S. Connors, J. Matthews, Y. Chen, X. Zhou, M. Gomis, E. Lonnoy, T. Maycock, M. Tignor, and T. Waterfield, *IPCC, 2018: Summary for Policymakers. In: Global Warming of 1.5°C. An IPCC Special Report on the impacts of global warming of 1.5°C above pre-industrial levels and related global greenhouse gas emission pathways, in the context of strengthening the global*, Tech. Rep. (In Press., 2018).

[4] C. Bustreo, U. Giuliani, D. Maggio, and G. Zollino, Fusion Engineering and Design **146**, 2189 (2019).

[5] A. Glaser and R. J. Goldston, Nuclear Fusion **52**, 10.1088/0029-5515/52/4/043004 (2012).

[6] E. E. Bloom, R. W. Conn, J. W. Davis, R. E. Gold, R. Little, K. R. Schultz, D. L. Smith, and F. W. Wiffen, Journal of Nuclear Materials **122**, 17 (1984).

[7] C. Hill, Learning Scientific Programming with Python.

[8] I. A. E. Agency, IAEA Nuclear Data Services.

[9] A. R. Raffray, M. Akiba, V. Chuyanov, L. Giancarli, and S. Malang, Journal of Nuclear Materials **307-311**, 21 (2002).

[10] P. R. Thomas, P. Andrew, B. Balet, D. Bartlett, J. Bull, B. de Esch, A. Gibson, C. Gowers, H. Guo, G. Huysmans, T. Jones, M. Keilhacker, R. Koenig, M. Lennholm, P. Lomas, A. Maas, F. Marcus, F. Nave, V. Parail, F. Rimini, J. Strachan, K. D. Zastrow, and N. Zornig, Physical Review Letters **80**, 5548 (1998).

[11] Y. Shimomura, Y. Murakami, A. R. Polevoi, P. Barabaschi, V. Mukhovatov, and M. Shimada, Plasma Physics and Controlled Fusion **45**, 687 (2001).

[12] A. J. Creely, M. J. Greenwald, S. B. Ballinger, D. Brunner, J. Canik, J. Doody, T. Fülöp, D. T. Garnier, R. Granetz, T. K. Gray, C. Holland, N. T. Howard, J. W. Hughes, J. H. Irby, V. A. Izzo, G. J. Kramer, A. Q. Kuang, B. Labombard, Y. Lin, B. Lipschultz, N. C. Logan, J. D. Lore, E. S. Marmar, K. Montes, R. T. Mumgaard, C. Paz-Soldan, C. Rea, M. L. Reinke, P. Rodriguez-Fernandez, K. Särkimäki, F. Sciortino, S. D. Scott, A. Snicker, P. B. Snyder, B. N. Sorbom, R. Sweeney, R. A. Tinguely, E. A. Tolman, M. Umansky, O. Vallhagen, J. Varje, D. G. Whyte, J. C. Wright, S. J. Wukitch, and J. Zhu, Journal of Plasma Physics , 1 (2020).

[13] R. J. Hastie, Astrophysics and Space Science **256**, 177 (1997).

[14] R. J. La Haye, Physics of Plasmas **13**, 10.1063/1.2180747 (2006).

[15] A. Harms, K. Schoepf, G. Miley, and D. Kingdon, *Principles of Fusion Energy* (World Scientific Publishing Co. Pte. Ltd., London, 2000) p. 127.

[16] T. R. Barrett, C. Jones, P. Blatchford, B. Smith, R. McAdams, and N. Woods, Fusion Engineering and Design **86**, 789 (2011).

[17] J. Wesson and D. J. Campbell, *Tokamaks* (Oxford University Press, 2011).

[18] S. M. Kaye, M. G. Bell, R. E. Bell, E. D. Fredrickson, B. P. Leblanc, K. C. Lee, S. Lynch, and S. A. Sabbagh, Nuclear Fusion **46**, 848 (2006).

[19] A. E. Costley, J. Hugill, and P. F. Buxton, Nuclear Fusion **55**, 10.1088/0029-5515/55/3/033001 (2015).

[20] A. Sykes, Nuclear Fusion **39**, 1271 (1999).

[21] R. J. Akers, A. Bond, R. J. Buttery, P. G. Carolan, G. F. Counsell, G. Cunningham, S. J. Fielding, C. G. Gimblett, M. Gryaznevich, R. J. Hastie, P. Helander, T. C. Hender, P. J. Knight, C. N. Lashmore-Davies, G. P. Maddison, T. J. Martin, K. G. McClements, A. W. Morris, M. R. O'Brien, C. Ribeiro, C. M. Roach, D. C. Robinson, A. Sykes, G. M. Voss, M. J. Walsh, H. R. Wilson, and F. S. Zaitsev, Nuclear Fusion **40**, 1223 (2000).

[22] D. N. Hill, Nuclear Fusion **53**, 10.1088/0029-5515/53/10/104001 (2013).

[23] M. E. Austin, A. Marinoni, M. L. Walker, M. W. Brookman, J. S. Degrassie, A. W. Hyatt, G. R. McKee, C. C. Petty, T. L. Rhodes, S. P. Smith, C. Sung, K. E. Thome, and A. D. Turnbull, Physical Review Letters **122**, 115001 (2019).

[24] General Atomics DIII-D.

[25] J. Harrison, *MAST Upgrade Research Plan*, Tech. Rep. (Culham Center for Fusion Energy, UKAEA, 2019).

[26] STEP - Spherical Tokamak for Energy Production.

[27] e. a. J.R. Harrison, Nuclear Fusion **59**, https://doi.org/10.1088/1741-4326/ab121chttps://doi.org/10.1088/1741-4326/ab121c (2019).

[28] S. F. Smith, S. J. Pamela, A. Fil, M. Hölzl, G. T. Huijsmans, A. Kirk, D. Moulton, O. Myatra, A. J. Thornton, and H. R. Wilson, Nuclear Fusion **60**, 10.1088/1741-4326/ab826a (2020).

[29] G. Fishpool, J. Canik, G. Cunningham, J. Harrison, I. Katramados, A. Kirk, M. Kovari, H. Meyer, and R. Scannell, Journal of Nuclear Materials **438**, S356 (2013).

[30] P. T. Lang, A. Loarte, G. Saibene, L. R. Baylor, M. Becoulet, M. Cavinato, S. Clement-Lorenzo, E. Daly, T. E. Evans, M. E. Fenstermacher, Y. Gribov, L. D. Horton, C. Lowry, Y. Martin, O. Neubauer, N. Oyama, M. J. Schaffer, D. Stork, W. Suttrop, P. Thomas, M. Tran, H. R. Wilson, A. Kavin, and O. Schmitz, Nuclear Fusion **53**, 10.1088/0029-5515/53/4/043004 (2013).

[31] C. Ham, R. Cramp, S. Gibson, S. Lazerson, I. Chapman, and K. A, Nuclear Fusion **56**, 086005 (2016).

[32] R. J. Fonck, D. S. Darrow, and K. P. Jaehnig, Physical Review A **29**, 3288 (1984).

[33] W. W. Heidbrink, K. H. Burrell, Y. Luo, N. A. Pablant, and E. Ruskov, Plasma Physics and Controlled Fusion **46**, 1855 (2004).

[34] F. M. Levinton, G. G. M. Fonck, R. J., R. Kaita, H. W. Kugel, E. T. Powell, and D. W. Roberts, Physical Review Letters **63**, 2060 (1989).

[35] A. Boileau, M. Von Hellerman, W. Mandl, H. P. Summers, H. Weisen, and A. Zinoviev, Journal of Physics B: Atomic, Molecular and Optical Physics **22**, 10.1088/0953-4075/22/7/002 (1989).

[36] F. M. Levinton, G. M. Gammel, R. Kaita, H. W. Kugel, and D. W. Roberts, Review of Scientific Instruments **61**, 2914 (1990).

[37] N. J. Conway, M. F. De Bock, C. A. Michael, M. J. Walsh, P. G. Carolan, N. C. Hawkes, E. Rachlew, J. F. McCone, S. Shibaev, and G. Wearing, Review of Scientific Instruments **81**, 10.1063/1.3494254 (2010).

[38] F. M. Levinton and H. Yuh, Review of Scientific Instruments **79**, 1 (2008).

[39] E. L. Foley and F. M. Levinton, Review of Scientific Instruments **77**, 10.1063/1.2219432 (2006).

[40] E. L. Foley and F. M. Levinton, Review of Scientific Instruments **84**, 10.1063/1.4802691 (2013).

[41] R. T. Mumgaard, *PhD Thesis*, Ph.D. thesis, Massachusetts Institute of Technology (2015).

[42] J. Howard, A. Diallo, R. Jaspers, and J. Chung, Plasma and Fusion Research **5**, S1010 (2010).

[43] J. Howard, Plasma Physics and Controlled Fusion **50**, 10.1088/0741-3335/50/12/125003 (2008).

[44] C. A. Michael, *Doppler spectroscopy of argon plasmas in H-1NF using a coherence imaging camera*, Ph.D. thesis, Australian National University (2003).

[45] J. Howard, C. Michael, H. Chen, R. Lester, A. Thorman, and J. Chung, Journal of Instrumentation **10** (9).

[46] A. Thorman, C. Michael, J. Howard, B. Victor, C. Holcomb, and S. Allen, Review of Scientific Instruments **89**, 10.1063/1.5038969 (2018).

[47] O. P. Ford, J. Howard, and R. C. Wolf, Review of Scientific Instruments **093504**, 10.1063/1.4929873 (2016).

[48] R. Fischer, A. Bock, A. Burckhart, O. P. Ford, L. Giannone, V. Igochine, M. Weiland, and M. Willensdorfer, Nuclear Fusion **59**, 10.1088/1741-4326/ab0b65 (2019).

[49] A. Thorman, Journal of Quantitative Spectroscopy and Radiative Transfer **207**, 8 (2018).

[50] O. Sauter, C. Angioni, and Y. R. Lin-Liu, Physics of Plasmas **6**, 2384 (1999).

[51] R. Hager and C. S. Chang, Physics of Plasmas **23**, 10.1063/1.4945615 (2016).

[52] M. F. De Bock, N. J. Conway, M. J. Walsh, P. G. Carolan, and N. C. Hawkes, Review of Scientific Instruments **79**, 9 (2008).

[53] L. Lao, H. St. John, R. Stambaugh, A. Kellman, and W. Pfeiffer, Nuclear Fusion **25**, 1611 (1985).

[54] J. C. Kemp, G. D. Henson, C. T. Steiner, and E. R. Powell, Nature **326**, 270 (1987).

[55] T. Kondoh, A. E. Costley, T. Sugie, Y. Kawano, A. Malaquias, and C. I. Walker, Review of Scientific Instruments **75**, 3420 (2004).

[56] R. A. Tinguely, M. Hoppe, R. S. Granetz, R. T. Mumgaard, and S. Scott, Nuclear Fusion **59**, 10.1088/1741-4326/ab2d1d (2019).

[57] B. H. Bransden and C. J. Jochain, *Physics of Atoms and Molecules*, 2nd ed. (Pearson Education, 2003).

[58] D. J. Griffiths, *Introduction to Quantum Mechanics*, 2nd ed. (Pearson Prentice Hall, 2005).

[59] B. H. Bransden and C. J. Jochain, *Quantum Mechanics*, 2nd ed. (Pearson Education, 2000).

[60] C. J. Foot, *Atomic Physics*, 1st ed. (Oxford University Press, 2005).

[61] NIST Standard Reference Database 78 v5.7 (2019).

[62] P. G. Carolan, Plasma Physics and Controlled Fusion **27**, 1101 (1985).

[63] J. D. Hey, C. C. Chu, and E. Hintz, Journal of Physics B: Atomic, Molecular and Optical Physics **32**, 3555 (1999).

[64] A. H. Bethe and E. E. Salpeter, *Quantum Mechanics of One and Two Electron Atoms* (Springer, 1957).

[65] P. Lotte, A. Malaquias, R. Giannella, M. V. Hellermann, P. Nielsen, and C. Walker, Plasma Physics and Controlled Fusion **26**, 4 (2002).

[66] M. F. Gu, C. T. Holcomb, R. J. Jayakuma, and S. L. Allen, Journal of Physics B: Atomic, Molecular and Optical Physics **41**, 10.1088/0953-4075/41/9/095701 (2008).

[67] H. Y. H. Yuh, *PhD Thesis*, Ph.D. thesis, Massachusetts Institute of Technology (2005).

[68] L. Appel, G. Huysmans, L. Lao, P. McCarthy, D. Muir, E. Solano, J. Storrs, D. Taylor, and W. Zwingmann, in *33rd EPS Conference on Controlled Fusion and Plasma Physics* (2006) pp. P–2.160.

[69] W. A. Shurcliff, *Polarized Light: Production and Use* (Harvard University Press, 2013).

[70] E. Collett, *Field Guide to Polarization* (SPIE Press, 2005).

[71] M. Kuldkepp, E. Rachlew, N. C. Hawkes, and B. Schunke, Review of Scientific Instruments **75**, 3446 (2004).

[72] M. Kuldkepp, N. C. Hawkes, E. Rachlew, and B. Schunke, Applied Optics **44**, 5899 (2005).

[73] D. Yang, J. C. Canit, and E. Gaignebet, Journal of Optics **26**, 151 (1995).

[74] D. Wróblewski and L. L. Lao, Review of Scientific Instruments **63**, 5140 (1992).

[75] M. Abramowitz and I. A. Stegun, *Handbook of mathematical functions with formulas, graphs, and mathematical tables.*, Vol. 55 (National Bureau of Standards Applied Mathematics series 55, 1964) p. 361.

[76] D. Alves, A. Stephen, N. Hawkes, S. Dalley, A. Goodyear, R. Felton, E. Joffrin, and H. Fernandes, Fusion Engineering and Design **71**, 175 (2004).

[77] M. J. Creese, *An Analysis of 2D Motional Stark Effect Imaging and Prospects for Determining the Structure of the Magnetic Field Inside a Tokamak*, Ph.D. thesis, Australian National University (2009).

[78] K. Kato, IEEE Journal of Quantum Electronics **22**, 1013 (1986).

[79] F. E. Veiras, L. I. Perez, and M. T. Garea, Applied Optics **49**, 2769 (2010).

[80] A. Thorman, *Polarisation Coherence Imaging of Electric and Magnetic Fields in Plasmas*, Ph.D. thesis, Australian National University (2018).

[81] F. e. a. Wagner, Phys. Rev. Lett. **49**, 1408 (1982).

[82] M. F. De Bock, J. Citrin, S. Saarelma, D. Temple, N. J. Conway, A. Kirk, H. Meyer, and C. A. Michael, Plasma Physics and Controlled Fusion **54**, 10.1088/0741-3335/54/2/025001 (2012).

[83] P. B. Snyder, H. R. Wilson, J. R. Ferron, L. L. Lao, A. W. Leonard, T. H. Osborne, A. D. Turnbull, D. Mossessian, M. Murakami, and X. Q. Xu, Physics of Plasmas **9**, 2037 (2002).

[84] L. Horvath, C. F. Maggi, F. J. Casson, V. Parail, L. Frassinetti, F. Koechl, S. Saarelma, M. G. Dunne, and K. J. Gibson, Plasma Physics and Controlled Fusion **60**, 10.1088/1361-6587/aac7a9 (2018).

[85] A. Burckhart, E. Wolfrum, R. Fischer, K. Lackner, and H. Zohm, Plasma Physics and Controlled Fusion **52**, 10.1088/0741-3335/52/10/105010 (2010).

[86] B. W. Rice, D. G. Nilson, K. H. Burrell, and L. L. Lao, Review of Scientific Instruments **70**, 815 (1999).

[87] K. H. Burrell, E. J. Doyle, P. Gohil, R. J. Groebner, J. Kim, R. J. La Haye, L. L. Lao, R. A. Moyer, T. H. Osborne, W. A. Peebles, C. L. Rettig, T. H. Rhodes, and D. M. Thomas, Physics of Plasmas **2**, 1358 (1995).

[88] E. Viezzer, *Radial electric field studies in the plasma edge of ASDEX Upgrade*, Ph.D. thesis, Ludwig Maximilian University of Munich (2012).

[89] A. R. Field, J. McCone, N. J. Conway, M. Dunstan, S. Newton, and M. Wisse, Plasma Physics and Controlled Fusion **51**, 10.1088/0741-3335/51/10/105002 (2009).

[90] N. J. Conway, P. G. Carolan, J. McCone, M. J. Walsh, and M. Wisse, Review of Scientific Instruments **77**, 1 (2006).

[91] R. J. Groebner and T. H. Osborne, Physics of Plasmas **5**, 1800 (1998).

[92] R. Scannell, M. Beurskens, P. G. Carolan, A. Kirk, M. Walsh, T. O'Gorman, and T. H. Osborne, Review of Scientific Instruments **82**, 10.1063/1.3581230 (2011).

[93] O. Meneghini, S. P. Smith, L. L. Lao, O. Izacard, Q. Ren, J. M. Park, J. Candy, Z. Wang, C. J. Luna, V. A. Izzo, B. A. Grierson, P. B. Snyder, C. Holland, J. Penna, G. Lu, P. Raum, A. McCubbin, D. M. Orlov, E. A. Belli, N. M. Ferraro, R. Prater, T. H. Osborne, A. D. Turnbull, and G. M. Staebler, Nuclear Fusion **55**, 10.1088/0029-5515/55/8/083008 (2015).

[94] J. W. Berkery, S. A. Sabbagh, R. Akers, Y. Andreopoulos, D. Battaglia, J. M. Bialek, C. Ham, L. Kogan, A. Piccione, J. D. Riquezes, D. Ryan, A. Thornton, Z. R. Wang, and G. Xia, 46th EPS Conference on Plasma Physics, EPS 2019 , 4 (2019).

[95] M. Gelfusa, A. Murari, I. Lupelli, N. Hawkes, P. Gaudio, M. Baruzzo, M. Brix, T. Craciunescu, V. Drozdov, A. Meigs, E. Peluso, M. Romanelli, S. Schmuck, and B. Sieglin, Review of Scientific Instruments **84**, 10.1063/1.4824200 (2013).

[96] R. Layne, N. Cook, D. Harting, D. C. McDonald, and C. Tidy, Fusion Engineering and Design **85**, 403 (2010).

[97] T. Edlington, R. Martin, and T. Pinfold, Review of Scientific Instruments **72**, 421 (2001).

[98] E. Arends, *Density gradients in spherical tokamak plasmas*, Ph.D. thesis (2003).

[99] J. Storrs, J. Dowling, G. Counsell, and G. McArdle, Fusion Engineering and Design **81**, 1841 (2006).

[100] G. Braithewaite, N. Gottardi, G. Magyar, J. O'Rourke, J. Ryan, and D. Veron, Review of Scientific Instruments **60**, 10.1063/1.1140666 (1989).

[101] E. J. Strait, L. L. Lao, M. E. Mauel, B. W. Rice, T. S. Taylor, K. H. Burrell, M. S. Chu, E. A. Lazarus, T. H. Osborne, S. J. Thompson, and A. D. Turnbull, Physical Review Letters **75**, 4421 (1995).

[102] T. C. Hender, P. Hennequin, B. Alpher, T. Hellsten, D. F. Howell, and E. Al, Plasma Physics and Controlled Fusion **44** (2002).

[103] T. Taylor, Plasma Physics and Controlled Fusion **39** (1997).

[104] A. K. Cline, Communications of the ACM **17**, 218 (1974).

[105] L. C. Appel and I. Lupelli, Computer Physics Communications **223**, 1 (2017).

[106] R. Goldston, D. McCune, H. Towner, S. Davis, R. Hawryluk, and G. Schmidt, Journal of Computational Physics **43**, 61 (1981).

[107] M. Brix, N. C. Hawkes, A. Boboc, V. Drozdov, and S. E. Sharapov, Review of Scientific Instruments **79**, 10.1063/1.2964180 (2008).

[108] C. Hirsch, *Numerical computation of internal and external flows: The fundamentals of computational fluid dynamics.*, 2nd ed. (Elsevier, Oxford, 2007).

[109] V. F. Shevchenko, R. G. Vann, S. J. Freethy, and B. K. Huang, Journal of Instrumentation **7** (10).

[110] R. G. Vann, K. J. Brunner, R. Ellis, G. Taylor, and D. A. Thomas, Review of Scientific Instruments **87**, 10.1063/1.4962253 (2016).

[111] A G Peeters, Plasma Physics and Controlled Fusion **42**, B231 (2000).

[112] R. L. Lester, *Doppler coherence imaging of ion flows and temperatures in the MAGPIE helicon plasma*, Ph.D. thesis, Australian National University (2018).

[113] A. Kirk, G. F. Counsell, H. R. Wilson, J. W. Ahn, R. Akers, E. R. Arends, J. Dowling, R. Martin, H. Meyer, M. Hole, M. Price, P. B. Snyder, D. Taylor, M. J. Walsh, and Y. Yang, Plasma Physics and Controlled Fusion **46**, 551 (2004).

[114] H. P. Summers, The ADAS User Mnaual, version 2.6 (2004).

[115] M. F. De Bock, N. J. Conway, M. J. Walsh, P. G. Carolan, and N. C. Hawkes, Review of Scientific Instruments **79**, 10.1063/1.2966459 (2008).

[116] P. Geelen, *Simulation of the Motional Stark Effect on C-MOD using MSESIM and PERF*, Tech. Rep. (MIT, 2012).

[117] O. Marchuk, Y. Ralchenko, R. K. Janev, W. Biel, E. Delabie, and A. M. Urnov, Journal of Physics B: Atomic, Molecular and Optical Physics **43**, 10.1088/0953-4075/43/1/011002 (2009).

[118] M. N. Beurskens, A. Alfier, B. Alper, I. Balboa, J. Flanagan, W. Fundamenski, E. Giovannozzi, M. Kempenaars, A. Loarte, P. Lomas, E. De La Luna, I. Nunes, R. Pasqualotto, R. A. Pitts, G. Saibene, M. Walsh, and S. Wiesen, Nuclear Fusion **49**, 10.1088/0029-5515/49/12/125006 (2009).

[119] A. Patel, P. G. Carolan, N. J. Conway, C. A. Bunting, and R. J. Akers, Review of Scientific Instruments **75**, 4145 (2004).

[120] J. Howard, C. Michael, F. Glass, J. Howard, J. Chung, R. König, and J. Howard 10.1088/0953-4075/43/14/144010 (2008).

[121] S. A. Silburn, J. R. Harrison, J. Howard, K. J. Gibson, H. Meyer, C. A. Michael, and R. M. Sharples, Review of Scientific Instruments **85**, 10.1063/1.4891165 (2014).

[122] M. N. Beurskens, T. H. Osborne, L. D. Horton, L. Frassinetti, R. Groebner, A. Leonard, P. Lomas, I. Nunes, S. Saarelma, P. B. Snyder, I. Balboa, B. Bray, K. Crombé, J. Flanagan, C. Giroud, E. Giovannozzi, M. Kempenaars, N. Kohen, A. Loarte, J. Lönnroth, E. De La Luna, G. Maddison, C. Maggi, D. McDonald, G. McKee, R. Pasqualotto, G. Saibene, R. Sartori, E. Solano, W. Suttrop, E. Wolfrum, M. Walsh, Z. Yan, L. Zabeo, and D. Zarzoso, Plasma Physics and Controlled Fusion **51**, 10.1088/0741-3335/51/12/124051 (2009).

[123] G. Cunningham, Fusion Engineering and Design **88**, 3238 (2013).

[124] Y. K. Peng and D. J. Strickler, Nuclear Fusion **26**, 769 (1986).

[125] B. Lloyd, J. W. Ahn, R. J. Akers, L. C. Appel, D. Applegate, K. B. Axon, Y. Baranov, C. Brickley, C. Bunting, R. J. Buttery, P. G. Caro-

lan, C. Challis, D. Ciric, N. J. Conway, M. Cox, G. F. Counsell, G. Cunningham, A. Darke, A. Dnestrovskij, J. Dowling, B. Dudson, M. R. Dunstan, A. R. Field, S. Gee, M. P. Gryaznevich, P. Helander, T. C. Hender, M. Hole, N. Joiner, D. Keeling, A. Kirk, I. P. Lehane, F. Lott, G. P. Maddison, S. J. Manhood, R. Martin, G. J. McArdle, K. G. McClements, H. Meyer, A. W. Morris, M. Nelson, M. R. O'Brien, A. Patel, T. Pinfold, J. Preinhaelter, M. N. Price, C. M. Roach, V. Rozhansky, S. Saarelma, A. Saveliev, R. Scannell, S. Sharapov, V. Shevchenko, S. Shibaev, K. Stammers, J. Storrs, A. Sykes, A. Tabasso, D. Taylor, M. R. Tournianski, A. Turner, G. Turri, M. Valovic, F. Volpe, G. Voss, M. J. Walsh, J. R. Watkins, H. R. Wilson, and M. Wisse, Plasma Physics and Controlled Fusion **46**, 10.1088/0741-3335/46/12B/040 (2004).

[126] S. L. Allen, C. M. Samuell, W. H. Meyer, and J. Howard, Review of Scientific Instruments **89**, 10.1063/1.5038739 (2018).

[127] N. C. Hawkes and M. Brix, Review of Scientific Instruments **77**, 10.1063/1.2221915 (2006).

[128] S. Chandrasekar, *Liquid Crystals*, Vol. 6 (1977) pp. 1–21.

[129] Z. Zhuang, Y. J. Kim, and J. S. Patel, Applied Physics Letters **76**, 3995 (2000).

[130] R. Herke, M. H. Anderson, and T. Baur, , 1 (2005).

[131] S. T. Tang, H. W. Chiu, and H. S. Kwok, Journal of Applied Physics **87**, 632 (2000).

[132] R. Lester, Y. Zhai, C. Corr, and J. Howard, Plasma Sources Science and Technology **25**, 10.1088/0963-0252/25/1/015025 (2016).

[133] C. T. Holcomb, M. A. Makowski, S. L. Allen, W. H. Meyer, and M. A. Van Zeeland, Review of Scientific Instruments **79**, 1 (2008).

[134] D. M. Thomas, A. W. Leonard, and H. W. Mueller, Review of Scientific Instruments **75**, 4109 (2004).

[135] T. C. Luce, C. C. Petty, W. H. Meyer, C. T. Holcomb, K. H. Burrell, and L. J. Bergsten, Plasma Physics and Controlled Fusion **58**, 1 (2016).

[136] W. M. Solomon, K. H. Burrell, R. Feder, A. Nagy, P. Gohil, and R. J. Groebner, Review of Scientific Instruments **79**, 10.1063/1.2957841 (2008).

[137] T. Fujita, H. Kuko, T. Sugie, N. Isei, and K. Ushigusa, Fusion Engineering and Design **34-35**, 289 (1997).

[138] P. Lotte, M. H. Aumeunier, P. Devynck, C. Fenzi, V. Martin, and J. M. Travre, Review of Scientific Instruments **81**, 10.1063/1.3474653 (2010).

[139] B. S. Victor, C. T. Holcomb, S. L. Allen, W. H. Meyer, M. A. Makowski, and A. Thorman, Review of Scientific Instruments **87**, 10.1063/1.4961560 (2016).

[140] E. M. Hollmann, S. Brezinsek, N. H. Brooks, M. Groth, A. G. McLean, A. Y. Pigarov, and D. L. Rudakov, Plasma Physics and Controlled Fusion **48**, 1165 (2006).

[141] Z. A. Xing, D. Eldon, A. O. Nelson, M. A. Roelofs, W. J. Eggert, O. Izacard, A. S. Glasser, N. C. Logan, O. Meneghini, S. P. Smith, R. Nazikian, and E. Kolemen, Fusion Engineering and Design **163**, 112163 (2021).

[142] A. Pavone, J. Svensson, S. Kwak, M. Brix, and R. C. Wolf, Plasma Physics and Controlled Fusion **62**, 10.1088/1361-6587/ab7732 (2020).

[143] O. Asunta, J. Govenius, R. Budny, M. Gorelenkova, G. Tardini, T. Kurki-Suonio, A. Salmi, and S. Sipilä, Computer Physics Communications **188**, 33 (2015).

[144] C. Giroud, A. Meakins, M. Carr, A. Bacerio, and C. Bertrand, CHERAB spectroscopy modelling framework (2018).

[145] D. D. Team, Dask: Library for dynamic task scheduling (2016).

[146] M. Novak, J. Millerd, N. Brock, M. North-Morris, J. Hayes, and J. Wyant, Applied Optics **44**, 6861 (2005).

[147] A. J. Donné, A. E. Costley, R. Barnsley, H. Bindslev, R. Boivin, G. Conway, R. Fisher, R. Giannella, H. Hartfuss, M. G. Von Hellermann, E. Hodgson, L. C. Ingesson, K. Itami, D. Johnson, Y. Kawano, T. Kondoh, A. Krasilnikov, Y. Kusama, A. Litnovsky, P. Lotte, P. Nielsen, T. Nishitani, F. Orsitto, B. J. Peterson, G. Razdobarin, J. Sanchez, M. Sasao, T. Sugie, G. Vayakis, V. Voitsenya, K. Vukolov, C. Walker, and K. Young, Nuclear Fusion **47**, 10.1088/0029-5515/47/6/S07 (2007).

[148] J. N. Brooks and J. P. Allain, Nuclear Fusion **48**, 10.1088/0029-5515/48/4/045003 (2008).

[149] A. Bock 10.17617/2.2303955 (2016).

[150] A. Thorman, C. Michael, M. De Bock, and J. Howard, Review of Scientific Instruments **87**, 10.1063/1.4958648 (2016).

[151] E. L. Foley, F. M. Levinton, H. Y. Yuh, and L. E. Zakharov, Review of Scientific Instruments **79**, 10.1063/1.2957776 (2008).

[152] N. A. Pablant, K. H. Burrell, R. J. Groebner, C. T. Holcomb, and D. H. Kaplan, Review of Scientific Instruments **81**, 10.1063/1.3491209 (2010).